THÈSE DE DOCTORAT
DE L'UNIVERSITÉ DE LILLE

LABORATOIRE DE MÉCANIQUE, MULTIPHYSIQUE ET
MULTIECHELLE (FRE 2016, CNRS)

Présentée par

Zhan YU

pour obtenir le grade de

DOCTEUR DE L'UNIVERSITÉ DE LILLE

Domaine

GÉNIE CIVIL

Sujet de la thèse

Modélisation de l'endommagement et de la fissuration des roches argileuses sous sollicitations thermo-hydromécaniques avec la méthode de champ de phase

Soutenue le 29 Novembre 2019 devant le jury composé de :

Pr. A. GENS	Universitat Polotecnica de Catalunya,	*Rapporteur*
Pr. D. HOXHA	Université d'Orléans	*Rapporteur*
Pr. H. DUMONTET	Sorbonne Université	*Membre*
Pr. A GIRAUD	Université de Lorraine	*Membre*
Dr. M. VU	ANDRA	*Membre*
Pr. J.F. SHAO	Université de Lille	*Directeur de thèse*

LAMCUBE - UNIVERSITÉ LILLE

Abstract

In the general framework of research projects related to geological disposal of radioactive waste, shale gas production and acid gas sequestration, it is necessary to investigate damage and cracking in clayey rocks under coupled thermo-hydro-mechanical loads (THM).

In the first part of the thesis, a new phase-field method is developed for rock-like materials. Two crack fields are introduced in order to describe both tensile and shear cracks. A proper thermodynamics framework is proposed to describe the evolution of two crack fields. The plastic deformation of rocks is also taken into account. An efficient numerical algorithm is adopted for the coupling between the crack fields and displacement field. This algorithm is then set up in the framework of the finite element method. The efficiency of the new phase-field method is illustrated through examples showing tensile and shear cracks.

In the second part, the phase-field method is extended to problems with thermo-hydro-mechanical coupling. To this end, a specific procedure is developed for the coupling between the crack fields, mechanical field and hydraulic and thermal fields. The effects of THM coupling on cracking mechanisms are investigated.

The last part is devoted to two representative examples of application. The first one is relevant to the study of excavation induced damage and cracking around an underground gallery. The second one is related to the thermally induced cracking. Both examples are based on in situ experiments performed in the underground research laboratory of Andra.

Résumé

Dans le contexte général de différents projets de recherche liés au stockage géologique des déchets radioactifs, à l'exploration de gaz de schiste et à la séquestration de gaz acides, il est nécessaire d'étudier l'endommagement et la fissuration des roches argileuses sous sollicitations thermo-hydromécaniques.

La première partie de la thèse est consacrée au développement d'une nouvelle méthode de champ de phase pour des géomatériaux sous sollicitations complexes. Deux champs de phase sont définis afin de prendre en compte des fissures de traction et de cisaillement. Un cadre thermodynamique est proposé permettant de décrite les évolutions des deux champs de fissures. La déformation plastique des roches est également prise en considération. Un algorithme spécifique est ensuite proposé pour prendre en compte le couplage entre les champs de fissures et le champ de déplacement. Cet algorithme est mis en oeuvre dans le cadre de la méthode des éléments finis. L'efficacité de la nouvelle méthode de champ de phase est illustrée par des exemples de fissuration en traction et en cisaillement.

Dans la deuxième partie, la méthode de champ de phase est étendue aux problèmes de couplage thermo-hydromécanique (THM). Une procédure numérique est développée permettant de considérer le couplage entres les champs de fissures, le champ mécanique et les champs de pression de fluide et de température. Les effects du couplage THM sur les mécanismes de fissuration est mis en évidence.

Dans la dernière partie, deux exemples d'application sont présentés. Le premier concerne l'étude de l'endommagement et de la fissuration induits par l'excavation autour d'une galerie souterraine. Le deuxième est lié au problème de fissuration induite par la variation de température. Les deux exemples sont basés sur des expérimentations in situ menées par l'Andra.

Acknowledgement

I would like to express my gratitude to all those who helped me during the writing of this thesis. I gratefully acknowledge the help of my main supervisor, Pro. Jianfu

SHAO, who has offered me valuable suggestions in the academic studies and whose useful suggestions, incisive comments as well as constructive criticism have contributed greatly to the completion of this thesis. I also do appreciate his precious guidances, patience, confidences and encourage during three years of my research and it is a great honor for me to be one of his students. I am deeply grateful for the comments from Professor Antonio

GENS, Professor Dashnor HOXHA as the reviewers of the manuscript of my dissertation. Great thanks also give to all the members of the research group in Lamcube, including

Pr. Wanqing Shen, Pr. Yun Jia, Dr. Yajun Cao, Dr. Lunyang Zhao, Dr. Bei Han, Dr. Yulong Zhang, Dr Hailing Shi, Dr. Yue Tong, Dr. Jianjian Zhao, Dr. Xi Chen, Dr. Jueliang Chen, Dr. Meng Wang.... They gave me not only much help in the research, but also provide much assistance.

Last but not least, I have to give a great appreciation to my parents and my girlfriend Yue Sun, for their unconditional support and encouragement during my academic career.

Zhan Yu

Contents

List of Figures

List of Tables

Chapter I

General Introduction

This research work was conducted with the support of Andra(French national radioactive waste management agency). Intermediate-level high-level and long-lived waste (HA-LLAM) is currently stored in reprocessing plants. Several countries around the world are studying the possibilities of storage in deep geological formations with a period of reversibility. The underground research laboratory at Bure(Centre de Meuse/Haute-Marne), developed by Andra, aims to evaluate the feasibility of building a deep storage site. Callovo-Oxfordian claystone(COx) is chosen as a potential host formation due to its recovery capacity and its hydro-mechanical properties (low permeability and porosity). More than 1500m of galleries were built and instrumented at -490m depth.

The storage of radioactive waste therefore requires rock excavation at great depth to accommodate the various facilities. In a context of durability and security, Thermo-Hydro-Mechanical (THM) behavior of the COx is of great importance in what concern the design and safety calculation of the high-level and intermediate-level long-lived waste disposals. It concerns the several major issues: the fractured area around walls after excavation; and the time-dependent behaviors of COx claystone after the excavation. Moreover, the heat emitted from the wastes shall provoke a pore-pressure increase within the surrounding rock due to the differential thermal expansion of the pore water and the solid skeleton. Numerical models are then used to describe, predict and help to understand these mechanisms in addition to experimental data that are sometimes inaccessible.

Unlike metal materials, the rock-like materials are usually subjected to compression-dominating stresses in most engineering applications such as underground cavities. As a consequence, cracking modes are complex including tensile and shear cracks. The tran-

sition from diffuse micro-cracking to localized macroscopic fractures is the key issue for modeling failure process in these materials and structures. With the onset of localized fractures, strong displacement discontinuities appear. Further, multiple fractures can initiate, propagate and interact. This makes numerical modeling a real challenge. Different numerical methods have been developed during the last decades to deal with this complex subject. For example, enriched finite element methods have been first developed to account for displacement discontinuities at the elementary level with the help of enriched shape functions [Oliver, 1996]. On the other hand, the extended finite element method (XFEM) have been developed to deal with displacement discontinuities by using nodal enrichment techniques [Moes et al., 1999]. This kind of methods have successfully been applied to different kinds of materials and structures, in particular hydraulic fracturing [Zeng et al., 2018, 2019]. In these two types of methods, the transition from diffuse damage to localized fracturing, on the other word, the onset of macroscopic cracks, is still a pending issue. The description of multiple cracks in three-dimensional conditions is also a delicate task. Some authors have tried to solve the problem of transition from diffuse damage to localized cracking by developing homogenized damage models with a representative elementary volume containing an oriented crack [Zhao et al., 2018a,b, Zhu et al., 2016]. The efficiency of such models at the structure scale still needs to be demonstrated.

More recently, based on the framework of variational principle for fracture mechanics [Francfort and Marigo, 1998] and optimal approximations methods of functionals with jumps [Ambrosio and Tortorelli, 1990, Bourdin et al., 2000, Mumford and Shah, 1989], the so-called phase-field method has been developed [Miehe et al., 2010a]. Then, this method has attracted more and more attention and gained a number of extensions [Ambati et al., 2015, Borden et al., 2012]. In this method, the sharp topology of the crack is approximated by a regularized topology with the help of an auxiliary crack phase-field. This one is determined by a proper boundary values problem based on a regularized variational principle. The phase-field method has successfully been applied to various engineering problems including multi-physics problems [Miehe et al., 2015], finite deformation [Borden et al., 2016], coupling between damage and plasticity [Choo and Sun, 2018, Fang et al., 2019].

In most previous studies, a single crack phase-field is generally considered. In most cases, tensile cracks are induced by tensile strain related energy. However, as mentioned above, in rock-like materials, both tensile and shear cracks have to be taken into account.

These two families of cracks are controlled by different driving forces. Further plastic deformation is also an important aspect to be considered and it is generally coupled with evolutions of cracks.

The subject of this thesis focuses mainly on finite element solutions coupled with phase-field numerical modeling of the THM and damage behavior of COx claystone and in particular the induced cracking during the excavation and heating operations. The main object of this work is the development of the phase-field method to introduce both tensile and shear cracks under the effects of THM coupling for rock-like materials.

The first Chapter presents a double phase-field method which extends the classic single phase-field method. Two independent crack fields are introduced to account for tensile and shear cracks respectively. In this Chapter, the foundation of the phase-field model is first presented. And then, the double phase-field method is introduced following the regularized thermodynamics framework and the weak forms of finite element method. Some basic tests are made to compare the simulation results between the classic phase-field model and our double phase-field model. At last, the proposed double field method is applied to study the mechanical behavior of two brittle rocks, sandstone and marble.

The second Chapter continues to present the double phase method applied to quasi-ductile rock-like materials. The plastic behavior is considered as that the regularized variational framework and the thermodynamics framework are extended to take into account the plastic effect. The double crack phase-field method is successfully developed to reproduce the elastic-plastic and damage behavior. At last, the triaxial compression tests of COx claystone are analysed by this new model.

In Chapter 3, we present the coupling between THM fields and crack fields. The model for thermo-poroelastic behavior and the related general equations that govern the thermo-hydro-mechanical coupling are presented. The crack fields are affected by the THM fields which are dependent on the evolution of crack fields. Some representative tests are shown at the end of this Chapter to verify our model.

Chapter 4 is devoted to two examples of application related to the problem of radioactive waste disposal from Andra. The first example is for studying damage and cracked zones during excavation of underground galleries. And the second one deals with THM

and damage modeling during an in situ heating test. In these examples, the experimental results and simulation results are compared for the fields of temperature, pore pressure, displacement and most importantly the fields of tensile and shear cracks.

Chapter II

A double phase-field method for brittle rock-like material

Contents

1 Introduction

Phase-field is a popular method to study the distribution and propagation of fracture problem. It is based on Griffith theory[Griffith and Gilman, 1968] developed by Irwin

[1958], Barenblatt [1962]. To remedy the defect of fracture mechanics, a variational method based on energy minimization is proposed by Francfort and Marigo [1998]. With the help of the regularization work of Ambrosio and Tortorelli [1990] Mumford and Shah [1989] Bourdin et al. [2000] used the Phase-field method in the brittle material. A lot of studies Bourdin et al. [2008] Miehe et al. [2010a] Borden et al. [2012] Ambati et al. [2015] of this method have attracted considerable attention.

In most previous studies, a single crack phase-field is generally considered. In most cases, tensile cracks are induced by tensile strain related energy. However, as mentioned above, in rock-like materials, both tensile and shear cracks have to be taken into account. These two families of cracks are controlled by different driving forces. Therefore, in the present study, a double phase-field method is developed. Two independent crack-phase-fields are introduced to account for the tensile and shear cracks respectively.

In this Chapter, the formulation of the phase-field model is presented at the beginning. And then, we shall present the double phase-field method. In this section, the regularized crack phase-fields and variational principles are first introduced. The thermodynamics framework is defined and used to determine the evolutions of two crack fields. The weak forms of the finite element method are formulated to the solution of crack fields and displacement field. Several benchmarks are used to compare the simulation results between the classic phase-field model and our double phase-field model. At last, the proposed double field method is applied to study the mechanical behavior of sandstone and Jinping marble by considering the transition from diffuse damage to localized cracking.

2 Phase-field model

2.1 Smeared approximation of the shape crack topology

In the framework of phase-field method, the sharp crack topology is approximated by the regularized smeared crack topology [Miehe et al., 2010a] by introducing a scalar-valued auxiliary variable called crack phase-field $d(\mathbf{x})$, taking the unit value on the crack surface and vanishing away from it. This crack phase-field can be determined by solving its own boundary value problem. Further, the differential equations governing the boundary value problem are the Euler equation of the variational problem consisting of minimizing the total crack density (surface) functional in the cracked body. The crack phase-field $d(\mathbf{x})$ can also be seen as equivalent to the macroscopic damage variable used in the continuum damage mechanics.

The schematic presentation of regularized crack topology is shown in Figure II .1.
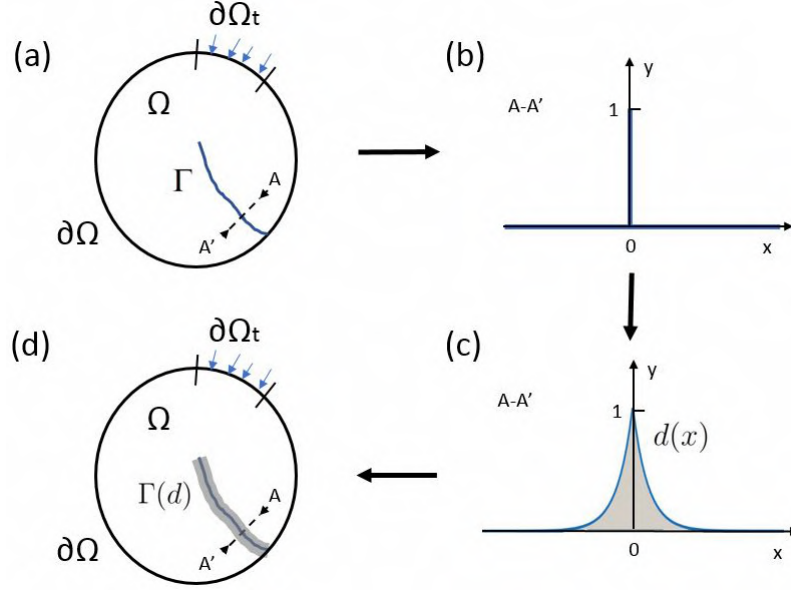
Figure II .1: (a)The real sharp crack Γ in the solid Ω; (b)The real sharp crack in the 1-D coup A-A'; (c) The diffused crack by Phase-field in the 1-D coup A-A'; (d)The diffused crack with its equivalent surface $\Gamma(d)$.

This diffuse crack is easier to be understood in its 1-D view(Figure II .1(b) and (c)).

Each of crack fields is determined by the following boundary problem [Miehe et al., 2010a]:

$$\begin{cases} d - l_d^2 \triangle d = 0 & \text{in } \Omega \\ d(\mathbf{x}) = 1 & \text{on } \Gamma \\ \nabla d(\mathbf{x}).\mathbf{n} = 0 & \text{on } \partial\Omega \end{cases} \tag{II .1}$$

l_d is a length scale parameter controlling the width of smeared cracks. According to Miehe et al. [2010a], the boundary value problem Eq. (II .1) is equivalent to the following variational problem:

$$d(\mathbf{x}) = Arg\{\inf_{d \in S_d} \Gamma_{l_d}(d)\} \tag{II .2}$$

with $S_d = \{d|d(\mathbf{x}) = 1 \text{ at } \mathbf{x} \in \Gamma\}$. $\Gamma_{l_d}(d)$ denotes the total tensile or shear crack density (surface), defined by:

$$\Gamma(d) = \int_{-\infty}^{+\infty} \frac{1}{2}(\frac{1}{l_d}d^2 + l_d d'^2)dx = \int_{-\infty}^{+\infty} \gamma(d, \nabla d)dx \tag{II .3}$$

Clearly, $\gamma(d, \nabla d)$ presents a crack surface density function:

$$\gamma(d, \nabla d) = \frac{1}{2}(\frac{1}{l_d}d^2 + l_d d'^2) \tag{II .4}$$

With this regularization work at hand, the quasi-static process of crack initiation and propagation is described by a minimization problem of the energy function:

$$E(u,d) = \int_\Omega g(d)\Psi_0(\epsilon(u))dV + g_c \int_\Omega \gamma(d, \nabla d)dV \qquad (\text{II .5})$$

with function h(d) presents the influence of crack to the displacement field.

2.2   Governing equations

With regard to the displacement field, the external potential must be considered as:

$$P(u) = \int_\Omega f_b \cdot u dV + \int_{\partial\Omega_t} t_N \cdot u dA \qquad (\text{II .6})$$

with the f_b is body force and the traction $t_N(x,t)$ is prescribed by Neumann-type boundary conditions at $\delta\Omega_t$.

The total energy function can be written as:

$$\Pi = E(u,\Gamma) - P(u) \qquad (\text{II .7})$$

To derive the governing equations through variation of functional(Eq. II .7) respect with the displacement field u and crack field d, the balance equation between external and internal virtual powers for the quasi-static process can be obtained by:

$$\delta\Pi = E(\dot{u}, \dot{d}) - P(\dot{u}) = \int_\Omega \sigma\delta\epsilon dV + \int_\Omega h'(d)\Psi_0\delta d dV + g_c \int_\Omega (\partial_d\gamma\delta d + \partial_{\nabla d}\gamma\delta\nabla d)dV$$
$$- \int_\Omega f_b\delta u dV - \int_{\partial\Omega_t} t_N\delta u dA$$
$$(\text{II .8})$$

with $\sigma = g(d)\partial_\epsilon\Psi_0$.

As $\delta\Pi = 0$ must be hold for both fields considered, we obtain the two coupled balance equations and theirs boundary conditions:

$$\begin{cases} \nabla \cdot \sigma + f_b = 0 & in \ \Omega \\ \sigma \cdot n = t_N & on \ \partial\Omega_t \end{cases} \qquad (\text{II .9})$$

for displacement field;

$$
\begin{cases}
h'(d)\Psi_0 + g_c(\frac{1}{l_d}d - l_d^2\Delta d) \geq 0 \ and \ \dot{d} \geq 0 \quad in \ \Omega \\
d = 1 \quad on \ \Gamma \\
\nabla d \cdot n = 0 \quad on \ \partial\Omega
\end{cases}
\tag{II .10}
$$

for crack field.

Here, we rewrite the balance equation of crack field(Eq. II .10) as:

$$
\underbrace{-h'(d)\mathcal{H}}_{\text{crack driving force}} - \underbrace{g_c(\frac{1}{l_d}d - l_d^2\Delta d)}_{\text{crack resistance}} \leq 0
\tag{II .11}
$$

where $\mathcal{H} = max(\Psi_0)$ is the maximum energy in all recent time step [Miehe et al., 2010a]. This history field $\mathcal{H}$ could reflect the crack irreversibility. Clearly we can see that the 2 parts in Eq. II .10 are positive. The new crack would be created if the crack driving force is bigger than the crack resistance.

3 A double phase-field method

3.1 Regularized crack topology

In most previous studies, only the crack due to tensile stress or strain is considered. In geomechanics, most materials are subjected to complex loading paths including tensile and compressive stresses. In particular, closed cracks can initiate and propagate under shear or deviatoric stress. In order to take into account such process, in the present study, two independent cracks phase-fields are introduced. The tensile crack phase-field is denoted by $d^t(\mathbf{x})$ and the shear crack phase-field by $d^{sh}(\mathbf{x})$. The schematic presentation of regularized crack topology is shown in Figure II .2.
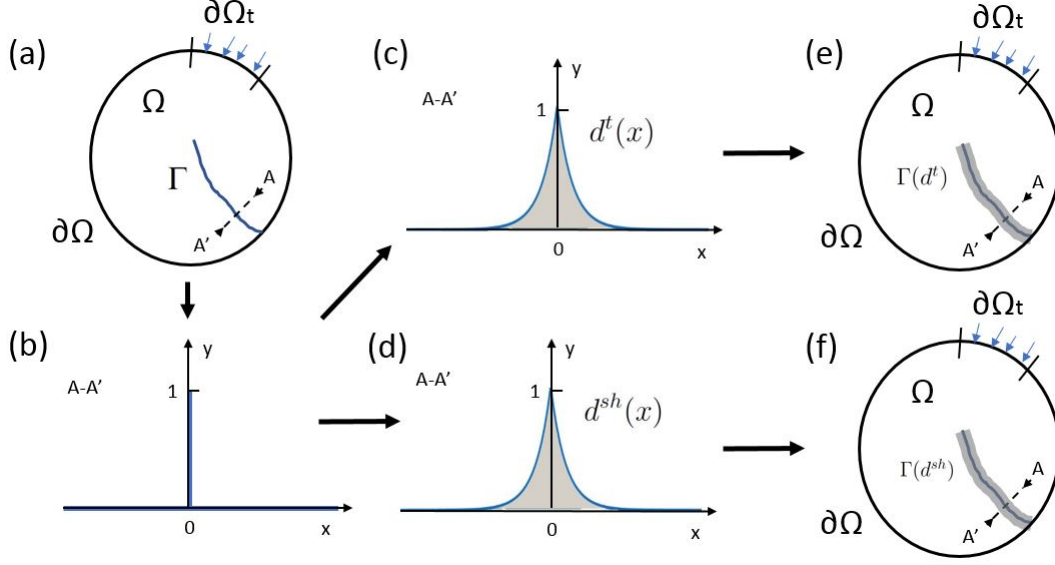
Figure II .2: (a)The real sharp crack Γ in the solid Ω; (b)The real sharp crack in the 1-D coup A-A'; (c)and(d) The diffused tensile&shear crack by phase-field method in the 1-D coup A-A'; (e)and(f)The diffused tensile&shear crack with its equivalent surface $\Gamma(d^t)$&$\Gamma(d^{sh})$.

Each of crack fields is determined by the following boundary problem [Miehe et al., 2010a], with $\alpha = t, sh$:

$$\begin{cases} d^\alpha - l_d^2 \triangle d^\alpha = 0 & \text{in } \Omega \\ d^\alpha(\mathbf{x}) = 1 & \text{on } \Gamma^\alpha \\ \nabla d^\alpha(\mathbf{x}).\mathbf{n} = 0 & \text{on } \partial\Omega \end{cases} \tag{II .12}$$

l_d is a length scale parameter controlling the width of smeared cracks. According to Miehe et al. [2010a], the boundary value problem Eq. (II .12) is equivalent to the following variational problem:

$$d^\alpha(\mathbf{x}) = Arg\{\inf_{d \in S_{d^\alpha}} \Gamma^\alpha_{l_d}(d^\alpha)\} \tag{II .13}$$

with $S_{d^\alpha} = \{d^\alpha | d^\alpha(\mathbf{x}) = 1 \text{ at } \mathbf{x} \in \Gamma^\alpha\}$. $\Gamma^\alpha_{l_d}(d^\alpha)$ denotes the total tensile or shear crack density (surface), defined by:

$$\Gamma^\alpha_{l_d}(d^\alpha) = \int_\Omega \gamma^\alpha(d^\alpha, \nabla d^\alpha)d\Omega; \quad \alpha = t, sh \tag{II .14}$$

$\gamma_\alpha(d^\alpha, \nabla d^\alpha)$ denotes the tensile or shear crack density (surface) per unit volume, defined by:

$$\gamma^\alpha(d^\alpha, \nabla d^\alpha) = \frac{1}{2}\{\frac{1}{l_d}(d^\alpha)^2 + l_d \nabla d^\alpha . \nabla d^\alpha\} \tag{II .15}$$

3.2 Regularized variational framework

In the framework of variational approach to fracture mechanics proposed by Francfort and Marigo [1998], an energy functional was introduced and it is composed of the elastic strain energy and the energy requested to create the crack. With the regularized smeared crack topology presented above, the energy requested to create the sharp crack is approximated by that for the creation of regularized crack surfaces. Thus, the extended form of the total energy functional is given by:

$$
\begin{aligned}
E(\mathbf{u}, d^t, d^{sh}) &= E_u(\mathbf{u}, d^t, d^{sh}) + E_s(d^t, d^{sh}) \\
E_u(\mathbf{u}, d^t, d^{sh}) &= \int_\Omega W_e(\boldsymbol{\epsilon}^e(\mathbf{u}), d^t, d^{sh}) d\Omega \\
E_s(d^t, d^{sh}) &= g_c^t \int_\Omega \gamma^t(d^t, \nabla d^t) d\Omega + g_c^{sh} \int_\Omega \gamma^{sh}(d^{sh}, \nabla d^{sh}) d\Omega
\end{aligned}
\tag{II.16}
$$

W_e is the elastic strain energy of cracked material. The parameters g_c^t and g_c^{sh} are the material toughness respectively for tensile and shear cracks. Note that the total functional E can also be rewritten in the following form:

$$
E(\mathbf{u}, d^t, d^{sh}) = \int_\Omega W(\mathbf{u}, d^t, d^{sh}) d\Omega
\tag{II.17}
$$

with

$$
W(\mathbf{u}, d^t, d^{sh}) = W_e(\boldsymbol{\epsilon}^e(\mathbf{u}), d^t, d^{sh}) + g_c^t \gamma^t(d^t, \nabla d^t) + g_c^{sh} \gamma^{sh}(d^{sh}, \nabla d^{sh})
\tag{II.18}
$$

which can be identified as the free energy.

We focus now on the crack driving force in our new model, which is the core problem of the phase-field method. In order to prevent the issue of cracks interpenetration in compression condition, a unilateral contact formulations is necessary to be used. In the models of phase-field method, there are two common kinds of formulations: (1) the energy decomposition based on the tensile and compressed strain; (2) the energy decomposition based on the spheric and deviatoric strain. The first one has a good agreement with the experimental observation in lots of classic benchmarks. But it is hard to apply the initial anisotropic material. In this section, we will see the $d^t \& d^{sh}$ phase-field model developed by these two decompositions.

3.2.1 Initial isotropic material

Following the Miehe phase-field method, we have:

$$
W_e^0(\epsilon) = W_0^+(\epsilon) + W_0^-(\epsilon)
\tag{II.19}
$$

The energy is decomposed by tensile part and compressed part, depending on the tensile and compressed strains:

$$W_0^{\pm}(\epsilon) = \frac{\lambda}{2}(tr\langle\epsilon\rangle_{\pm})^2 + \mu tr\{(\epsilon^{\pm})^2\} \tag{II .20}$$

and

$$\epsilon^{\pm} = \sum_{D}^{i=1}\langle\epsilon^i\rangle_{\pm}n^i \otimes n^i \tag{II .21}$$

In our model, the decomposition of elastic energy density W_0 must be considered to separate the effective crack driving force of tensile crack and shear crack. Two formulations are proposed based on this tensile/compressed decomposition.

The case 1 is presented as:

$$W_e(\epsilon, d^t, d^{sh}) = \frac{\lambda}{2}(tr\langle\epsilon\rangle_+)^2 h_1(d^t) + \mu tr\{(\epsilon^+)^2\}h_3(d^{sh}) + W_0^-(\epsilon) \tag{II .22}$$

with the degradation functions $h_{1-3}(d^t, d^{sh})$ are defined as:

$$\begin{cases} h_1(d^t) = (1 - \beta_1 d^t)^2 \\\\ h_2(d^t) = (1 - \beta_2 d^t)^2 \\\\ h_3(d^{sh}) = (1 - \beta_3 d^{sh})^2 \end{cases} \tag{II .23}$$

The parameters β_1, β_2 and β_3 are used to reflect the residual elastic stiffness of damaged material.

In this case, we only consider the tensile energy as the crack driving quantity, and this tensile energy is decomposed by the spheric part and the shear part defined by the Lamé coefficients λ and μ. This so called tensile spheric energy plays the role of the driving quantity of tensile crack d^t, and the tensile spheric energy conduits to the shear crack d^{sh}. This model inherits the advantages of the Miehe model, which has a good agreement with the experiment observation. On the other hand, the tensile and shear cracks can be observed separately. And the effect weights of tensile and shear crack in the propagation can be controlled depend on the chosen of the g_c^t and g_c^{sh}.

For the case 2, the formulation of energy is presented as:

$$W_e(\epsilon, d^t, d^{sh}) = W_0^+(\epsilon)h_1(d^t) + \frac{\lambda}{2}(tr\langle\epsilon\rangle_-)^2 + \mu tr\{(\epsilon^-)^2\}h_3(d^{sh}) \tag{II .24}$$

In this case, the total tensile energy is considered as the driving quantity of the tensile crack d^t; and the compressed shear energy conduits to the shear crack d^{sh}. The shear part of the tensile energy is considered as a type of tensile energy which follows the direction of principal strain. And the shear crack is only produced under the compressed condition, it is defined as an compressed shear crack.

3.2.2   Initial anisotropic material

In the Amor phase-field model, the energy is composed by spheric part and deviatoric part:

$$W_e^0(\epsilon) = W_{sph}^0(\epsilon) + W_{dev}^0(\epsilon) = \frac{1}{2}\mathbb{C}_{sph} : \epsilon : \epsilon + \frac{1}{2}\mathbb{C}_{dev} : \epsilon : \epsilon \qquad \text{(II .25)}$$

The spherical and deviatoric elastic stiffness tensors $\mathbb{C}_{sph}^0$ and $\mathbb{C}_{dev}^0$ are defined as:

$$\begin{cases} \mathbb{C}_{sph} = K_0^{reuss}\mathbf{1}\bigotimes\mathbf{1}; \\ \\ \mathbb{C}_{dev} = \mathbb{C}_0 - \mathbb{C}_{sph} \end{cases} \qquad \text{(II .26)}$$

$\mathbb{C}^0$ denotes the total initial elastic stiffness tensor of undamaged material and k_{reuss}^0 is the so-called Reuss bulk modulus. Compared with other decompositions of elastic tensors [Miehe et al., 2010b], the present one is particularly suitable for anisotropic elastic materials.

In order to distinguish the different effects of open and closed cracks, the following crack status coefficient $r_e^{\pm}$ is introduced:

$$\begin{cases} \text{if } tr(\boldsymbol{\epsilon}^e) >= 0 : \ r_e^+ = 1, \ r_e^- = 0 \\ \\ \text{if } tr(\boldsymbol{\epsilon}^e) < 0 : \ r_e^+ = 0, \ r_e^- = 1 \end{cases} \qquad \text{(II .27)}$$

In the case 1 based on the Amor phase-field model, the effect of crack to the energy is presented as:

$$W_e(\epsilon, d^t, d^{sh}) = (h_1(d^t)r^+ + r^-)W_{sph}^0 + h_3(d^{sh})W_{dev}^0 \qquad \text{(II .28)}$$

In this case, we consider the tensile spheric energy as the driving quantity of the tensile crack d^t, and both parts(tensile and compressed parts) of the deviatoric energy conduits to the shear crack d^{sh}. This is a concise formulation to define the two types of crack, but it can not reflect the effect of deviatoric energy to the tensile crack especially under tensile condition.

In order to overcome this issue, the case 2 is proposed as:

$$W_e(\epsilon, d^t, d^{sh}) = (h_1(d^t)r^+ + r^-)W_{sph}^0 + h_2(d^t)h_3(d^{sh})W_{dev}^0 \qquad \text{(II .29)}$$
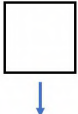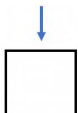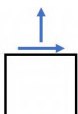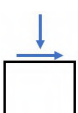
By using this model, W_{sph}^0 is as the tensile crack driving quantity only under the expansion condition. And W_{dev}^0 plays the role of crack driving quantity for both of two types of the crack. The different degradation functions $h_1(d^t)$ and $h_2(d^t)$ are used to distinguish the different weights of influence between spheric energy and deviatoric energy.

And then, in order to separate the effect of d^t and d^{sh} in the W_{dev}^0 under expansion/compression condition, we propose the case 3:

$$W_e(\epsilon, d^t, d^{sh}) = [h_1(d^t)r^+ + r^-]W_{sph}^0 + [h_2(d^t)h_3(d^{sh})r^+ + h_3(d^{sh})r^-]W_{dev}^0(\epsilon) \quad \text{(II .30)}$$

W_{dev}^0 is separated by expansion and compression condition. It plays the same role as in the case 2 under the expansion condition and it plays the role of the shear crack driving quantity under the compression condition. Following this way, we deal the W_{dev}^0 brings tensile fracture and shear fracture when the element is expanded, and the shear fracture here is only defined as the compressed shear fracture. Following this formulation, the driving quantities for tensile crack and shear crack conform well the physical logic. And it works well in the compression tests.

The case 3 is the final version to this driving energy decomposition. The physical interpretation of elastic energy decomposition with respect to degradation by open and closed cracks is illustrated in Figure II .1.

spheric/deviatoric	open/closed	mode	degradation
spheric energy	open crack		$h_1(d^t)$
	closed crack		-
deviatoric energy	open crack		$h_2(d^t) * h_3(d^{sh})$
	closed crack		$h_3(d^{sh})$

Table II .1: The energy divided into 4 parts by spheric/deviatoric and open/closed crack conditions, and their degradation functions.

The table 2.1 can help us to understand the splits used in the model of case 3. At first, in the spherical part of energy, Ψ_{sph} is as a part of the tensile crack driving quantity only under the expansion condition. And this energy can't bring the shear crack.

For the deviatoric part of energy, it can't be ignored that there's crack opening during the shear behavior under the expansion condition. Ψ_{dev} plays the role of crack driving quantity for both of two types of the crack under the expansion condition. But under the compressed condition, Ψ_{dev} is only considered as the shear crack driving quantity.

3.3   Evolution of crack phase fields

The reduced Clausius-Duhem inequality relative to the evolution of the damage parameter d is defined as:

$$\mathcal{A}^{\alpha}\dot{d}^{\alpha} \geqslant 0 \qquad (\text{II .31})$$

$\mathcal{A}^{\alpha} = -\frac{\partial W}{\partial d^{\alpha}}$ is the thermodynamic force associated with the crack phase field d^{α} ($\alpha = t, sh$). Further, it is assumed that the threshold function $F^{\alpha}(\mathcal{A}^{\alpha})$ governing the crack phase field evolution is simply written as:

$$F^{\alpha}(\mathcal{A}^{\alpha}) = \mathcal{A}^{\alpha} \leq 0 \qquad (\text{II .32})$$

Taking into account the irreversible condition of crack growth, one gets for $\dot{d}^{\alpha} > 0$, $F^{\alpha} = 0$. It is:

$$F^{\alpha} = -\{\frac{\partial W_e}{\partial d^{\alpha}} + g_c^{\alpha}\delta\gamma^{\alpha}(d^{\alpha})\} = 0 \qquad (\text{II .33})$$

where $\delta\gamma^{\alpha}(d^{\alpha})$ is the variational derivative of the crack density function [Miehe et al., 2010b]. By considering the definitions of different parts of energy in Eq. II .18, one gets:

$$\begin{cases} -r_e^+ h_1' W_{sph}^0 - h_2' h_3 r_e^+ W_{dev}^0 - g_c^t(\frac{1}{l_d}d^t - l_d^2\Delta d^t) \leq 0 \\ \\ -h_3'(r_e^+ h_2 W_{dev}^0 + r_e^- W_{dev}^0) - g_c^{sh}(\frac{1}{l_d}d^{sh} - l_d^2\Delta d^{sh}) \leq 0 \end{cases} \qquad (\text{II .34})$$

In order to consider complex loading paths with unloading and reloading cycles and considering that the crack growth is an irreversible process, a strain history functional has been introduced in Miehe et al. [2010b]. Inspired by this, in this study, three energy history functionals are defined as follows:

$$\begin{cases} \mathcal{H}_{sph} = max[r_e^+ W_{sph}^0] \\ \\ \mathcal{H}_{dev}^t = max[h_3 r_e^+ W_{dev}^0] \\ \\ \mathcal{H}_{dev}^{sh} = max[r_e^+ h_2 W_{dev}^0 + r_e^- W_{dev}^0] \end{cases} \qquad (\text{II .35})$$

With these energy history functionals at hand, the evolutions of crack phase fields are determined by the following criteria:

$$\begin{cases} -h_1'\mathcal{H}_{sph} - h_2'\mathcal{H}_{dev}^t - g_c^t(\frac{1}{l_d}d^t - l_d^2\Delta d^t) = 0 \\ -h_3'\mathcal{H}_{dev}^{sh} - g_c^{sh}(\frac{1}{l_d}d^{sh} - l_d^2\Delta d^{sh}) = 0 \end{cases} \qquad (\text{II .36})$$

3.4   Numerical implementation in finite element method

We consider here two crack phase fields in the solid body Ω subjected to the body force $\mathbf{f}_b$ in Ω, the surface force $\mathbf{t}_N$ on its boundary $\partial\Omega_f$ and the prescribed displacement $\overline{\mathbf{u}}$ on its boundary $\partial\Omega_u$, as shown in Figure II .2. The total potential energy can be written as:

$$\Pi = E(\mathbf{u}, d^t, d^{sh}) - \int_\Omega \mathbf{f}_b \cdot \mathbf{u} d\Omega - \int_{\partial\Omega_f} \mathbf{t}_N \cdot \mathbf{u} dA \tag{II .37}$$

The stationarity condition of the potential energy $\delta\Pi = 0$ leads to three coupled boundary values problems respectively for the displacement field, the tensile crack phase-field and the shear crack phase field.

The local equations for the displacement field are written as:

$$\begin{cases} \nabla \cdot \boldsymbol{\sigma} + \mathbf{f}_b = 0 \quad \text{in } \Omega \\ \boldsymbol{\sigma} \cdot \mathbf{n} = \mathbf{t}_N \quad \text{on } \partial\Omega_t \end{cases} \tag{II .38}$$

With the help of shape functions and related derivatives in finite elements, one obtains the discrete weak form for the displacement field for the current loading step:

$$\begin{cases} \mathbf{K}_u \triangle\mathbf{U} = \triangle\mathbf{F} \\ \\ \mathbf{K}_u = \int_\Omega \mathbf{B}_u^T \mathbb{C} \mathbf{B}_u d\Omega \\ \\ \triangle\mathbf{F} = \int_\Omega \mathbf{N}_u^T \triangle\mathbf{f}_b d\Omega + \int_{\partial\Omega_f} \mathbf{N}_u^T \triangle\mathbf{t}_N dA \end{cases} \tag{II .39}$$

$\mathbf{N}_u$ and $\mathbf{B}_u$ are respectively the matrix of shape functions and related derivatives of displacement components. $\mathbf{K}_u$ is the global stiffness matrix. $\triangle\mathbf{U}$ and $\triangle\mathbf{F}$ respectively denote the column matrix of increment nodal displacements and forces. The current elastic stiffness matrix of cracked material is given by:

$$\mathbb{C}(d^t, d^{sh}) = [r_e^+ h_1 + r_e^-]\mathbb{C}_{sph}^0 + [r_e^+ h_2 h_3 + r_e^- h_3]\mathbb{C}_{dev}^0 \tag{II .40}$$

For the tensile crack phase field, one has the following local equations:

$$\begin{cases} h_1' \mathcal{H}_{sph} + h_2' \mathcal{H}_{dev}^t + g_c^t(\frac{1}{l_d} d^t - l_d^2 \Delta d^t) = 0 \quad \text{in } \Omega \\ \dot{d}^t \geq 0 \quad \text{in } \Omega \\ d^t = 1 \quad \text{on } \Gamma^t \\ \nabla d^t \cdot \mathbf{n} = 0 \quad \text{on } \partial\Omega \end{cases} \tag{II .41}$$

and for the shear crack phase field:

$$\begin{cases} h_3' \mathcal{H}_{dev}^{sh} + g_c^{sh}(\frac{1}{l_d}d^{sh} - l_d^2 \Delta d^{sh}) = 0 & \text{in } \Omega \\ \dot{d}^{sh} \geq 0 & \text{in } \Omega \\ d^{sh} = 1 & \text{on } \Gamma^{sh} \\ \nabla d^{sh} \cdot \mathbf{n} = 0 & \text{on } \partial\Omega \end{cases} \tag{II .42}$$

Similar to the displacement field, the two crack phase fields and their gradients inside each element are also approximated by the nodal values by using appropriate shape functions and related derivatives. With such approximations, the weak forms and discrete systems of equations are obtained for each crack phase field. Namely, for the tensile cracks field, one gets:

$$\begin{cases} \mathbf{K}_{d^t}\mathbf{d}^t = \mathbf{F}_{d^t} \\ \\ \mathbf{K}_{d^t} = \int_\Omega \{(g_c^t \, l_d + 2\beta_1^2 \mathcal{H}_{sph} + 2\beta_2^2 \mathcal{H}_{dev}^t)\mathbf{N}_d^T \mathbf{N}_d + g_c^t l_d \mathbf{B}_d^T \mathbf{B}_d\}d\Omega \\ \\ \mathbf{F}_{d^t} = \int_\Omega 2(\beta_1 \mathcal{H}_{sph} + \beta_2 \mathcal{H}_{sph}^t)\mathbf{N}_d^T d\Omega \end{cases} \tag{II .43}$$

and for the shear crack field:

$$\begin{cases} \mathbf{K}_{d^{sh}}\mathbf{d}^{sh} = \mathbf{F}_{d^{sh}} \\ \\ \mathbf{K}_{d^{sh}} = \int_\Omega \{(g_c^t \, l_d + 2\beta_3^2 \mathcal{H}_{dev}^{sh})\mathbf{N}_d^T \mathbf{N}_d + g_c^t l_d \mathbf{B}_d^T \mathbf{B}_d\}d\Omega \\ \\ \mathbf{F}_{d^{sh}} = \int_\Omega 2\beta_3 \mathcal{H}_{dev}^{sh}\mathbf{N}_d^T d\Omega \end{cases} \tag{II .44}$$

$\mathbf{N}_d$ and $\mathbf{B}_d$ are the shape functions and related derivatives for two crack phase fields.

It is obvious that three fields are coupled. The calculation of displacement field is influenced by the crack phase fields due to the fact that the elastic stiffness matrix $\mathbb{C}(\mathbf{x})$ is a function of $d^t(\mathbf{x})$ and $d^{sh}(\mathbf{x})$. On the other hand, the evolutions of crack fields are controlled by the energy history functionals which are functions of elastic.

4   Numerical experiments

In this section, three examples of test would be presented to show how our model works. The first 2 examples are classic benchmark problem for phase-field method: single-edge notched tension and shear test. The isotropic phase-field model [Miehe et al., 2010b],

Miehe phase-field model [Miehe et al., 2010b] and Amor phase-field model [Amor et al., 2009] will be compared with our $d^t \& d^{sh}$ phase-field model. The isotropic phase-field model uses all of the elastic strain energy as the driving energy to create the crack. Miehe phase-field model has a good agreement compared with the experimental result. The method of decomposing energy in this model is very popular, lot of studies of phase-field method are based on it. And Amor phase-field method uses the similar method of decomposing energy like ours: decomposition based on spherical and deviatorical parts.

The last example is a tri-axial compression test, it's rare to see the simulation of this test by phase-field model. We try to reproduce the crack path by our elastic-damage model. This laboratory-scale test is simulated under plan strain condition. In all of the following numerical examples, the regular of 4-node elements is adapted.

4.1   Single-edge notched tension test

In this benchmark, we apply the model to a square plate (1×1 mm) with a straight horizontal notch(0.5 mm) located at mid-height of the left edge. The dimensions and the boundary conditions are shown in the Figure II .3(a). The load of displacement $u(t)$ apply on the top outer surface.
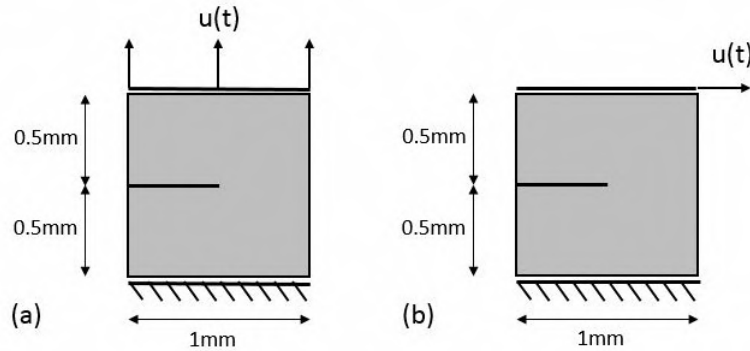
Figure II .3: The dimension and the boundary conditions of single-edge notched tension test.

To match the example of Miehe et al. [2010a], we use the same parameters of material: $\lambda = 121.15 kN/mm^2$, $\mu = 80.77 kN/mm^2$ and $l_d = 5.0 \times 10^{-3} mm$. The toughness parameters $g_c^t = g_c^{sh} = 2.7 \times 10^{-3} kN/mm$ for case 1, $g_c^t = g_c^{sh} = 1.35 \times 10^{-3} kN/mm$ for case 2, because in case 2, the crack driving force is separated by tensile and shear parts independently, every part of energy is reduced. The toughness parameters follow these reductions to march the same resistance abilities. The mesh with refine containing 11790 elements and 3998 nodes and the incremental load of displacement $\Delta u = 1 \times 10^{-5} mm$ are

enough precise for this test.

In case 1, the crack path at different stages of the deformation are illustrated in Figure II .4. The red and blue zone indicate the broken state(d^t or d^{sh}=1) and the unbroken state(d^t or d^{sh}=0) of the material. The main crack which propagates is the tensile one. Almost none shear crack can be observed, because the shear crack in this case is defined as compressed shear crack, but there's no volumetric strain reduced during the test, the shear crack driving force is equal to 0.

               (a)   (b)   (c)   (d)
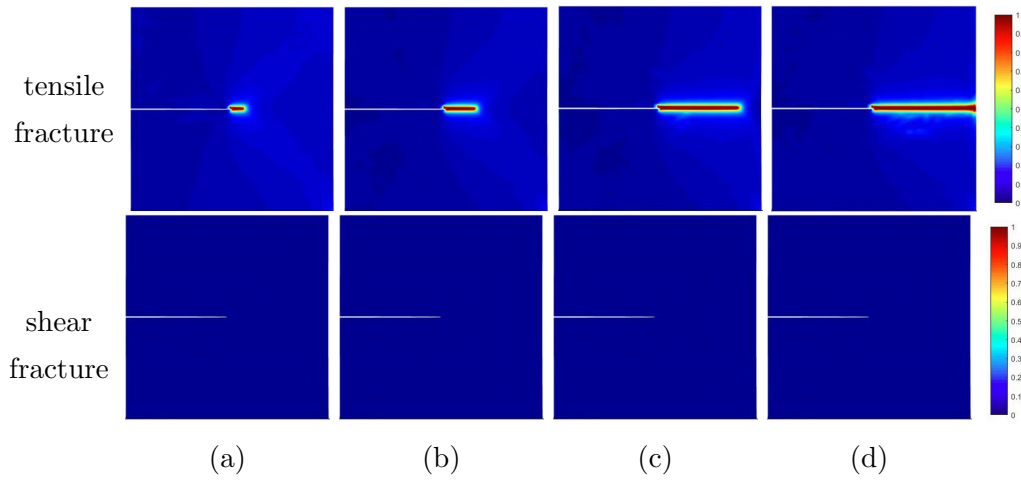
Figure II .4: Single-edge notched tension test simulated by case 1. Crack path at the load of displacement: (a)$u = 5.3 \times 10^{-3} mm$; (b)$u = 5.5 \times 10^{-3} mm$; (c)$u = 6 \times 10^{-3} mm$;(d)$u = 6.2 \times 10^{-3} mm$.

In case 2, the results of simulation is presented as in Figure II .5. Both of two types of crack propagate independently at the same time, and their effects are considered to the stiffness matrix.
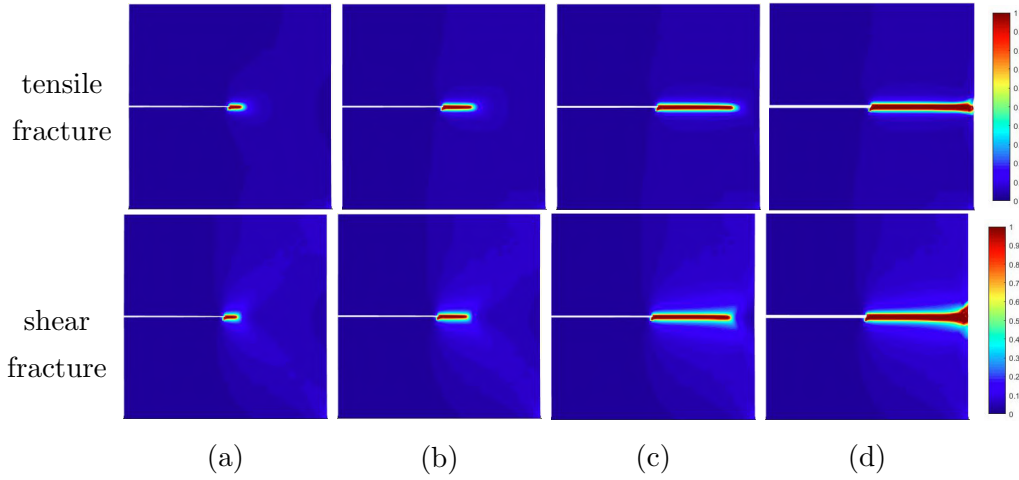
Figure II .5: Single-edge notched tension test simulated by case 2. Crack path at the load of displacement: (a)$u = 5.3 \times 10^{-3}mm$; (b)$u = 5.5 \times 10^{-3}mm$; (c)$u = 6 \times 10^{-3}mm$;(d)$u = 6.2 \times 10^{-3}mm$.

In case 3, the main crack that propagates is the tensile crack as indicated in II .6. A small shear band can be observed along the path of the tensile crack. Compare with cases 1 and 2, in which case, the results of two distributions of damage may show more physical significance. The distribution of tensile damage in three boxes is not significantly altered. And in case 3, the shear damage appeared to be minor in this tensile test.
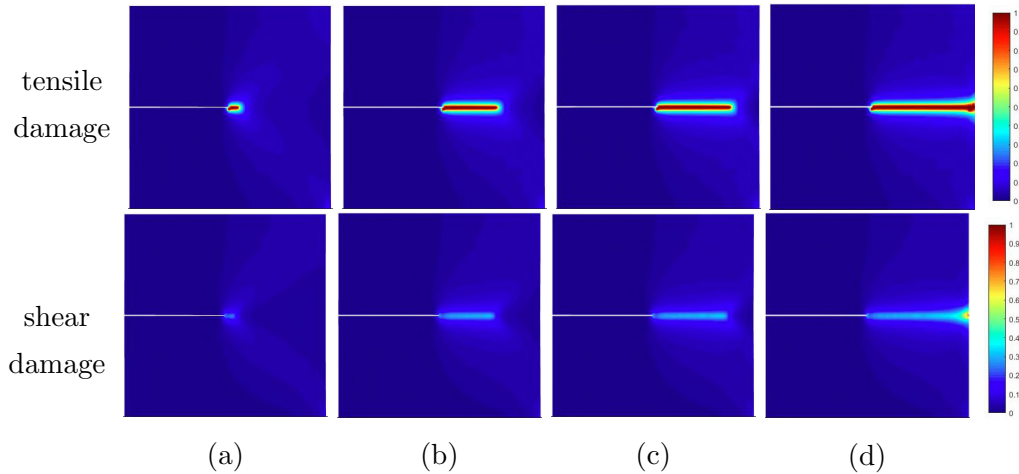
Figure II .6: Single-edge notched tension test. Crack path at the load of displacement: (a)$u = 5.3 \times 10^{-3}mm$; (b)$u = 5.5 \times 10^{-3}mm$; (c)$u = 6 \times 10^{-3}mm$;(d)$u = 6.2 \times 10^{-3}mm$.

Figure II .7 reports a comparison of the reaction-displacement curves between the phase-field model mentioned and our $d^t \& d^{sh}$ model of case 3. The behaviors are quite

similar, it's due to the crack is created by almost all of the strain energy in this test, even the isotropic model has the same result. And for our models, they work well in the fracture mode I. We can see clearly which type of fracture works.
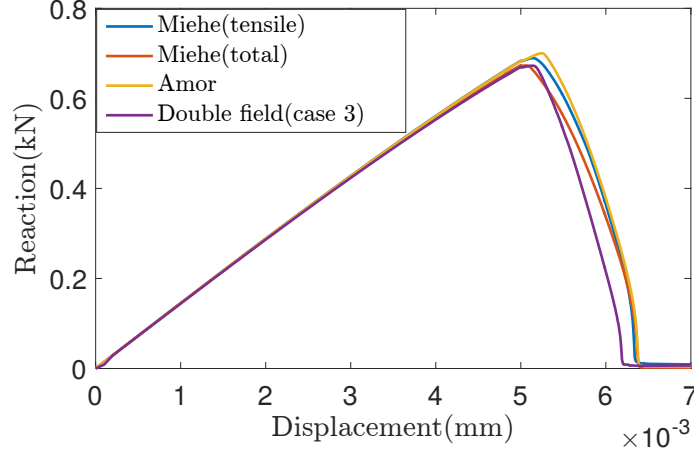
Figure II .7: Single-edge notched tension test. Reaction-displacement curve

4.2   Single-edge notched shear test

The second benchmark is a Single-edge notched shear test. We apply the same plate(same geometry and same material parameter) except the we use $2g_c^t = g_c^{sh} = 2.7 \times 10^{-3} kN/mm$ in case 2. The g_c^t is reduced to the half of the g_c^{sh}. The direction of load is horizontally to the right as in the Figure II .3(b). 22500 elements refined and 22876 nodes are used in this test and the incremental load of displacement is fixed as $\Delta u = 1 \times 10^{-5} mm$.

The results of simulation by case 1 and 2 are presented as in Figure II .8 and Figure II .9. In both of the results, unlikely the symmetric crack branches form [Miehe et al., 2010b] simulated by isotropic phase-field model, there is only one crack propagates towards to the lower-right angle of the plate. This means that our model accurately avoids cracks in the compressed elements. The crack path reproduces the result of Bourdin[Bourdin et al., 2000], the principal feature of the result is that the angle between the initial crack and the propagated crack $\beta = 61^o$.

In case 1(Figure II .8), the main crack propagated is the tensile one. Because in this shear test, the shear crack always appears under the condition of expansion. We consider this exposed shear crack is a part of the tensile crack in our model. So the compressed shear crack isn't produced during the test(bot images of Figure II .8).
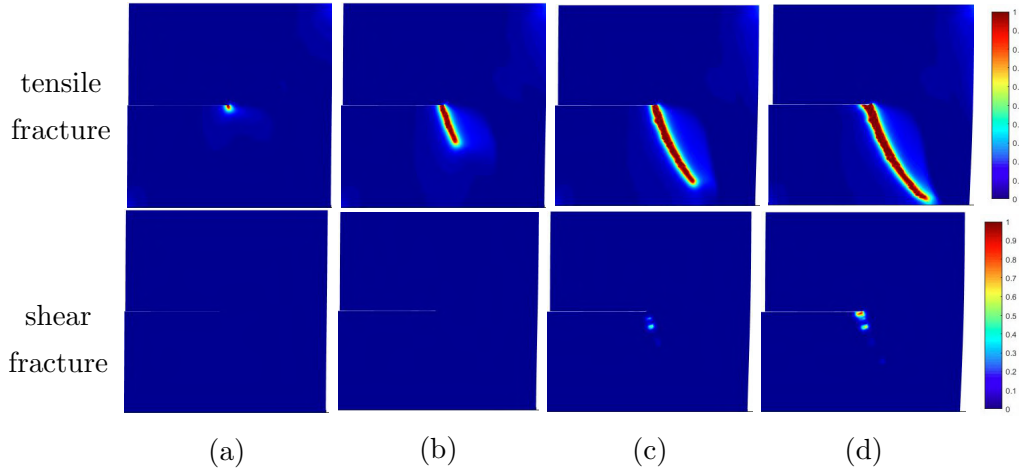
Figure II .8: Single-edge notched shear test simulated by case 1. Crack path at the load of displacement: (a)$u = 1 \times 10^{-2}mm$; (b)$u = 1.5 \times 10^{-2}mm$; (c)$u = 2 \times 10^{-2}mm$;(d)$u = 2.5 \times 10^{-2}mm$.

In case 2(Figure II .9), both of the two types of crack propagate. We explain this propagation as that: the shear crack propagates at first. And then, the stiffness matrix is reduced by the effect of the shear crack. At last, it conduits to the tensile crack propagates following the same path. As we can see, the global process of propagation is caused by the interaction between both of two types of crack.
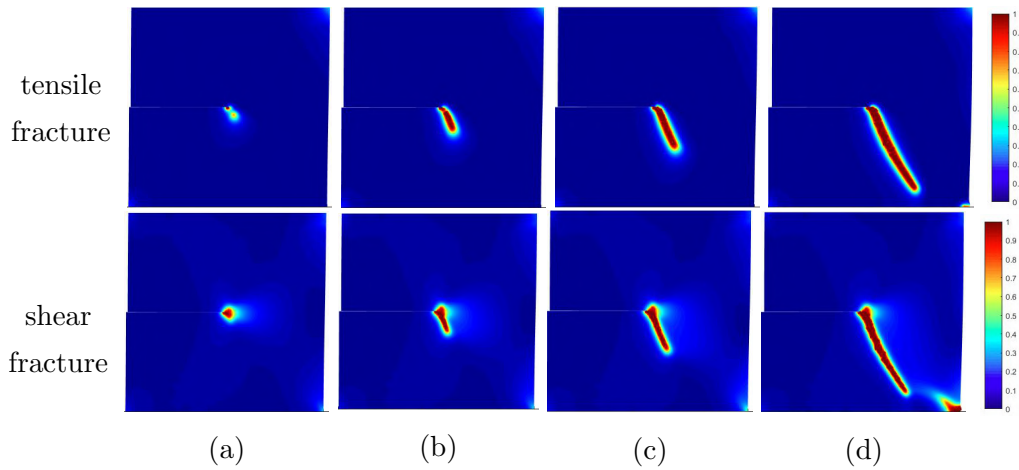
Figure II .9: Single-edge notched shear test simulated by case 2. Crack path at the load of displacement: (a)$u = 1 \times 10^{-2}mm$; (b)$u = 1.5 \times 10^{-2}mm$; (c)$u = 2 \times 10^{-2}mm$;(d)$u = 2.5 \times 10^{-2}mm$.

The results simulated by case 3 is shown as in the Figure II .10. The main crack

propagated is the tensile one. We consider this exposed shear crack is a part of the tensile crack in our model. Unlikely the symmetric crack branches form [Miehe et al., 2010b] simulated by isotropic phase-field model, there is only one crack propagates towards to the lower-right angle of the plate. This means that our model accurately avoids cracks in the compressed elements. The crack path reproduces the result of Bourdin [Bourdin et al., 2000], the principal feature of the result is that the angle between the initial crack and the propagated crack $\beta = 61^o$.
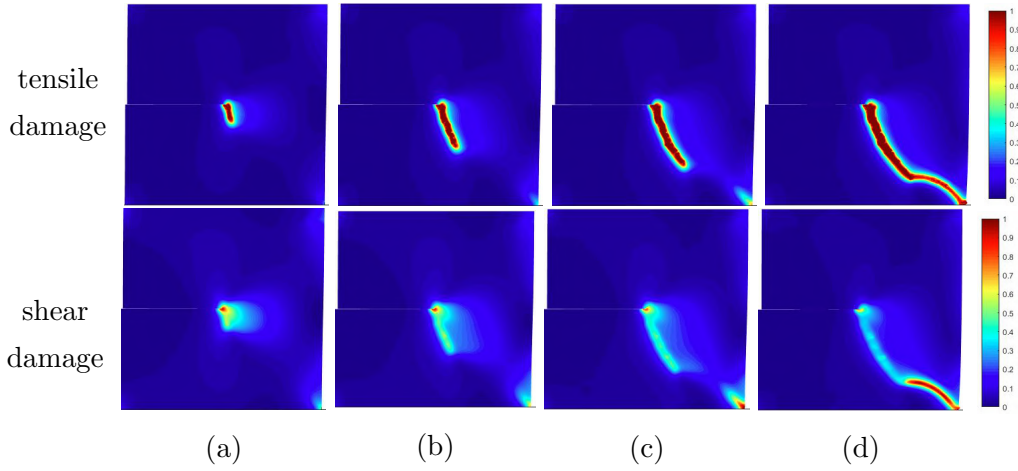
Figure II .10: Single-edge notched shear test simulated by case 3. Crack path at the load of displacement: (a)$u = 1 \times 10^{-2}mm$; (b)$u = 1.5 \times 10^{-2}mm$; (c)$u = 2 \times 10^{-2}mm$;(d)$u = 2.5 \times 10^{-2}mm$.

Compared with the results of Miehe model and Amor model as shown in Figure II .11. Amor model and our model have the second crack propagated from the lower-right angle of the sample near the end of the test. And this second crack connects the main crack at the end. But it isn't appeared in Miehe model. Because in Miehe model, the compressed shear energy isn't considered as the crack driving quantity, and this compressed shear energy conduits to the appearance of the second crack. Compare the results of our model with the Amor model, the locations at which the two cracks intersect are different. The shear crack propagates the longer distance in our model. This behavior depends on the value of g_c^{sh}. Amor model can be seen as a special situation of our model under the condition $g_c^{sh} = +\infty$. In this simulation by our model, the g_c^{sh} is defined as a real value which is enough small compared with $+\infty$. It means that the material has lower ability to resist the propagation of shear crack.
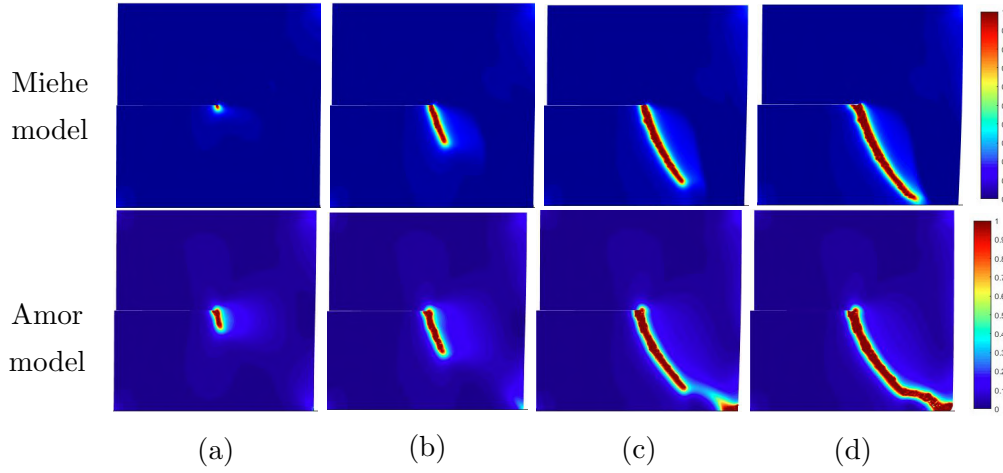
Figure II .11: Single-edge notched shear test simulated by Miehe model and Amor model. Crack path at the load of displacement: (a)$u = 1 \times 10^{-2}mm$; (b)$u = 1.5 \times 10^{-2}mm$; (c)$u = 2 \times 10^{-2}mm$;(d)$u = 2.5 \times 10^{-2}mm$.

Figure II .12 shows the relation of reaction and displacement. Compared with other models, the curve of case 1 is quite similar to the result of Miehe p-f model. But there's some reactions vibrated after the peak, which is because that there's the change between expansion and compression condition appears at the area of high tensile damaged zone. The stiffness matrix recovers to the low damaged state when there's the change from expansion condition to compression condition. In case 2, it overcomes this issue. The peak of case 2 curve is a little higher than the others, which is because that the definition of g_c^t and g_c^{sh} is not the same. In other model, they have only g_c^t to present the resistance of tensile crack, but in case 2, this resistance should be reduced and separated to the every types of the damage resistance. Here, we only use the same parameters to compare the curves. And the curve of case 2 has the same trend compare with Amor phase-field model. Figure II .12(b) shows the relation of reaction and displacement. The appearance of second crack brings different curves. Amor model and our model have the same shape, and they differ from the curve of Miehe model.
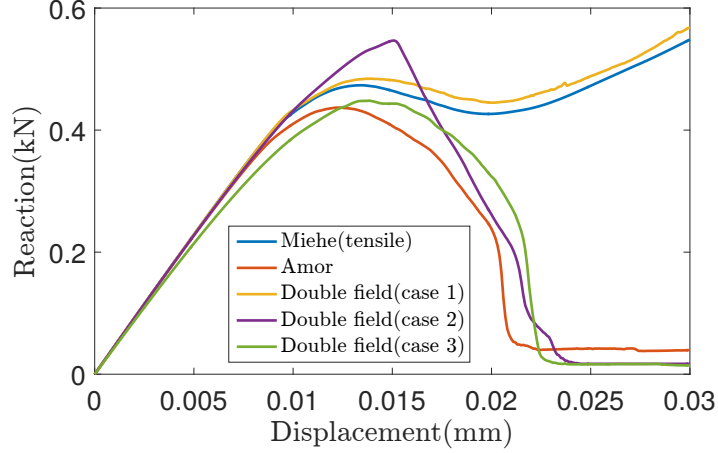
Figure II .12: Single-edge notched shear test. Reaction-displacement curve.

4.3 Triaxial compression test of sandstone

In the first triaxial compression test. The experimental tests of sandstone were performed in Laboratory of Mechanics of Lille, France. In these conventional triaxial tests, the cylindrical samples of 37 mm in diameter and 74 mm in height are used under the confining pressures of 5, 20, 40 and 60 MPa. It can be obtained from the results that the Young's modulus of sample increases from 15 to 18 GPa with the confining pressure changing from 5 to 60 MPa. And the Poisson's ratio is 0.25.

In the simulation, the sandstone is considered as a isotropic material. The geometry and boundary condition are presented as in the Figure II .13. The mesh containing 20000 elements and 20301 nodes and the incremental load of displacement $\Delta u = 1 \times 10^{-3} mm$. The width of the diffusive crack $l_d = 0.37mm$ which equals to the dimension of the smallest element. In our elasticity-damage model, elastic field couldn't reflect the influence of confinement. The popular way in phase-field method is increasing the value of $g_c^t \& g_c^{sh}$ to describe the higher crack resistance of the material under the higher confinement. But there's no convincing mathematical expression between them yet. In these simulations, $g_c^t \& g_c^{sh}$ used increase from 0.01kN/mm to 0.055kN/mm with the confining pressure changing from 5 to 60 MPa. To facilitate inhomogeneous deformation, we define a weak region at the red zone in the Figure II .13, in this region, the g_c^t and g_c^{sh} are reduced to 1%.
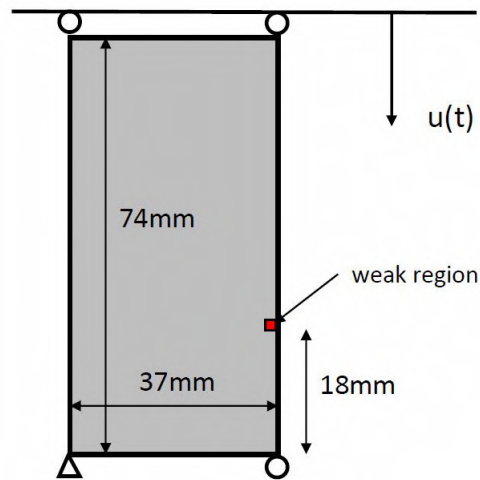
Figure II .13: The dimension and the boundary conditions of triaxial compression test.

The Figure II .14 presents the result of stress-strain curves compared with experimental results. It is observed that the peak of differential stress significantly increases with the increase of confining pressure. This effect of confining pressure is correctly reproduced by the numerical model. Unfortunately, due to the technical limit of experimental device, the mechanical responses in the post-peak regime are not available in the laboratory tests.
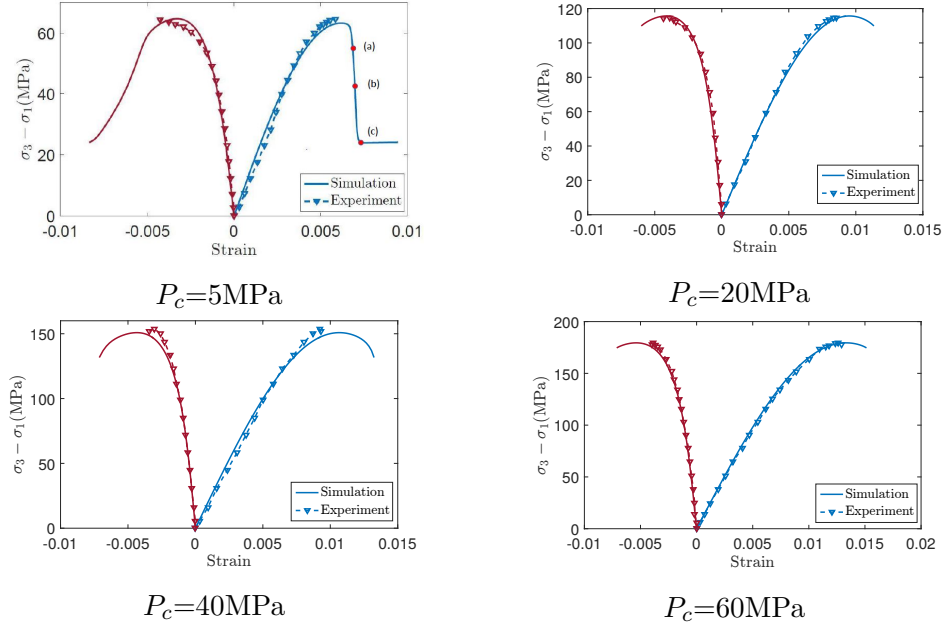
Figure II .14: Axial (blue) and lateral (red) strain versus differential stress in conventional compression tests with different confining pressures P_c=5, 20, 40, 60MPa: comparison between numerical results (continuous lines) and LML experiment data(dotted line).

The Figure II .15 shows the result of crack path during the test under 5MPa confinement. First, during the compression process, the shear damage values of all the nodes of the sample increase, but there's no tensile damage produced. According to the weak region that can be considered as the zone with lower crack resistance, two damage bands are formed in the shear fracture field. And then, the value d^{sh} increases in two band. Upon further loading, the fracture is developed from the weak region. Due to this shear fracture, some tensile fracture are gradually formed around the shear one.
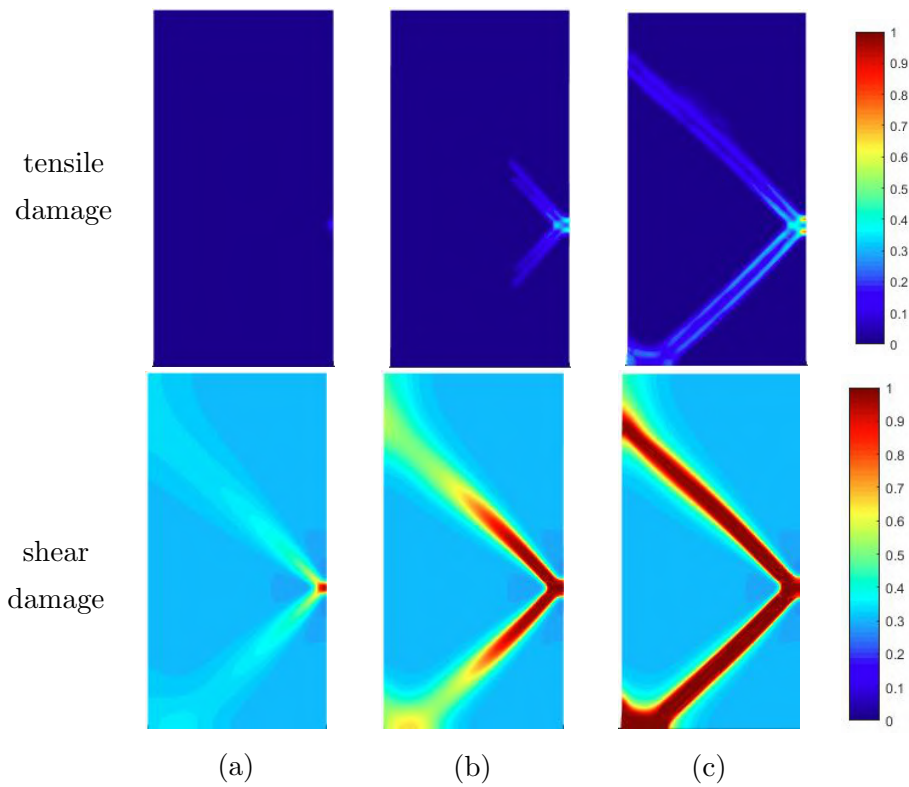
Figure II .15: Triaxial compression test on sandstone under P_c=5MPa. Crack path at the load of displacement: (a)$u = 0.51mm$; (b)$u = 0.516mm$; (c)$u = 0.52mm$ (the 3 points displayed in figure 10, P_c=5MPa).

Figure II .16 shows the results of the simulation with the weak region above the middle right side of the sample. The distribution of cracks is similar except for the reverse.
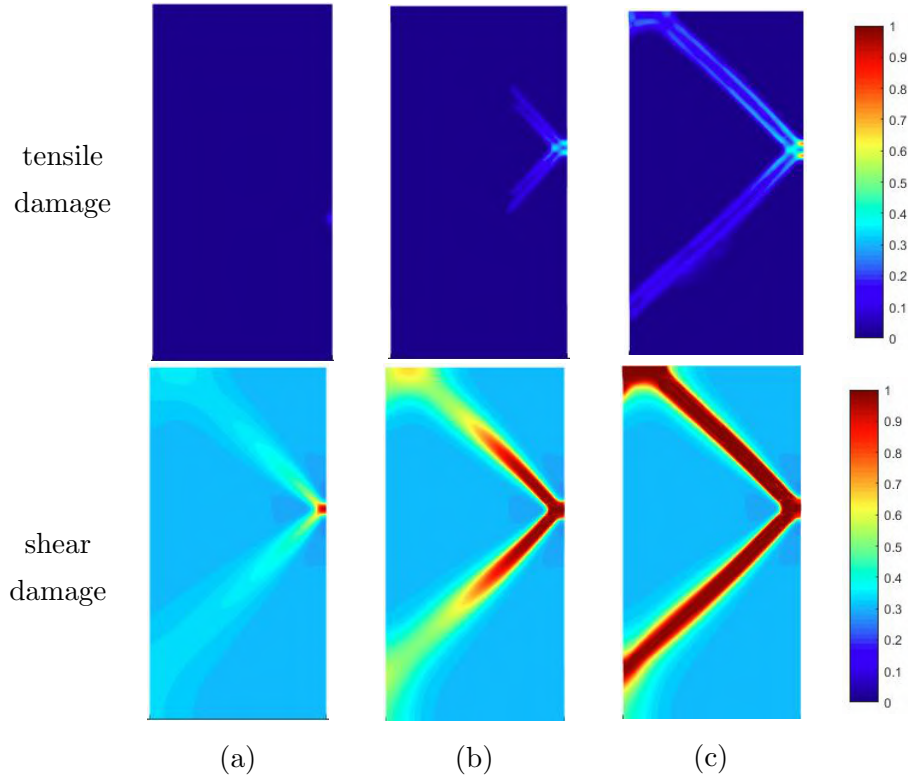
Figure II .16: Triaxial compression test on sandstone under P_c=5MPa. Crack path at the load of displacement: (a)$u = 0.51mm$; (b)$u = 0.516mm$; (c)$u = 0.52mm$ (the 3 points displayed in figure 10, P_c=5MPa).

In the phase-field model, the size of the effective elements does not have much effect on the results. The results simulated by a coarse mesh with 5000 elements is used to compared with the results simulated by the fine mesh(20000 elements) as in the Figure II .17.
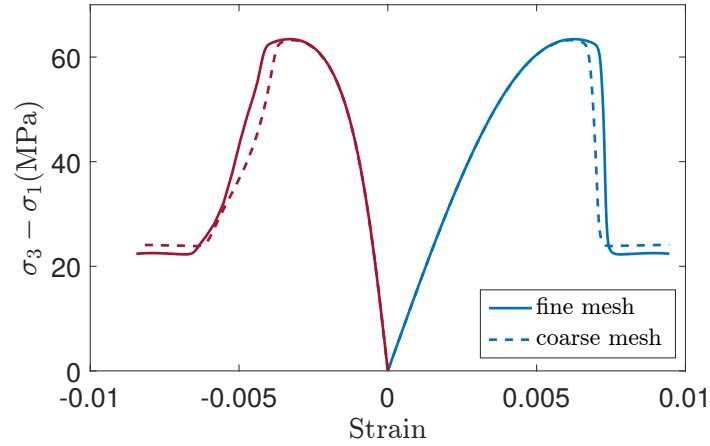
Figure II .17: Axial (blue) and lateral (red) stress-strain curves of 5MPa confinement test: comparison between coarse mesh (dotted line) and fine mesh (continuous lines).

In this simulation, the incremental displacement Δu plays an important role. We compare the results simulated by different Δu as in the Figure II .18. The small Δu is necessary to reduce the residue of coupling between the mechanical field and damage fields, especially in the period with quickly producing of damage. This period is expressed as a portion after the peak in the stress-strain curves.
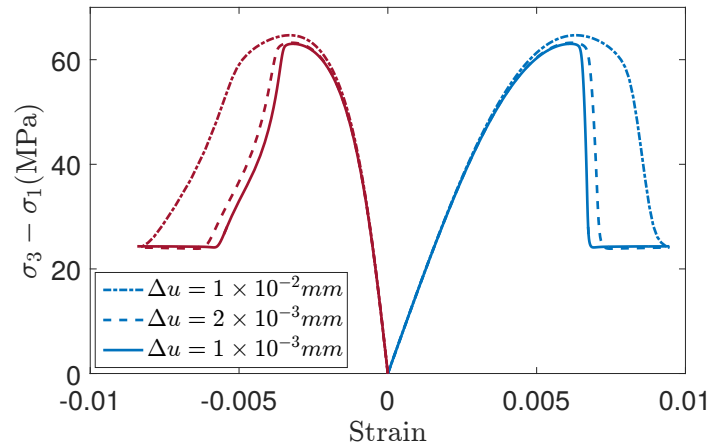
Figure II .18: Axial (blue) and lateral (red) stress-strain curves of 5MPa confinement test: comparison between different load steps: $\Delta u = 1 \times 10^{-2} mm$ (dash-dotted line) $\Delta u = 2 \times 10^{-3} mm$ (dotted line) and $\Delta u = 1 \times 10^{-3} mm$ (continuous lines).

According to our model, the compressed shear energy are considered as the driving quantity to create the shear fracture. This is a new way to simulate the compression test by phase-field method.

4.4   Triaxial compression test of Jinping marble

In order to compare the post-peak of stress-strain curve in the triaxial compression test, we simulate triaxaial mechanical behavior of Jinping marble under confining pressure $P_c =$4, 10, 20, 30 MPa [Liu and Shao, 2017]. The sample used has the same dimension of $74mm \times 37mm$ with a weak region as in the Figure II .13. The Young modulus and Poisson's ratio of the sample are 30 GPa and 0.15. The same mesh is used as the previous test of sandstone. The incremental load of displacement is $\Delta u = 1 \times 10^{-3} mm$ and the width of the diffusive crack $l_d = 0.37mm$.

The stress-strain relations of these tests are presented in the Figure II .20. According to the use of the parameter β_2 of the degradation function of shear damage $h_3(d^{sh})$ (Figure II .19), the post-peak regions are well reproduced compared with the experiment results. The post-peak behavior can be explained as 2 parts. At first, minimum convergence differential stress increases slightly during confining pressure increase. We interpret this convergence stress as the residual resistance of the damaged material. It can be mathematically reflected as the the degradation function $h_3(d^{sh} = 1) > 0$, so we can obtain the residual stiffness matrix in the totally broken material in the simulation. Secondly, the downward trend of the curve in the post-peak region becomes smooth during the increase of the confining pressure, which means that the speed of damage creation is slowed down in our simulation. It can be mathematically reflected as the damage driving energy is reduced by $h_3(d^{sh})$. In this way, our model is allowed to correctly predict the behavior of the brittle-ductile transition.

And the results also present the limit of our elastic-damage model, the lack of the consideration of plastic behaviors conduits to the differences at the pre-peak region especially under the high confining pressure.
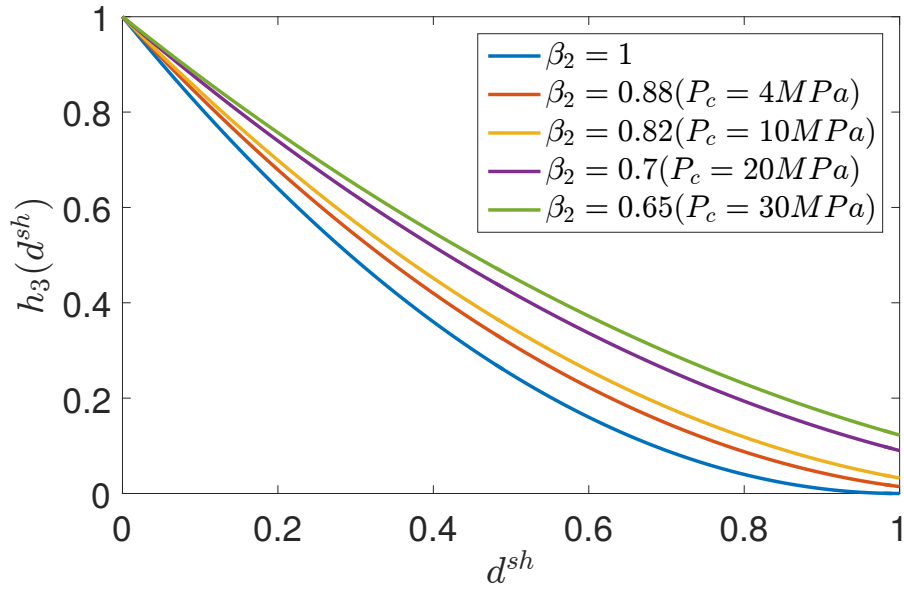
Figure II .19: The functions of degradation $h_3(d^{sh})$ used under confining pressures $P_c =4$, 10, 20, 30 MPa.

P_c=4MPa

P_c=10MPa

P_c=20MPa

P_c=30MPa
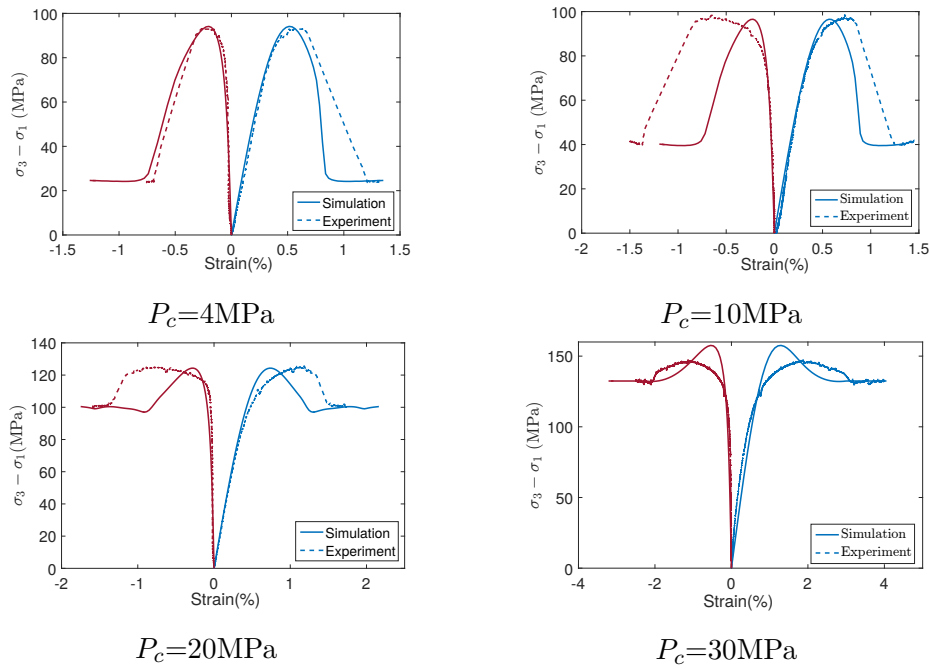
Figure II .20: Axial (blue) and lateral (red) strain versus differential stress in conventional compression tests with different confining pressures P_c=4, 10 ,20, 30MPa: comparison between numerical results (continuous lines) and experiment data [Liu and Shao, 2017] (dotted line)

The Figure II .21 presents the distribution of the damage at the failure state under the different confining pressures. The color of the not totally broken area in the distributions of shear damage is changed, which means that the average of shear damage value at the failure moment is different. Under the high confining pressure, it needs higher average damage to create the main damage. And the tensile damage can hardly be observed under the high confining pressure. This is another way to explain the behavior of the brittle-ductile transition.
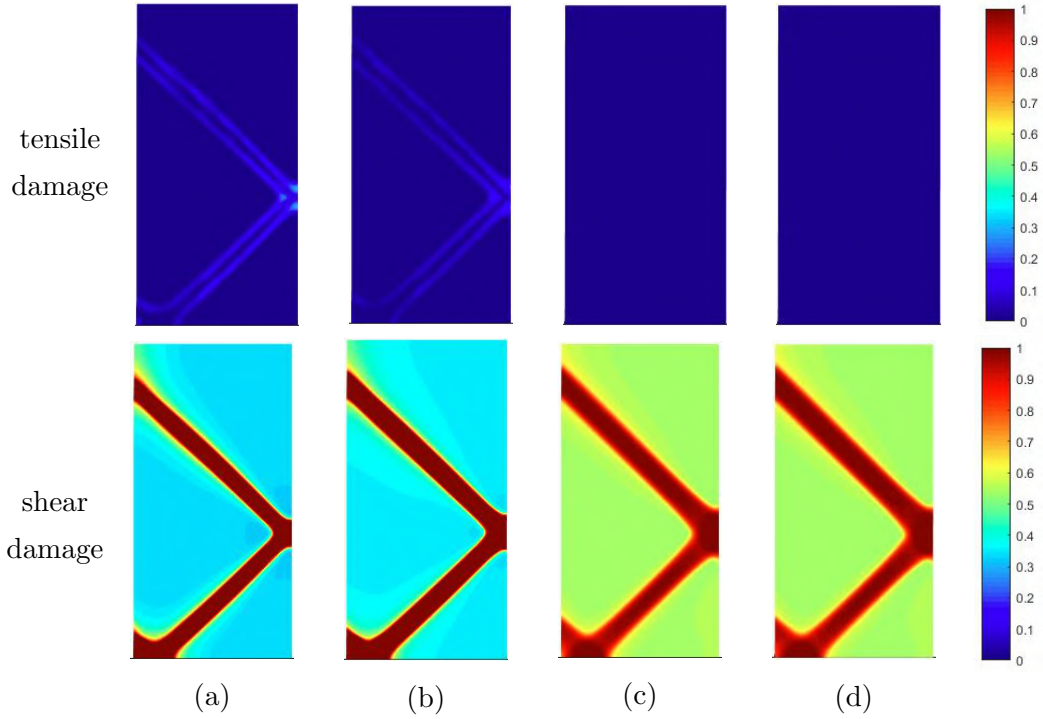
Figure II .21: Triaxial compression test on sandstone. Crack path at the load of displacement under different confining pressures: (a)$P_c = 4MPa$; (b)$P_c = 10MPa$; (c)$P_c = 20MPa$; (d)$P_c = 30MPa$.

5   Conclusion

In this Chapter, a double crack phase-field model is proposed for modeling damage and cracking process of cohesive brittle materials. Both tensile and shear cracks are taken into account. The two types of the crack path can be directly observed during the failure process. The two types of fracture behavior can be controlled by the adjustment of the degradation function and density resistance energy g_c^t and g_c^{sh}. With the elastic stiffness decomposition, the crack fields can be coupled with both isotropic and anisotropic elastic

materials.

Our model based on a new decomposition of driving energy has a good agreement in the benchmark problem compared with the other classic phase-field model.

Unlikely other phase-field model, our model works well in the triaxial compression test with brittle rock-like material such as sandstone and Jinping marble. The crack path can be reproduced under the elasticity-damage condition. It is found that under dominating compression stresses, the shear cracking is the main mechanism and the failure is induced mainly by the onset of localized shear bands. But as we all know that plastic deformation plays an important role for more ductile material, the elasto-plastic damage model would be considered with the double crack phase-field method in the next Chapter.

Chapter III

A double phase-field method for quasi-ductile rock-like materials

Contents

1   Introduction

In this Chapter, the double crack phase-field method, which is introduced in the previous chapter, is extended to describe the elastic-plastic damage behavior. Two independent crack-phase fields are introduced to account for the tensile and shear cracks respectively. Two boundary values problems are solved to determine the evolutions of these two crack phases, which are both coupled with plastic deformation. The regularized variational framework and the thermodynamics framework is defined to take into account the plastic effect. The weak forms of the finite element method are formulated to the solution of crack fields and displacement field with respect to the plastic function. A simplified numerical

algorithm is proposed to solve the three coupled fields. The proposed double field method is finally applied to study the mechanical behavior of clayey rocks by considering the transition from diffuse damage to localized cracking.

2 The double phase-field method for plastic materials

2.1 Regularized variational framework

In the framework of the variational approach to fracture mechanics proposed by Francfort and Marigo [1998], an energy functional was introduced and it is composed of the elastic strain energy and the energy requested to create the crack. With the regularized smeared crack topology presented above, the energy requested to create the sharp crack is approximated by that for the creation of regularized crack surfaces. Further, in the present study, plastic deformation of bulk material is also taken into account. The locked energy for plastic hardening is then added in the energy functional. Thus, the extended form of the total energy functional is given by:

$$
\begin{aligned}
E(\mathbf{u}, d^t, d^{sh}) &= E_u(\mathbf{u}, d^t, d^{sh}) + E_s(d^t, d^{sh}) \\
E_u(\mathbf{u}, d^t, d^{sh}) &= \int_\Omega W_e(\boldsymbol{\epsilon}^e(\mathbf{u}), d^t, d^{sh}) d\Omega + \int_\Omega W_p(\boldsymbol{\epsilon}^p(\mathbf{u}), d^t, d^{sh}) d\Omega \\
E_s(d^t, d^{sh}) &= g_c^t \int_\Omega \gamma^t(d^t, \nabla d^t) d\Omega + g_c^{sh} \int_\Omega \gamma^{sh}(d^{sh}, \nabla d^{sh}) d\Omega
\end{aligned}
\tag{III .1}
$$

W_e is the elastic strain energy of cracked material while W_p the locked energy for plastic hardening. The parameters g_c^t and g_c^{sh} are the material toughness respectively for tensile and shear cracks. Note that the total functional E can also be rewritten in the following form:

$$
E(\mathbf{u}, d^t, d^{sh}) = \int_\Omega W(\mathbf{u}, d^t, d^{sh}) d\Omega
\tag{III .2}
$$

with

$$
W(\mathbf{u}, d^t, d^{sh}) = W_e(\boldsymbol{\epsilon}^e(\mathbf{u}), d^t, d^{sh}) + W_p(\boldsymbol{\epsilon}^p(\mathbf{u}), d^t, d^{sh}) + g_c^t \gamma^t(d^t, \nabla d^t) + g_c^{sh} \gamma^{sh}(d^{sh}, \nabla d^{sh})
\tag{III .3}
$$

which can be identified as the free energy.

In order to take into account an anisotropic elastic behavior and the distinctive effects of tensile and shear cracks on the elastic properties of material, the elastic strain energy of undamaged material is decomposed into a spherical part and a deviatoric part:

$$
W_e^0(\boldsymbol{\epsilon}^e) = W_{sph}^0(\boldsymbol{\epsilon}^e) + W_{dev}^0(\boldsymbol{\epsilon}^e) = \frac{1}{2} \boldsymbol{\epsilon}^e : \mathbb{C}_{sph}^0 : \boldsymbol{\epsilon}^e + \frac{1}{2} \boldsymbol{\epsilon}^e : \mathbb{C}_{dev}^0 : \boldsymbol{\epsilon}^e
\tag{III .4}
$$

The spherical and deviatoric elastic stiffness tensors $\mathbb{C}^0_{sph}$ and $\mathbb{C}^0_{dev}$ are defined as:

$$
\begin{cases}
\mathbb{C}^0_{sph} = k^0_{reuss} \mathbf{1} \bigotimes \mathbf{1}; \\
\\
\mathbb{C}^0_{dev} = \mathbb{C}^0 - \mathbb{C}^0_{sph}
\end{cases}
\tag{III .5}
$$

$\mathbb{C}^0$ denotes the total initial elastic stiffness tensor of undamaged material and k^0_{reuss} is the so-called Reuss bulk modulus. Compared with other decompositions of elastic tensors [Miehe et al., 2010b], the present one is particularly suitable for anisotropic elastic materials. In order to distinguish the different effects of open and closed cracks, the following crack status coefficient $r^{\pm}_e$ is introduced:

$$
\begin{cases}
\text{if } tr(\boldsymbol{\epsilon}^e) >= 0 : \ r^+_e = 1, \ r^-_e = 0 \\
\\
\text{if } tr(\boldsymbol{\epsilon}^e) < 0 : \ r^+_e = 0, \ r^-_e = 1
\end{cases}
\tag{III .6}
$$

The elastic properties of material are progressively deteriorated by induced cracks. This is interpreted by the progressive degradation of the elastic stiffness tensor through the following relations:

$$
W_e(\boldsymbol{\epsilon}^e, d^t, d^{sh}) = \{r^+_e h_1(d^t) + r^-_e\}W^0_{sph} + \{r^+_e h_2(d^t)h_3(d^{sh}) + r^-_e h_3(d^{sh})\}W^0_{dev} \tag{III .7}
$$

It is assumed that the degradation functions $h_{1-3}(d^t, d^{sh})$ take the following forms:

$$
\begin{cases}
h_1(d^t) = (1 - \beta_1 d^t)^2 \\
\\
h_2(d^t) = (1 - \beta_2 d^t)^2 \\
\\
h_3(d^{sh}) = (1 - \beta_3 d^{sh})^2
\end{cases}
\tag{III .8}
$$

The parameters β_1, β_2 and β_3 are used to reflect the residual elastic stiffness of damaged material. The physical interpretation of elastic energy decomposition with respect to degradation by open and closed cracks is illustrated in Figure III .1.

spheric/deviatoric	open/closed	mode	degradation
spheric energy	open crack		$h_1(d^t)$
	closed crack		-
deviatoric energy	open crack		$h_2(d^t)h_3(d^{sh})$
	closed crack		$h_3(d^{sh})$

Figure III .1: Physical interpretation of elastic energy decomposition with respect to degradation by open and closed cracks

The work related to plastic strain is generally composed of two parts: the plastic dissipation and the locked energy for plastic hardening W_p. The locked energy is assumed to contribute to the total energy functional. For the sake of simplicity, the locked plastic energy is calculated as a part of the total plastic work. For the undamaged material, one has:

$$\dot{W}_p^0(\dot{\boldsymbol{\epsilon}}^p) = (1 - \eta)\boldsymbol{\sigma} : \dot{\boldsymbol{\epsilon}}^p \tag{III .9}$$

$0 \leqslant \eta \leqslant 1$ is the so-called Taylor-Quinny coefficient used to determine the ratio of locked energy to the total plastic work. The effect of locked plastic energy on the phase-field evolutions also depends on the crack status. Therefore, the following crack status coefficient

is introduced:

$$\begin{cases} \text{if } tr(\boldsymbol{\epsilon}^p) >= 0 : \ r_p^+ = 1, \ r_p^- = 0 \\ \\ \text{if } tr(\boldsymbol{\epsilon}^p) < 0 : \ r_p^+ = 0, \ r_p^- = 1 \end{cases} \qquad \text{(III .10)}$$

Finally, the contribution of locked plastic energy to the total energy functional is given by:

$$\dot{W}_p = \{r_p^+ h_2(d^t)h_3(d^{sh}) + r_p^- h_3(d^{sh})\}\dot{W}_p^0 \qquad \text{(III .11)}$$

The accumulated value of locked plastic energy W_p is obtained by the summation of each incremental value during loading history.

2.2 Evolution of crack phase fields

It is assumed that the total strain rate verifies the following partition rule: $\boldsymbol{\epsilon} = \boldsymbol{\epsilon}^e + \boldsymbol{\epsilon}^p$. Further, with the assumption of isothermal conditions, the Clausius-Duhem inequality can be written as:

$$\mathcal{D} = \boldsymbol{\sigma} : (\dot{\boldsymbol{\epsilon}}^e + \dot{\boldsymbol{\epsilon}}^p) - \dot{W}_p - \dot{W} \geqslant 0 \qquad \text{(III .12)}$$

It is assumed that the dissipations related to plastic strain and crack growth are respectively positive. Hence, one gets:

$$\boldsymbol{\sigma} = \frac{\partial W}{\partial \boldsymbol{\epsilon}^e} = [r_e^+ h_1(d^t) + r_e^-]\mathbb{C}_{sph}^0 : \boldsymbol{\epsilon}^e + [r_e^+ h_2(d^t)h_3(d^{sh}) + r_e^- h_3(d^{sh})]\mathbb{C}_{dev}^0 : \boldsymbol{\epsilon}^e \quad \text{(III .13)}$$

$$\boldsymbol{\sigma} : \dot{\boldsymbol{\epsilon}}^p - \dot{W}_p \geqslant 0 \qquad \text{(III .14)}$$

$$\mathcal{A}^\alpha \dot{d}^\alpha \geqslant 0 \qquad \text{(III .15)}$$

$\mathcal{A}^\alpha = -\frac{\partial W}{\partial d^\alpha}$ is the thermodynamic force associated with the crack phase field d^α ($\alpha = t, sh$). Further, it is assumed that the threshold function $F^\alpha(\mathcal{A}^\alpha)$ governing the crack phase field evolution is simply written as:

$$F^\alpha(\mathcal{A}^\alpha) = \mathcal{A}^\alpha \leq 0 \qquad \text{(III .16)}$$

Taking into account the irreversible condition of crack growth, one gets for $\dot{d}^\alpha > 0$, $F^\alpha = 0$. It is:

$$F^\alpha = -\{\frac{\partial(W_e + W_p)}{\partial d^\alpha} + g_c^\alpha \delta\gamma^\alpha(d^\alpha)\} = 0 \qquad \text{(III .17)}$$

where $\delta\gamma^\alpha(d^\alpha)$ is the variational derivative of the crack density function [Miehe et al., 2010b]. By considering the definitions of different parts of energy in Eq. III .3, one gets:

$$\begin{cases} -r_e^+ h_1' W_{sph}^0 - h_2' h_3 (r_e^+ W_{dev}^0 + r_p^+ W_p^0) - g_c^t(\frac{1}{l_d} d^t - l_d^2 \Delta d^t) \leq 0 \\ \\ -h_3'[r_e^+ h_2 W_{dev}^0 + r_e^- W_{dev}^0 + r_p^- W_p^0] - g_c^{sh}(\frac{1}{l_d} d^{sh} - l_d^2 \Delta d^{sh}) \leq 0 \end{cases} \tag{III .18}$$

In order to consider complex loading paths with unloading and reloading cycles and considering that the crack growth is an irreversible process, a strain history functional has been introduced in Miehe et al. [2010b]. Inspired by this, in this study, three energy history functionals are defined as follows:

$$\begin{cases} \mathcal{H}_{sph} = max[r_e^+ W_{sph}^0] \\ \\ \mathcal{H}_{dev}^t = max[h_3(r_e^+ W_{dev}^0 + r_p^+ W_p^0)] \\ \\ \mathcal{H}_{dev}^{sh} = max[r_e^+ h_2 W_{dev}^0 + r_e^- W_{dev}^0 + r_p^- W_p^0] \end{cases} \tag{III .19}$$

With these energy history functionals at hand, the evolutions of crack phase fields are determined by the following criteria:

$$\begin{cases} -h_1' \mathcal{H}_{sph} - h_2' \mathcal{H}_{dev}^t - g_c^t(\frac{1}{l_d} d^t - l_d^2 \Delta d^t) = 0 \\ -h_3' \mathcal{H}_{dev}^{sh} - g_c^{sh}(\frac{1}{l_d} d^{sh} - l_d^2 \Delta d^{sh}) = 0 \end{cases} \tag{III .20}$$

3   Numerical implementation in finite element method

We consider here two crack phase fields in the solid body Ω subjected to the body force $\mathbf{f}_b$ in Ω, the surface force $\mathbf{t}_N$ on its boundary $\partial\Omega_f$ and the prescribed displacement $\overline{\mathbf{u}}$ on its boundary $\partial\Omega_u$, as shown in Figure II .2. The total potential energy can be written as:

$$\Pi = E(\mathbf{u}, d^t, d^{sh}) - \int_\Omega \mathbf{f}_b \cdot \mathbf{u} d\Omega - \int_{\partial\Omega_f} \mathbf{t}_N \cdot \mathbf{u} dA \tag{III .21}$$

The stationarity condition of the potential energy $\delta\Pi = 0$ leads to three coupled boundary values problems respectively for the displacement field, the tensile crack phase field and the shear crack phase field.

The local equations for the displacement field are written as:

$$\begin{cases} \nabla \cdot \boldsymbol{\sigma} + \mathbf{f}_b = 0 & \text{in } \Omega \\ \boldsymbol{\sigma} \cdot \mathbf{n} = \mathbf{t}_N & \text{on } \partial\Omega_t \end{cases} \tag{III .22}$$

With the help of shape functions and related derivatives in finite elements, one obtains the discrete weak form for the displacement field for the current loading step:

$$\begin{cases} \mathbf{K}_u \triangle \mathbf{U} = \triangle \mathbf{F} \\\\ \mathbf{K}_u = \int_\Omega \mathbf{B}_u^T \mathbb{C} \mathbf{B}_u d\Omega \\\\ \triangle \mathbf{F} = \int_\Omega \mathbf{N}_u^T \triangle \mathbf{f}_b d\Omega + \int_{\partial \Omega_f} \mathbf{N}_u^T \triangle \mathbf{t}_N dA \end{cases} \tag{III .23}$$

$\mathbf{N}_u$ and $\mathbf{B}_u$ are respectively the matrix of shape functions and related derivatives of displacement components. $\mathbf{K}_u$ is the global stiffness matrix. $\triangle \mathbf{U}$ and $\triangle \mathbf{F}$ respectively denote the column matrix of increment nodal displacements and forces. The current elastic stiffness matrix of cracked material is given by:

$$\mathbb{C}(d^t, d^{sh}) = [r_e^+ h_1 + r_e^-] \mathbb{C}_{sph}^0 + [r_e^+ h_2 h_3 + r_e^- h_3] \mathbb{C}_{dev}^0 \tag{III .24}$$

For the tensile crack phase field, one has the following local equations:

$$\begin{cases} h_1' \mathcal{H}_{sph} + h_2' \mathcal{H}_{dev}^t + g_c^t(\frac{1}{l_d} d^t - l_d^2 \Delta d^t) = 0 \quad \text{in } \Omega \\ \dot{d}^t \geq 0 \quad \text{in } \Omega \\ d^t = 1 \quad \text{on } \Gamma^t \\ \nabla d^t \cdot \mathbf{n} = 0 \quad \text{on } \partial \Omega \end{cases} \tag{III .25}$$

and for the shear crack phase field:

$$\begin{cases} h_3' \mathcal{H}_{dev}^{sh} + g_c^{sh}(\frac{1}{l_d} d^{sh} - l_d^2 \Delta d^{sh}) = 0 \quad \text{in } \Omega \\ \dot{d}^{sh} \geq 0 \quad \text{in } \Omega \\ d^{sh} = 1 \quad \text{on } \Gamma^{sh} \\ \nabla d^{sh} \cdot \mathbf{n} = 0 \quad \text{on } \partial \Omega \end{cases} \tag{III .26}$$

Similar to the displacement field, the two crack phase fields and their gradients inside each element are also approximated by the nodal values by using appropriate shape functions and related derivatives. With such approximations, the weak forms and discrete systems of equations are obtained for each crack phase field. Namely, for the tensile cracks field, one gets:

$$\begin{cases} \mathbf{K}_{d^t} \mathbf{d}^t = \mathbf{F}_{d^t} \\\\ \mathbf{K}_{d^t} = \int_\Omega \{ (g_c^t \, l_d + 2\beta_1^2 \mathcal{H}_{sph} + 2\beta_2^2 \mathcal{H}_{dev}^t) \mathbf{N}_d^T \mathbf{N}_d + g_c^t l_d \mathbf{B}_d^T \mathbf{B}_d \} d\Omega \\\\ \mathbf{F}_{d^t} = \int_\Omega 2(\beta_1 \mathcal{H}_{sph} + \beta_2 \mathcal{H}_{sph}^t) \mathbf{N}_d^T d\Omega \end{cases} \tag{III .27}$$

and for the shear crack field:

$$
\begin{cases}
\mathbf{K}_{d^{sh}}\mathbf{d}^{sh} = \mathbf{F}_{d^{sh}} \\[2ex]
\mathbf{K}_{d^{sh}} = \int_{\Omega}\{(g_c^t\ l_d + 2\beta_3^2\mathcal{H}_{dev}^{sh})\mathbf{N}_d^T\mathbf{N}_d + g_c^t l_d\mathbf{B}_d^T\mathbf{B}_d\}d\Omega \\[2ex]
\mathbf{F}_{d^{sh}} = \int_{\Omega} 2\beta_3\mathcal{H}_{dev}^{sh}\mathbf{N}_d^T d\Omega
\end{cases}
\qquad\text{(III .28)}
$$

$\mathbf{N}_d$ and $\mathbf{B}_d$ are the shape functions and related derivatives for two crack phase fields.

It is obvious that three fields are coupled. The calculation of displacement field is influenced by the crack phase fields due to the fact that the elastic stiffness matrix $\mathbb{C}(\mathbf{x})$ is a function of $d^t(\mathbf{x})$ and $d^{sh}(\mathbf{x})$. On the other hand, the evolutions of crack fields are controlled by the energy history functionals which are functions of elastic and plastic strains. Moreover, in this study, the plastic strain of material is considered. For most geomaterials, a non-associated plastic flow rule is generally needed. The incremental plastic strain is calculated by the following general constitutive relations.

$$
\begin{cases}
f_p(\boldsymbol{\sigma};\gamma_p) \leq 0 \\[2ex]
\dot{\boldsymbol{\epsilon}}^p f_p = 0 \\[2ex]
\dot{\boldsymbol{\epsilon}}^p = \dot{\lambda}^p\frac{\partial G_p(\boldsymbol{\sigma})}{\partial\boldsymbol{\sigma}}
\end{cases}
$$

f_p and G_p are respectively the yield function and plastic potential. γ_p is an internal plastic hardening variable. λ^p is the positive plastic multiplier.

The loading history is divided into a number of incremental steps. At each loading step, three coupled nonlinear problems are to be solved. In this study and based on some previous studies, a simplified decoupled algorithm is adopted. At each loading step, the displacement field is first solved by using the values of crack fields obtained at the end of the previous stop. However, due to the plastic deformation, even the crack fields are frozen, an iterative procedure is still necessary to solve the nonlinear mechanical problem. After the determination of displacement, stress and strain fields, the values of energy history functionals are evaluated and the two crack fields are updated separately. A brief

summary of the algorithm is presented below.

Algorithm 1: Simplified algorithm for loading step $i + 1$

> **Input:** ϵ_e^i, ϵ_p^i, σ^i, γ_p^i, $\mathbf{d}_i^t$, $\mathbf{d}_i^{sh}$
>
> **Output:** ϵ_e^{i+1}, ϵ_p^{i+1}, σ^{i+1}, γ_p^{i+1}, $\mathbf{d}_{i+1}^t$, $\mathbf{d}_{i+1}^{sh}$
>
> **for** $m = 1...n_{iter}$ **do**
>
>> update nodal force: $\Delta \mathbf{f}^m = \Delta \mathbf{f}_{i+1} + \Delta \mathbf{f}_r^{m-1}$
>>
>> calculate nodal displacement increment: $\Delta \mathbf{U}^m = \mathbf{K}_u^{-1}(\mathbf{d}_i^t, \mathbf{d}_i^{sh}) \Delta \mathbf{F}^m$
>>
>> update strains: $\Delta \epsilon^m = \mathbf{B} \Delta \mathbf{U}^m$; $\Delta \epsilon_e^m = \Delta \epsilon^m - \Delta \epsilon_p^{m-1}$
>>
>> calculate elastic trial stress: $\sigma_{i+1}^{m-tri} = \sigma_i + \mathbb{C}(\mathbf{d}_i^t, \mathbf{d}_i^{sh}) : \Delta \epsilon_e^m$
>>
>> internal iteration for plastic strain calculation: $\Delta \epsilon_p^m$
>
> **end for**
>
> update plastic strain and hardening variable: $\epsilon_p^{i+1} = \epsilon_p^i + \Delta \epsilon_p^{i+1}$; $\gamma_p^{i+1} = \gamma_p^i + \Delta \gamma_p^{i+1}$
>
> update elastic strain: $\epsilon_e^{i+1} = \epsilon_e^i + (\Delta \epsilon^{i+1} - \Delta \epsilon_p^{i+1})$
>
> update stress: $\sigma_{i+1} = \sigma_i + \mathbb{C}(\mathbf{d}_i^t, \mathbf{d}_i^{sh}) : \Delta \epsilon_e^{i+1}$
>
> calculate energy history functionals:
>
> $\mathcal{H}_{sph}(\epsilon_e^{i+1})$, $\mathcal{H}_{dev}^t(\epsilon_e^{i+1}, \epsilon_p^{i+1}, \sigma^{i+1})$, $\mathcal{H}_{dev}^{sh}(\epsilon_e^{i+1}, \epsilon_p^{i+1}, \sigma^{i+1})$
>
> update crack phase fields: $\mathbf{d}_{i+1}^t$ and $\mathbf{d}_{i+1}^{sh}$

During the calculation of displacement field, the stiffness matrix $\mathbb{C}$ is influenced by d^t and d^{sh}; on the other side, the damage degrees d^t and d^{sh} are solved by the damage driving energy which is dependent on the elastic and plastic strain.

4 Numerical experiments

In this section, the prosed double crack phase fields model is applied to studying the mechanical behavior of a typical cohesive brittle material, the Callovo-Oxfordian claystone. This rock has been widely investigated in the framework of geological disposal of nuclear waste in France [Armand et al., 2017, 2013]. In this study, the objective is to reproduce the full mechanical response during triaxial compression tests by considering the nucleation, propagation and coalescence of micro-cracks. Consequently, both pre- and post-peak responses are investigated with the help of two crack phase fields.

The plastic behavior of claystone is described by a very simple model including the Drucker-Prager linear yield function, an isotropic hardening law and a non-associated

plastic potential. They are summarized as follows:

$$
\begin{cases}
\text{Yield function: } f_p = q + \alpha_p(p - C) \leq 0 \\[2ex]
\text{Hardening law: } \alpha_p = \alpha_0 + (\alpha_m - \alpha_0)\frac{\gamma_p}{B+\gamma_p} \\[2ex]
\text{Plastic potential: } G = q + (C - p)ln(\frac{C-p}{P})
\end{cases}
\tag{III .29}
$$

$p = tr(\boldsymbol{\sigma})/3$ is the mean stress. $q = \sqrt{2(\mathbf{s} : \mathbf{s})/3}$ is the equivalent shear stress (called deviatoric stress), with $\mathbf{s}$ being the deviatoric stress tensor. C is the yield threshold in hydrostatic tension. α_p denotes the current frictional coefficient varying from the initial value α_0 to the asymptotic one α_m. The parameter B controls the plastic hardening rate.
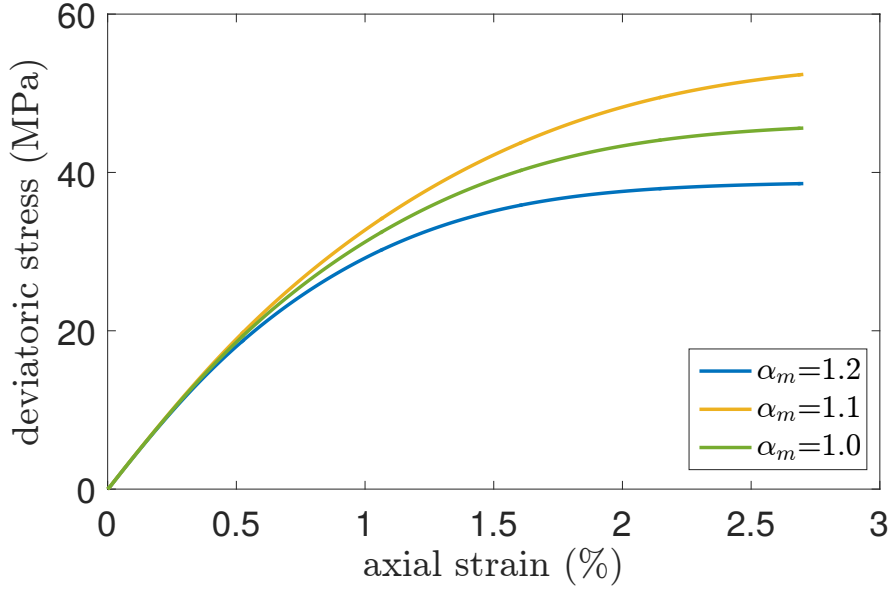
Figure III .2: The stress-strain curves of a uniaxial compression test. The elasto-plastic model only considers hardening function.

4.1   Tri-axial compression test simulated under plan strain condition

At first, we concern to study the sensitivity of different confining pressure. A series of triaxial compression tests were performed on cylindrical samples under different values of confining pressure $P_c = 0$, 2, 5, 10 and 20MPa. The size of cylindrical samples is 74mm in height and 37mm in diameter. For the sake of simplicity, numerical calculations are here performed under plane strain conditions on the vertical cross section of samples. The geometrical domain and boundary conditions are illustrated in Figure III .3(a). The mesh contains 5000 4-nodes elements and 5151 nodes.

The basic mechanical properties used in the calculations are as follows: Young's modulus E =4GPa, Poisson's ratio ν =0.2, C=10.8MPa, B=0.2×10^{-4}, $\alpha_0 = 0.25$. It is found that the value of α_m seems to be dependent on confining pressure. With giving an explicit relationship of this dependency, its value varies from 1.5 to 1 when the confining pressure changes from $P_c = 0$MPa to $P_c = 20$MPa.

The elastic stiffness degradation parameters β_1 and β_2 are equal to 1. β_3 is found dependent on confining pressure. Its values varies from 1 to 0.7 for the confining pressure is increased from $P_c = 0$MPa to $P_c = 20$MPa. The Taylor-Quinny coefficient for the plastic locked energy is taken as $\eta = 0.5$.

Concerning the crack fields evolutions, the toughness for tensile crack is taken as constant, $g_c^t = 8 \times 10^{-3}$kN/mm. However, the toughness for shear crack g_c^{sh} is found increasing with the confining pressure. Its values varies from 8×10^{-3}kN/mm to 14×10^{-3}kN/mm when the confining pressure changes from 0MPa to 20MPa. The length scale parameter is taken as $l_d = 0.37mm$ which is equal to the side length of the smallest element.
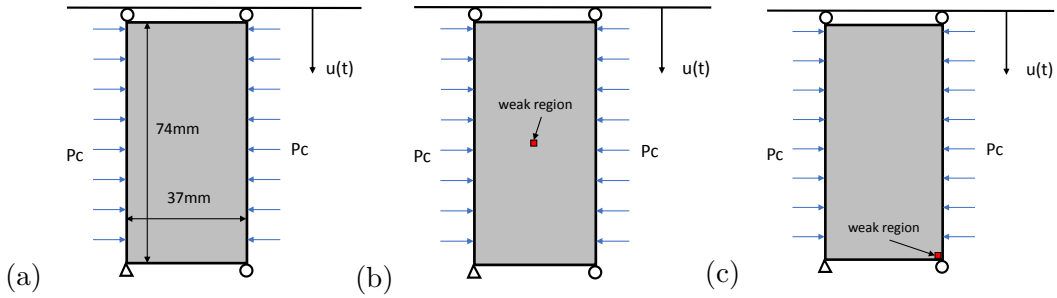
Figure III .3: (a)The dimension and the boundary conditions of triaxial compression test; (b)(c) 2 localizations of weak region

In order to facilitate the onset of macroscopic fracture, two cases of weak region is placed at the center of sample, as shown Figure III .3(b)(c). The size of weak region is equal to that of one element. In the weak region, the values of toughness parameters g_c^t and g_c^{sh} are reduced by 1%. In this first test, we use the case 1.

In Figure III .4, axial strains versus daviatoric stress curves are presented for four triaxial compression tests. The calculations are performed by using the displacement increment of $\Delta u = 1 \times 10^{-3}mm$ in each loading step and with the weak element at the center of domain. A very good agreement is obtained between the numerical results and experimental data of axial strains found in Armand et al. [2013], Hoxha and Auvray [2004]. Unfortunately, no lateral strains were recorded in those tests. For all tests, both the pre-

and post-peak responses are well reproduced. With the help of crack phase fields, the material softening in the post-peak regime is correctly described. Note that only a plastic hardening law is used in the plastic model. The material softening is entirely induced by the nucleation and propagation of cracks represented here by the two phase fields. Further, the transition from the brittle to ductile behavior with in increase of confining pressure is also well reproduced. The post-peak material softening is more abrupt when the confining pressure is lower. This means that the nucleation and propagation of cracks is attenuated by the increase of confining pressure. Finally, with the help of the specific degradation laws used for the elastic stiffness, the residual strength of material is also well described.
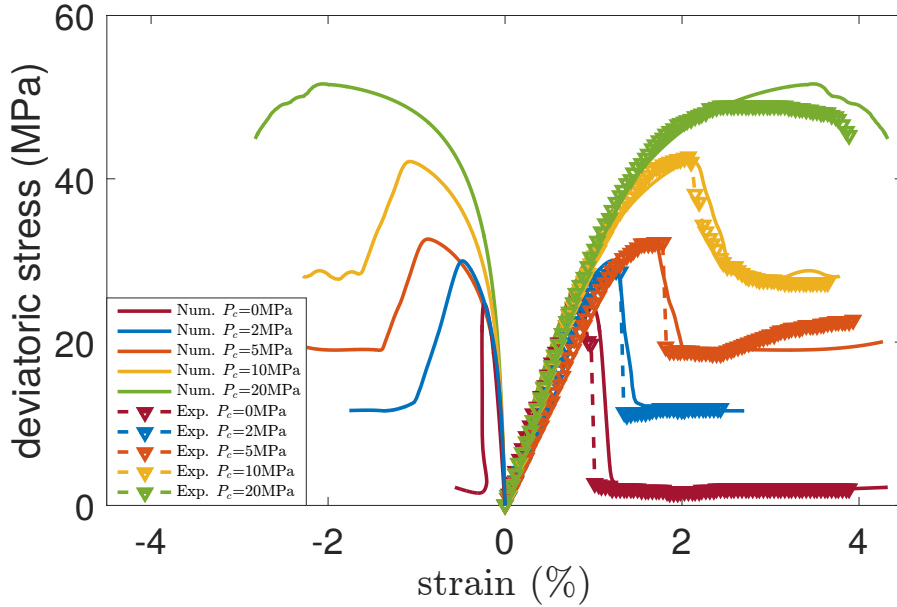
Figure III .4: Axial and lateral strains versus deviatoric stress of the COx claystone in triaxial compression tests with different confining pressures: comparisons between numerical results and the experimental data given in Armand et al. [2013], Hoxha and Auvray [2004].

4.2   Plastic deformation effect

In this section, the effect of plastic deformation on the mechanism of cracking and macroscopic response of material is investigated. For this purpose, the experimental data obtained from a second series of triaxial compression tests on the Cox claystone are used. In this second series, both axial and lateral strains were measured. However, the tests in this series were performed on a group of samples taken at a different depth than those in the first series [Armand et al., 2017]. As the mineralogical compositions vary with the depth,

the mechanical responses are also dependent on the depth. However, the influences of mineralogy on the mechanical behavior of the claystone are not investigated in detail here. These influences are taken into account only by considering another set of parameters, given as follows. The elastic parameters remain unchanged with respect to the first series of tests. The tensile toughness is taken constant as $g_c^t = 7.2 \times 10^{-3}$kN/mm. The shear toughness is affected by confining pressure and taken as $g_c^{sh} = 7.2 \times 10^{-3}$, 9.4×10^{-3} and 11×10^{-3}kN/mm respectively for $P_c =$2MPa, 6MPa and 12MPa. Regarding the degradation parameters, $\beta_1 = 1.0$ and $\beta_2 = 1.0$ are kept constant while $\beta_3 = 0.85$, $\beta_3 = 0.8$ and $\beta_3 = 0.7$, respectively for $P_c =$2MPa, 6MPa and 12MPa. The plastic parameters are given as: $C = 7.8$MPa, $B = 1.2 \times 10^{-4}$, $\alpha_0 = 0.25$, $\alpha_m = 1.2$, 1.2 and 1.0 respectively for $P_c =$2MPa, 6MPa and 12MPa. The Taylor-Quinny coefficient $\eta = 0.5$ is taken constant. The length scale parameter is $l_d = 0.37$mm.

The geometry and boundary conditions as well as the finite element mesh are the same as those in the previous calculations. In Figure III .5, one presents the stress-strain curves for three values of confining pressures, obtained by using the double phase-field model with plastic deformation. As for the first series of tests, one obtains again a good agreement between numerical results and experimental data for all the tests and for both the pre- and post-peak regimes. The consequence of cracking process on the macroscopic behavior is well captured.
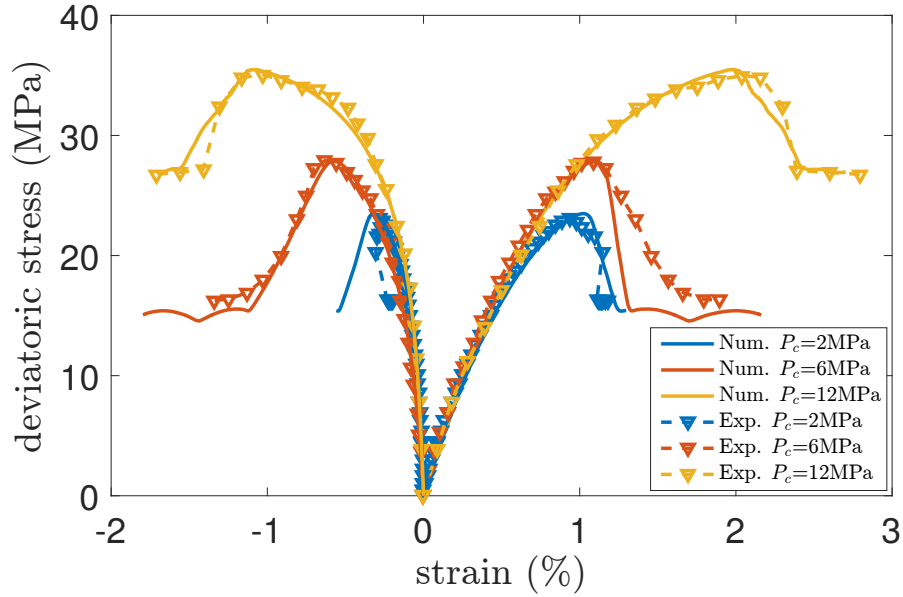
Figure III .5: Axial and lateral strains versus differential stress in triaxial compression tests with different confining pressures (2, 6, 12MPa): comparisons between numerical results (continuous line) with consideration of plastic deformation and the experimental data (dotted lines with triangles) reported in Armand et al. [2017]

For the purpose of comparison, the same tests are also simulated by using the double phase-field model without considering plastic deformation. The obtained results are presented in Figure III .6. It is clear that the inelastic deformation before the peak stress is significantly under-estimated if the plastic deformation is neglected. Further, the response in the post-peak regime is also a bit less well described.
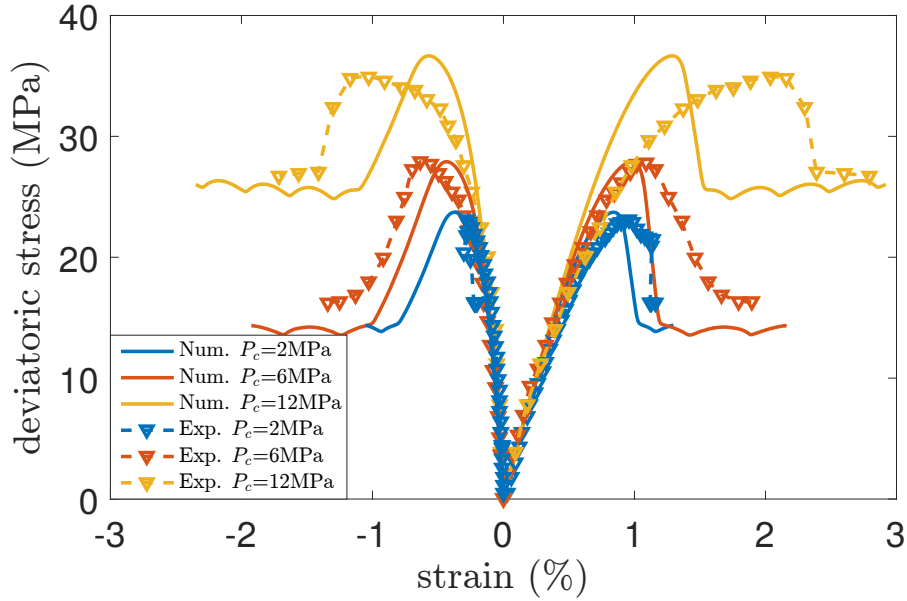
Figure III .6: Axial and lateral strains versus differential stress in triaxial compression tests with different confining pressures (2, 6, 12MPa): comparisons between numerical results (continuous line) without consideration of plastic deformation and the experimental data (dotted lines with triangles) reported in Armand et al. [2017].

The effect of plastic deformation on the cracking growth is also investigated. By using the weak element located at the center of sample as shown in Figure III .3(b), the distributions of tensile and shear crack fields obtained by the elastic crack model and the elastic-plastic crack model are respectively presented in Figure III .7 and Figure III .8, for four different levels of axial strain in the post-peak regime.

From these results, it is found that the cracking pattern is clearly affected by the plastic deformation. In the elastic-crack, no tensile cracks are observed. In the elastic-plastic crack model, both tensile and shear cracks are obtained. The tensile cracks are due to the dilatant plastic volumetric strain. The shear cracking remains the dominant mechanism due to the action of deviatoric stress in triaxial compression tests. Moreover, two shear bands are formed in the elastic crack calculations while one single shear band is created in the elastic-plastic crack calculations. The inclination angle of shear bands is also different between two models. It seems that the shear band obtained in the elastic-plastic calculations is in good agreement with the failure modes observed in triaxial compression tests [Armand et al., 2017].
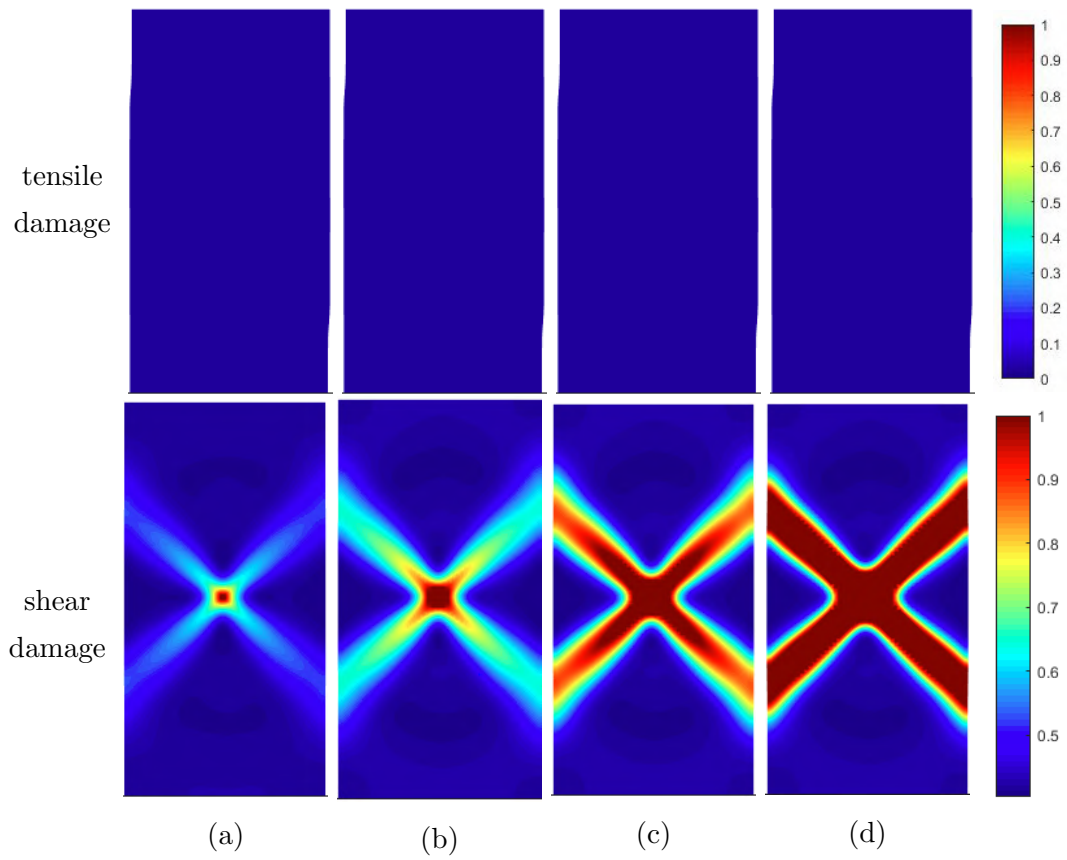
Figure III .7: Distributions of tensile/shear damage under Pc=12MPa. Results simulated by elastic damage model. During the post-peak at the load of axial strain: (a) $\epsilon_a = 1.35\%$, (b) $\epsilon_a = 1.4\%$, (c) $\epsilon_a = 1.5\%$, (d) $\epsilon_a = 1.55\%$.
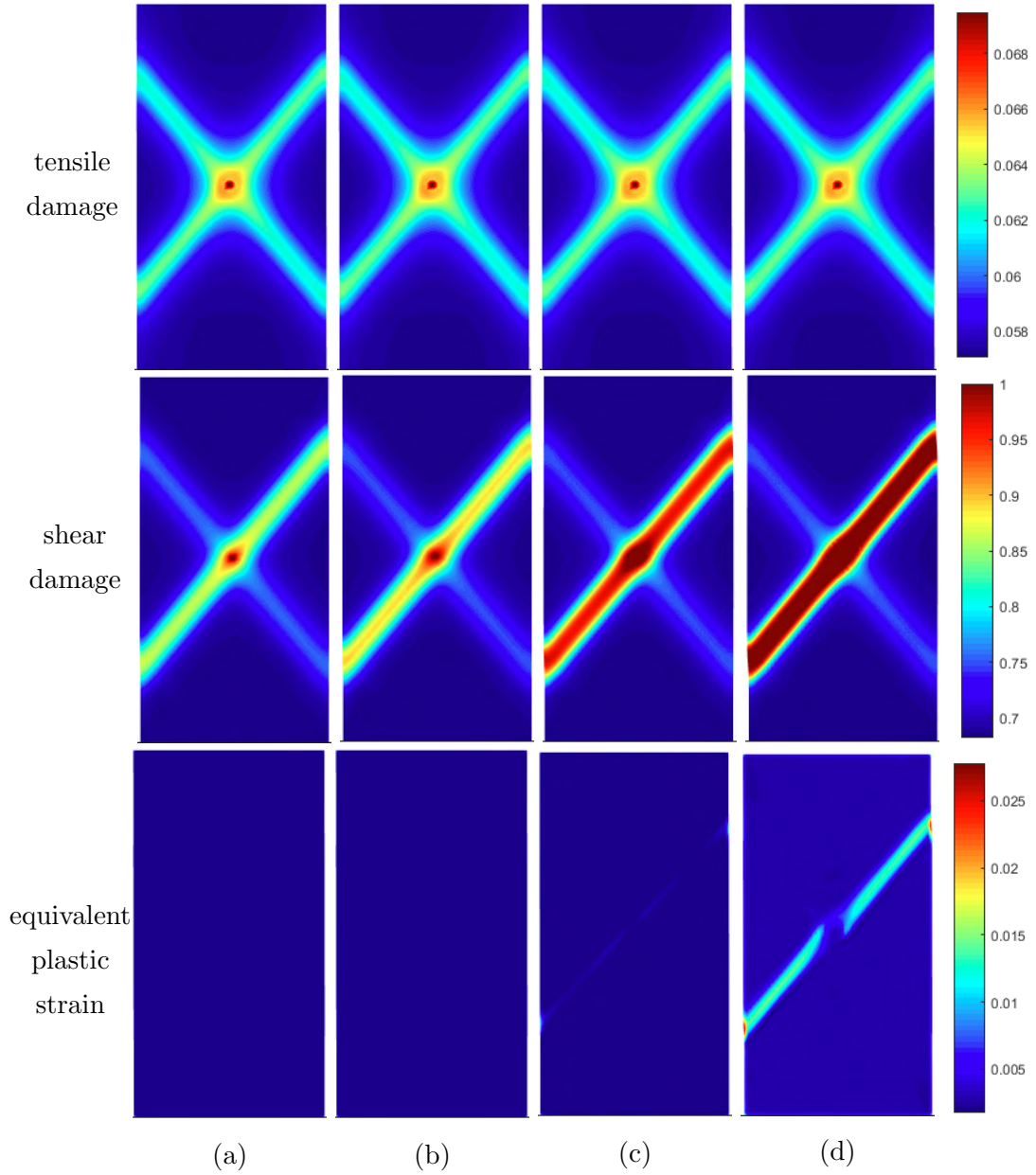
Figure III .8: Distributions of tensile/shear damage and equivalent plastic strain under Pc=12MPa. Results simulated by elasto-plastic damage model. During the post-peak at the load of axial strain: (a)$\epsilon_a = 2.1\%$; (b)$\epsilon_a = 2.15\%$; (c)$\epsilon_a = 2.2\%$; (d)$\epsilon_a = 2.25\%$.

Figures III .9-III .11 present results simulated by the case 2 of weak region: the weak region is located in the lower-right point of the sample as shown in Figure III .3(c). The Figure III .9 presents the results simulated by the elastic damage model. And the Figures III .10 and III .11 present the results simulated by the elasto-plastic damage model using different Taylor-Quinny coefficient η (defined in Eq. III .9).

In the results of elastic damage model(Figure III .9), there's only shear damaged zone which propagates from the weak region. And it reaches to the middle point of the left side of the sample.

And then, if we add the influence of plasticity, like in Figure III .10, $\eta = 0.5$, the half energy of plasticity is considered as the dissipated energy to transfer to the thermal energy, and the rest energy is considered as the stored energy, which become a part of the damage driving quantity. As the results presented, the shear damaged zone has the same form like in the Figure III .9. But the angle of the propagation is changed, the damaged zone reached to the point higher than the middle point of the left side of sample because of the contributions of plastic stored energy.

And if we reduce the value of η to 0.1, there's more plastic energy participates to create or propagate the damage. We can obtain the results presented as in the Figure III .11. The shear damaged zone appears almost from the lower-right point to the upper-left point of the sample. But it doesn't cross the weak region located.
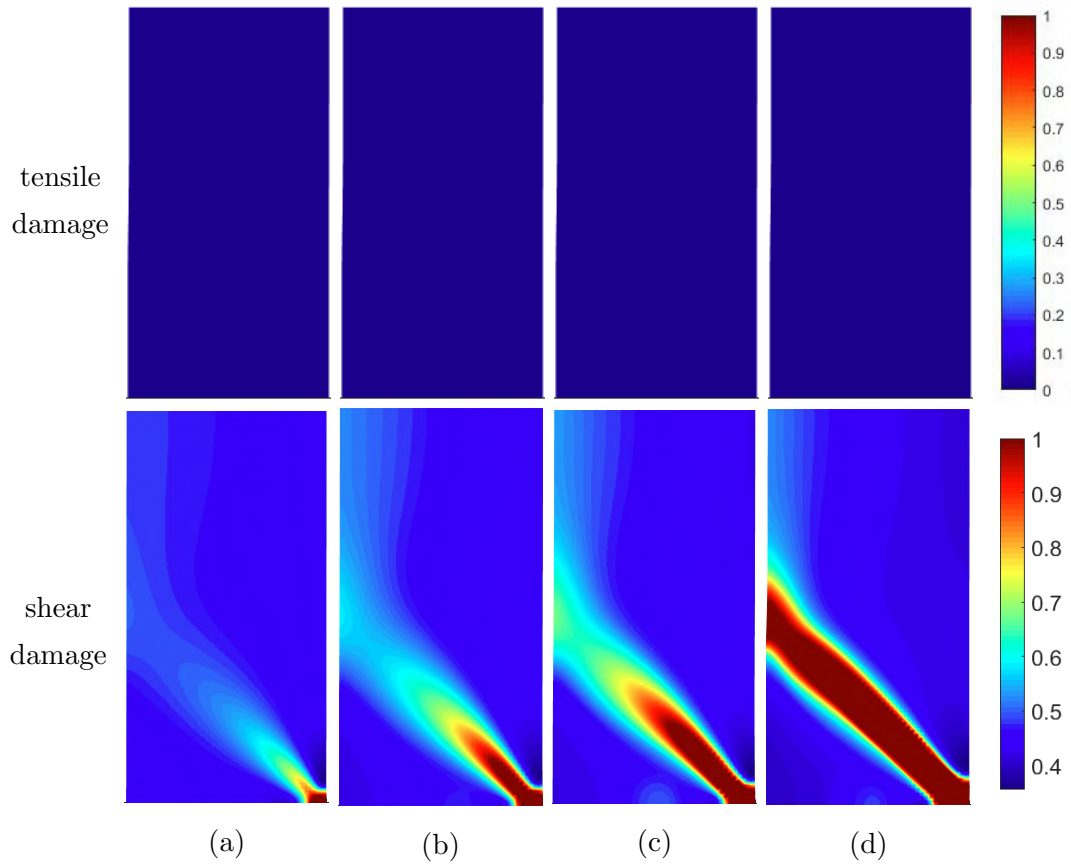
Figure III .9: Distributions of tensile/shear damage under Pc=12MPa. Results simulated by elastic damage model. During the post-peak at the load of axial strain: (a)$\epsilon_a = 1.35\%$; (b)$\epsilon_a = 1.4\%$; (c)$\epsilon_a = 1.45\%$; (d)$\epsilon_a = 1.55\%$.
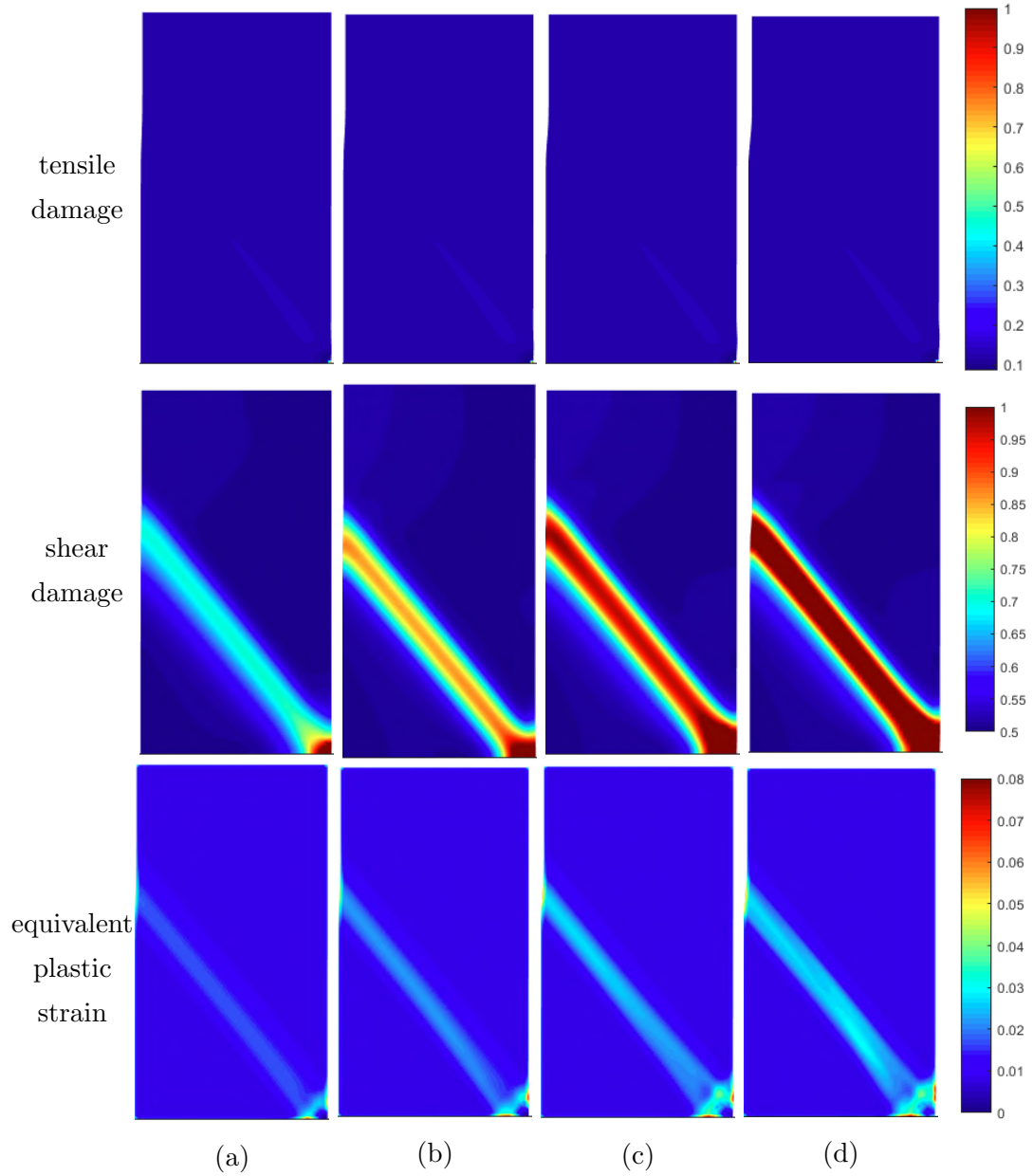
Figure III .10: Distributions of tensile/shear damage and equivalent plastic strain under Pc=12MPa. Results simulated by elasto-plastic damage model with $\eta = 0.5$. During the post-peak at the load of axial strain: (a)$\epsilon_a = 2.15\%$; (b)$\epsilon_a = 2.2\%$; (c)$\epsilon_a = 2.25\%$; (d)$\epsilon_a = 2.3\%$.
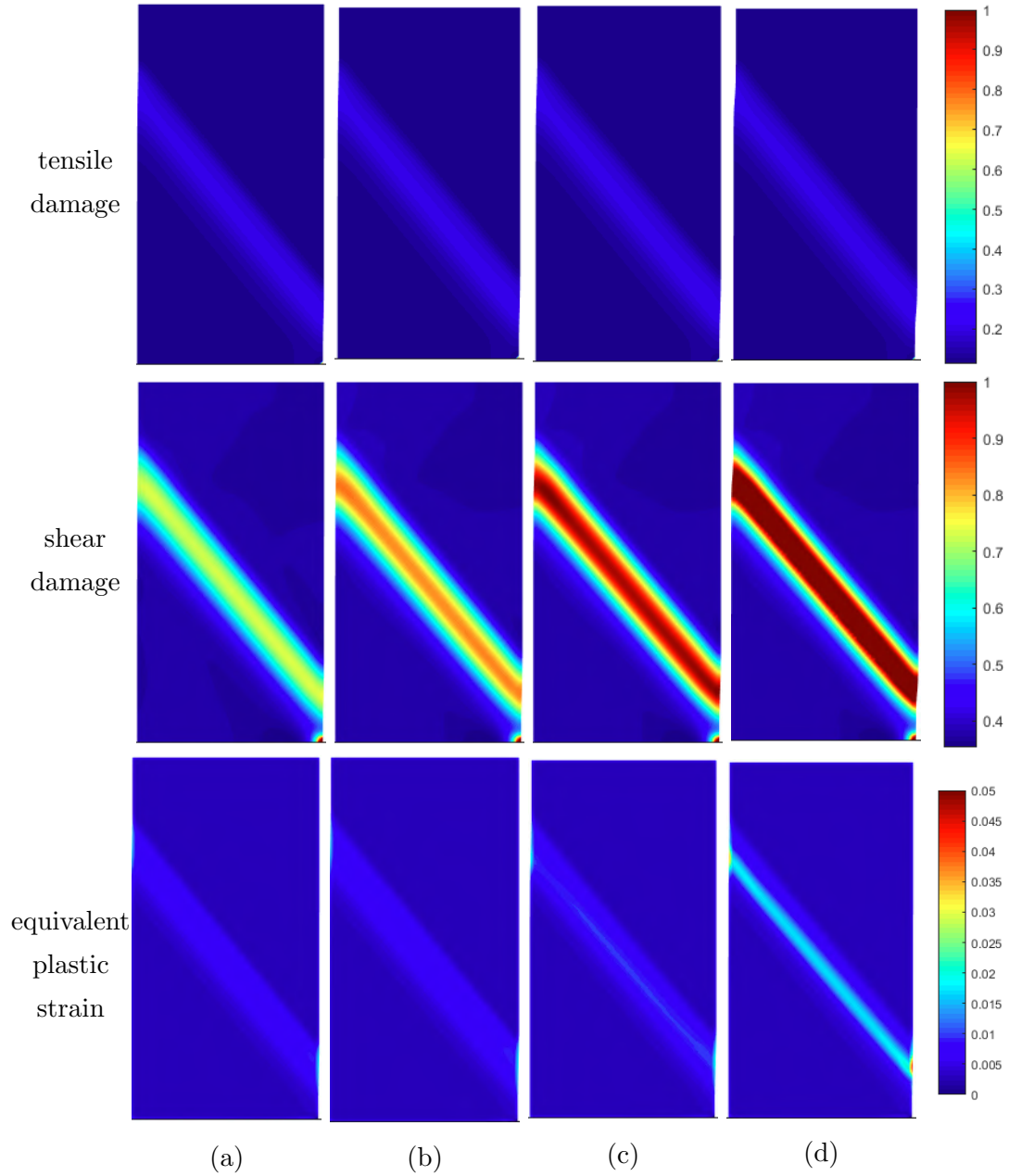
Figure III .11: Distributions of tensile/shear damage and equivalent plastic strain under Pc=12MPa. Results simulated by elasto-plastic damage model with $\eta = 0.1$. During the post-peak at the load of axial strain: (a)$\epsilon_a = 2.05\%$; (b)$\epsilon_a = 2.1\%$; (c)$\epsilon_a = 2.15\%$; (d)$\epsilon_a = 2.2\%$.

Both of the distributions of damaged zone simulated by elasto-plastic damage model are meaningful, they reproduce the features of crack path in the compression tests. The different location of weak region and different ratio of plastic energy dissipated are con-

sidered in the simulation to march the different possibility in the real experiment.

5   Conclusion

In this Chapter, the double crack phase-field method is developed to adapt to the elasto-plastic damage model. Both tensile and shear cracks as well as plastic deformation are taken into account. The evolutions of two crack fields are determined within the framework of irreversible thermodynamics and coupled with elastic and plastic strains. Plastic deformation plays an important role in clayey rocks by controlling the pre-peak deformation and affecting the shear band evolution in the post-peak regime. The double phase-field model brings a significant improvement of classical single phase-field models for predicting cracking process in rock-like materials. The adding plastic function improves the simulation results of ductile rock-like material very well in the triaxial compression tests.

Chapter IV

Coupling between THM and damage fields

Contents

1 Introduction

As part of the feasibility study for deep radioactive waste disposal, it is necessary to conduct coupled thermo-hydro-mechanical modeling. To carry out this type of modeling,

the thermo-poromechanical behavior of the rocks is one of the essential stages. In the previous chapter, we found that the mechanical behavior of the COx claystone can be described by an elasto-plastic model coupled to the damage by using proposed double phase-field method.

In this Chapter, we first propose to formulate the model of thermo-poroelastic behavior and to define the general equations that govern thermo-hydro-mechanical modeling. The first studies about the solid-fluid coupling in porous media were conducted by Terzaghi who introduced the effective stress concept in soil mechanics. Biot[Biot, 1941, 1956, 1973] generalized the Terzaghi's work for cohesive materials such as porous rock and defined a poroelasticity theory. And thanks to the general formulation of the thermo-hydro-mechanics of porous material proposed by Coussy. This model will be the basic model for our study. And then, the damage fields are considered as independent fields to participate the coupling of THM fields. After several verification examples which used to check our code of modeling, we shall use 3 examples to show the functions of our THM damage coupling at the last of this Chapter.

2 Theory of THM coupling

The porous medium is considered an open thermodynamic system that exchanges fluid mass and heat with the outside. We limit our discussion to cases of infinitesimal transformations. The state variables used are therefore the deformation tensor $\bar{\bar{\epsilon}}$, the fluid mass input per unit of initial volume of the porous medium m and the temperature T. Under the condition of the natural initial state(no initial stress), we have the quadratic form of free energy as:

$$\psi = g_m^0 m - s_0\theta + \frac{1}{2}\bar{\bar{\epsilon}} : \mathbb{C} : \bar{\bar{\epsilon}} - (\frac{m}{\rho_0^f})M\bar{\bar{B}} : \bar{\bar{\epsilon}} - \theta\bar{\bar{A}} : \bar{\bar{\epsilon}} - (s_m^0 - L^*)m\theta + \frac{1}{2}M(\frac{m}{\rho_0^f})^2 - \frac{1}{2}\frac{C_p}{T_0}\theta^2$$

$$(IV.1)$$

The parameter g_m^0 is the free enthalpy of the fluid per unit of mass, s_0 is the initial entropy of the system. θ is the temperature variation with respect to the reference state, defined by $\theta = T - T_0$. The 4th order symmetric tensor, $\mathbb{C}$, denotes the elastic tensor in undrained(m=0) and isotherm($\theta = 0$) condition. ρ_0^f is the initial density of the fluid. The scalar M is the Biot modulus and the 2ed order tensor, $\bar{\bar{B}}$, is the tensor of the Biot coefficients. L^* is the latent heat of fluid supply with constant deformation. C_p is the volumetric heat for constant deformation under undrained conditions.

With this global free energy equation at hand, the state equation can be deduced from

the potential as:

$$\bar{\bar{\sigma}} = \mathbb{C} : \bar{\bar{\epsilon}} - M\bar{\bar{B}}(\frac{m}{\rho_0^f}) - \bar{\bar{A}}\theta \tag{IV .2}$$

$$g_m = g_m^0 - (\frac{1}{\rho_0^f})M\bar{\bar{B}} : \bar{\bar{\epsilon}} - (s_m^0 - L^*)\theta + \frac{1}{\rho_0^f}M(\frac{m}{\rho_0^f}) \tag{IV .3}$$

$$s = s_0 + s_m^0 m + \bar{\bar{A}} : \bar{\bar{\epsilon}} - L^*m + \beta\theta \tag{IV .4}$$

using the linear fluid state equation:

$$g_m = g_m^0 + \frac{p - p_0}{\rho_0^f} - s_m^0(T - T_0) \tag{IV .5}$$

the Eq. (IV .3) can be expressed in terms of the pore pressure:

$$p = p_0 + M(-\bar{\bar{B}} : \bar{\bar{\epsilon}} + \frac{m}{\rho_0^f}) + \rho_0^f L^*\theta \tag{IV .6}$$

and then, we rewrite Eq. (IV .2) and Eq. (IV .4) with the help of Eq. (IV .6) to obtain the state equations in the drained condition:

$$\bar{\bar{\sigma}} = \mathbb{C}^b : \bar{\bar{\epsilon}} - \bar{\bar{B}}(p - p_0) - \bar{\bar{A}}^b\theta \tag{IV .7}$$

$$s = s_0 + s_m^0 m + \bar{\bar{A}}^b : \bar{\bar{\epsilon}} + \frac{C_p^b}{T_0}\theta \tag{IV .8}$$

with:

$$\mathbb{C}^b = \mathbb{C} - M(\bar{\bar{B}} \otimes \bar{\bar{B}}) \tag{IV .9}$$

$$\bar{\bar{A}}^b = \bar{\bar{A}} - 3\alpha_m M\bar{\bar{B}} \tag{IV .10}$$

$$3\alpha_m = \rho_0^f L^*/M \tag{IV .11}$$

$$C_p^b = C_p - 9T_0\alpha_m^2 M \tag{IV .12}$$

the use of $*^b$ presents the parameter in the drained condition, and α_m is the coefficients of differential thermal expansion between drained and undrained condition.

Now we can write the tensor of the effective stresses of Biot for the elastic deformations $\bar{\bar{\sigma}}^{ef}$:

$$\bar{\bar{\sigma}}^{ef} = \mathbb{C}^b : \bar{\bar{\epsilon}} - \bar{\bar{A}}^b\theta \tag{IV .13}$$

and

$$\bar{\bar{\sigma}}^{ef} = \bar{\bar{\sigma}} + \bar{\bar{B}}(p - p_0) \tag{IV .14}$$

here, if $\bar{\bar{B}} = \bar{\bar{1}}$, then $\bar{\bar{\sigma}}^{ef} = \bar{\bar{\sigma}} + \bar{\bar{1}}(p - p_0)$, which we can find the Terzaghi concept in soil mechanics.

In the case of isotropic porous material, we have:

$$\mathbb{C} = (K - \frac{2}{3}\mu)\mathbb{J} + 2\mu\mathbb{I}, \ \bar{\bar{B}} = b\bar{\bar{1}}, \ \bar{\bar{A}} = a\bar{\bar{1}} \tag{IV .15}$$

With the isotropic parameters at hand, we can rewrite Eq. (IV .7), (IV .6) and (IV .8) as:

$$\bar{\bar{\sigma}} - \bar{\bar{\sigma}}^0 = 2\mu\bar{\bar{\epsilon}} + (K - \frac{2}{3}\mu)tr(\epsilon)\bar{\bar{1}} - Mb(\frac{m}{\rho_0^f})\bar{\bar{1}} - a\theta\bar{\bar{1}} \tag{IV .16}$$

$$p - p_0 = M(-b : \bar{\bar{\epsilon}} + \frac{m}{\rho_0^f}) + 3\alpha_m\theta \tag{IV .17}$$

$$s - s_0 = atr(\bar{\bar{\epsilon}}) + (s_m^0 - L^*)m + \frac{C_p^b}{T_0}\theta \tag{IV .18}$$

At last, we rewrite the Eq. (IV .16) and (IV .18) with the help of Eq. (IV .6), we have:

$$\bar{\bar{\sigma}} - \bar{\bar{\sigma}}^0 = 2\mu^b\bar{\bar{\epsilon}} + (K^b - \frac{2}{3}\mu^b)tr(\epsilon)\bar{\bar{1}} - b(p - p_0)\bar{\bar{1}} - a^b\theta\bar{\bar{1}} \tag{IV .19}$$

$$s - s_0 = a^btr(\bar{\bar{\epsilon}}) + s_m^0 m - 3\alpha_m(p - p_0) + \frac{C_p^b}{T_0}\theta \tag{IV .20}$$

with the relations form between drained and undrained parameters:

$$\begin{cases} K^b = K - b^2M; \\ \mu^b = \mu; \\ a^b = a - 3\alpha_mMb; \\ a^b = 3K^b\alpha^b; \\ a = 3K\alpha; \\ C_p^b = C_p + 9T_0\alpha_m^2M. \end{cases} \tag{IV .21}$$

In these group of form of isotropic porous material, K and μ present the bulk modulus and shear modulus. b presents the Biot coefficient.

Now we have seven independent parameters. Two elastic parameters of the porous medium under drained and isothermal conditions: K^b and μ^b; Five THM coupling parameters: b, M, α_b, α_m and C_p^b. The elastic parameters can be obtained by the classic method based on the elastic theory. And the THM coupling parameters can be determined by the specific tests(Shao and Giraud 2002).

In addition, micromechanical analyzes make it possible to determine the relationships between the coupling parameters and the properties of the constituents of the porous material(Auriault and Sanchez-Palencia, 1977 ; Cheng 1997 ; Lydzba and Shao 1999). For the isotropic porous material, we have the relations between the THM coupling parameters

as:

$$\begin{cases} b = 1 - \frac{K_b}{K_s}; \\ \frac{1}{M} = \frac{b-\phi}{K_s} + \frac{\phi}{K_f}; \\ \alpha_m = (b-1)\alpha_b + (1-\phi)\alpha_s + \phi\alpha_f; \\ C_p^b = (1-\phi)C_p^s + \rho_f^0 \phi C_p. \end{cases} \qquad \text{(IV .22)}$$

K_s is the bulk modulus of the solid matrix and K_f is for saturating fluid. ϕ presents the connected porosity. α_s and α_f are the dilation coefficients relating to the solid matrix and the fluid. C_p is the the specific heat of the fluid at constant pressure. C_p^b is the density heat drained with constant stresses and is deduced from the volume heat drained at constant strain.

3 Numerical implementation in finite element method

Here, we can obtain the equilibrium equations for the quasi static problem of a porous medium:

$$div(\bar{\bar{\sigma}}) + F_v = 0 \qquad \text{(IV .23)}$$

For the fluid diffusivity equation, il should use the Darcy law and law of conservation of mass:

$$\begin{cases} \frac{\bar{\omega}}{\rho^f} = k(-\nabla p + \rho^f \bar{g}) \\ \dot{m} = -div\bar{M} \end{cases} \qquad \text{(IV .24)}$$

in infinitesimal transformation, we have $\bar{\omega} \simeq \bar{M}$, then:

$$\dot{m} = div[\rho_0^f k(-\nabla p + \rho^f \bar{g})] \qquad \text{(IV .25)}$$

in our study, we can ignore the mass of fluid, the we have:

$$\frac{\dot{m}}{\rho_0^f} = kdiv(\nabla(p - p_0)) \qquad \text{(IV .26)}$$

with the help of IV .17, we can obtain fluid diffusivity equation as:

$$kdiv(\nabla p) = \frac{1}{M}\frac{\partial p}{\partial t} + b\frac{\partial \epsilon_{kk}}{\partial t} - 3\alpha_m\frac{\partial \theta}{\partial t} \qquad \text{(IV .27)}$$

For the heat diffusivity equation, it should use the Fourier law and Laws of thermodynamics, we can obtain:

$$Tdiv(\bar{M}s_m) + \dot{s}_b T - k\nabla p \boldsymbol{.} \nabla p = \lambda div(\nabla \theta) \qquad \text{(IV .28)}$$

with the help of IV .18, we can obtain heat diffusivity equation as:

$$\lambda div(\nabla\theta) = C_p^b \frac{\partial\theta}{\partial t} - 3\alpha_m T_0 \frac{\partial p}{\partial t} + 3\alpha_b K_b T_0 \frac{\partial\epsilon_{kk}}{\partial t} - k\nabla p(C_p\nabla\theta) \qquad \text{(IV .29)}$$

Following the Galerkin method, the weak form of displacement, pore pressure and temperature can be written as:

$$\int_\Omega \delta\bar{\bar{\epsilon}} : \mathbb{C}^b : \bar{\bar{\epsilon}}dV - \int_\Omega \delta\bar{\bar{\epsilon}} : (\delta p)\bar{\bar{I}}dV - \int_\Omega \delta\bar{\bar{\epsilon}} : (3\alpha_b K_b T)\bar{\bar{I}}dV = \int_{S_{\bar{t}}} \bar{t}\delta\bar{u}dS \qquad \text{(IV .30)}$$

$$\int_\Omega k\nabla p\nabla(\delta p)dV = \int_{S_\omega} k\delta p\nabla p\bar{n}dS - \int_\Omega \frac{1}{M}\frac{\partial p}{\partial t}\delta pdV - \int_\Omega b\frac{\partial\epsilon_{kk}}{\partial t}\delta pdV + \int_\Omega 3\alpha_m\frac{\partial\theta}{\partial t}\delta pdV \qquad \text{(IV .31)}$$

$$\int_\Omega \lambda\nabla T\nabla(\delta\theta)dV = \int_{S_q} \lambda\delta T\nabla T\bar{n}dS - \int_\Omega C_p^b\frac{\partial\theta}{\partial t}\delta\theta dV - \int_\Omega (3\alpha_b K_b T_0)\frac{\partial\epsilon_{kk}}{\partial t}\delta\theta dV$$
$$+ \int_\Omega (3\alpha_m T_0)\frac{\partial p}{\partial t}\delta\theta dV + \int_{S_\Omega} k\nabla p(C_p\nabla\theta)\delta\theta dV \qquad \text{(IV .32)}$$

And then, with the help of the shape functions N_u and N_p and the matrix of shape functions derivatives B_u and B_p, the nodal values of the displacement $\bar{U}$, the pore pressure $\bar{P}$, temperature $^-$ and their gradient values can be approximated in one element by:

$$\bar{u} = N_u\bar{U}, \ p = N_p\bar{P}, \ \theta = N_p\bar{T} \qquad \text{(IV .33)}$$

$$\bar{\bar{\epsilon}} = B_u\bar{U}, \ \nabla p = B_p\bar{P}, \ \nabla\theta = B_p\bar{T} \qquad \text{(IV .34)}$$

and we have the same approximation for the nodal incremental functions of them by:

$$\Delta\bar{u} = N_u\Delta\bar{U}, \ \Delta p = N_p\Delta\bar{P}, \ \Delta\theta = N_p\Delta\bar{T} \qquad \text{(IV .35)}$$

$$\Delta\bar{\bar{\epsilon}} = B_u\Delta\bar{U}, \ \nabla(\Delta p) = B_p(\Delta\bar{P}), \ \nabla(\Delta\theta) = B_p(\Delta\bar{T}) \qquad \text{(IV .36)}$$

and for the nodal trial functions by:

$$\delta\bar{u} = N_u\delta\bar{U}, \ \delta p = N_p\delta\bar{P}, \ \delta\theta = N_p\delta\bar{T} \qquad \text{(IV .37)}$$

$$\delta\bar{\bar{\epsilon}} = B_u\delta\bar{U}, \ \nabla(\delta p) = B_p(\delta\bar{P}), \ \nabla(\delta\theta) = B_p(\delta\bar{T}) \qquad \text{(IV .38)}$$

At last, with the help of the approximation functions, we obtain the discrete system by [Shao et al., 1993]:

$$\begin{cases} R_{uu}\bar{U} + C_{up}\bar{P} + C_{uT}\bar{T} = \bar{F}_e \\ R_{pp}\bar{P} + M_{pp}\frac{\partial\bar{P}}{\partial t} + C_{pu}\frac{\partial\bar{U}}{\partial t} + C_{pT}\frac{\partial\bar{T}}{\partial t} = \bar{F}_\omega \\ R_{TT}\bar{T} + M_{TT}\frac{\partial\bar{T}}{\partial t} + C_{Tu}\frac{\partial\bar{U}}{\partial t} + C_{Tp}\frac{\partial\bar{P}}{\partial t} = \bar{F}_q \end{cases} \qquad \text{(IV .39)}$$

with the definitions of the matrix by:

$$\begin{cases} R_{uu} = -\int_\Omega^t B_u(\mathbb{C}_b)B_u dV \\ C_{up} = \int_\Omega^t B_u(b)N_p dV \\ C_{uT} = \int_\Omega^t B_u(3\alpha_b K_b)N_p dV \\ \Delta \bar{F}_e = -\int_{s_{\bar{t}}}^t N_u \bar{t} dS \end{cases} \qquad (\text{IV .40})$$

$$\begin{cases} R_{pp} = -\int_\Omega^t B_p(k)B_p dV \\ M_{pp} = \int_\Omega^t N_p(\frac{1}{M})N_p dV \\ C_{pu} =^t C_{up} \\ C_{pT} = \int_\Omega^t N_p(-3\alpha_m)N_p dV \\ \Delta \bar{F}_\omega = -\int_{s_\omega}^t N_p dS \end{cases} \qquad (\text{IV .41})$$

$$\begin{cases} R_{TT} = -\int_\Omega^t B_p(\frac{\lambda}{T_0})B_p dV \\ C_{Tu} =^t C_{uT} \\ M_{TT} = \int_\Omega^t N_p(\frac{C_p}{T_0})N_p dV \\ C_{Tp} =^t C_{pT} \\ \Delta \bar{F}_q = -\int_{s_q}^t N_p dS \end{cases} \qquad (\text{IV .42})$$

In this study, in order to easily handle the non-linearities of the problem, we use the incremental method to solve the problem.

At first, the temporal discretization of the main unknowns x which presents $\bar{U}$, $\bar{P}$ and $\bar{T}$ can be written as the Euler method form:

$$x(t + \S\Delta t) = (1 - \S)x(t) + \S x(t + \Delta t), \ \S \in [0, 1] \qquad (\text{IV .43})$$

$$\frac{d}{dt}x(t + \partial\Delta t) = \frac{x(t + \Delta t) - x(t)}{\Delta t} = \frac{\Delta x}{\Delta t} \qquad (\text{IV .44})$$

And then, we can rewrite the Eq. IV .23, IV .27 and IV .29 as:

$$\begin{cases} div(\Delta \bar{\bar{\sigma}}) + \Delta F_v = 0 \\ kdiv(\nabla p_\S) = \frac{1}{M}\frac{\Delta p}{\Delta t} + b\frac{\Delta \epsilon_{kk}}{\Delta t} - 3\alpha_m \frac{\Delta \theta}{\Delta t} \\ \lambda div(\nabla \theta_\S) = C_p^b \frac{\Delta \theta}{\Delta t} - 3\alpha_m T_0 \frac{\Delta p}{\Delta t} + 3\alpha_b K_b T_0 \frac{\Delta \epsilon_{kk}}{\Delta t} - k\nabla p_\S(C_p \nabla \theta_\S) \end{cases} \qquad (\text{IV .45})$$

with the respect of:

$$\begin{cases} p_\S = p_n + \S\Delta p, \ p_n = p(t_n) \\ \theta_\S = \theta_n + \S\Delta \theta, \ \theta_n = \theta(t_n) \end{cases} \qquad (\text{IV .46})$$

After discretization in space and time, the linear system of THM coupling can be written as:

$$
\begin{cases}
R_{uu}\Delta\bar{U}_{n+1} + C_{up}\Delta\bar{P}_{n+1} + C_{uT}\Delta\bar{T}_{n+1} = \Delta\bar{F}_e^{n+1} \\
(\Delta t_{n+1}R_{pp} + M_{pp})\Delta\bar{P}_{n+1} + C_{pu}\Delta\bar{U}_{n+1} + C_{pT}\Delta\bar{T}_{n+1} = \Delta t_{n+1}(-R_{pp}\bar{P}_n + \Delta\bar{F}_\omega^{n+1}) \\
(\Delta t_{n+1}R_{TT} + M_{TT})\Delta\bar{T}_{n+1} + C_{Tu}\Delta\bar{U}_{n+1} + C_{Tp}\Delta\bar{P}_{n+1} = \Delta t_{n+1}(-R_{TT}\bar{T}_n + \Delta\bar{F}_q^{n+1})
\end{cases}
\tag{IV .47}
$$

by using explicit method $\S = 1$, the relation between time step n and n+1 used is:

$$
\begin{cases}
\bar{U}_{n+1} = \bar{U}_n + \Delta\bar{U}_{n+1} \\
\bar{P}_{n+1} = \bar{P}_n + \Delta\bar{P}_{n+1} \\
\bar{T}_{n+1} = \bar{T}_n + \Delta\bar{T}_{n+1}
\end{cases}
\tag{IV .48}
$$

4   The coupling of THM-d

In order to consider the impact of damage for THM coupling, we introduce the double phase-field method. As we can see in the previous chapter, the phase-field method has an independent field to describe the variation of the damage. The damage is considered as an independent field to be coupled with mechanical field. Based on this feature, the new coupling is considered as the coupling between five fields: the temperature field, the pore pressure field, the mechanical field , the tensile and shear damage fields. These 5 fields can be solved by the partial differential equations themselves. And the couplings of these 5 fields are shown clearly in the Figure IV .1.

At first, we have seen the detail of the coupling between THM fields in the previous section: the variation of temperature leads to the variation of the pore pressure with respect to the differential expansion between rock and fluid: α_m. The pore pressure field and the mechanical field are coupled by the Biot coefficient: b. Finally, the relationship between the temperature field and the mechanical field is defined by the bulk modulus K^b and thermal expansion of the rock α_m.

And then, the damage fields are coupled with the mechanical field: damage fields depend on the defined strain energy from the mechanical field, and the mechanical field is influenced by the stiffness matrix which depends on the damage values d^α. We have seen the detail of this coupling in the chapter I and II.
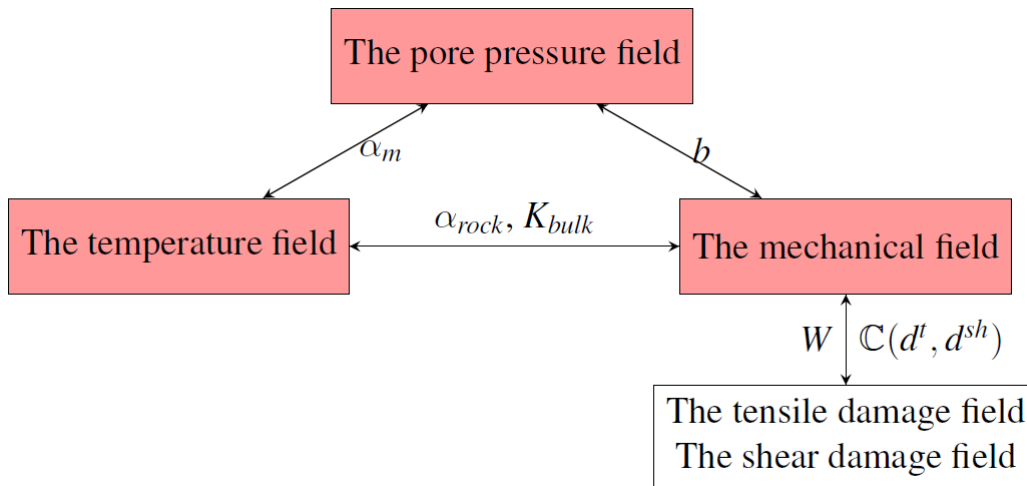
Figure IV .1: The coupling between THM and damage fields

In this study, we focus on the rock-like material. Thanks to the large of experiment and simulation results, We can see that the effect of pore pressure changes on temperature is very small, and the effect of stress changes on temperature is also small. In order to optimize the calculation, we have the simplified model of coupling as shown in Figure IV .2.
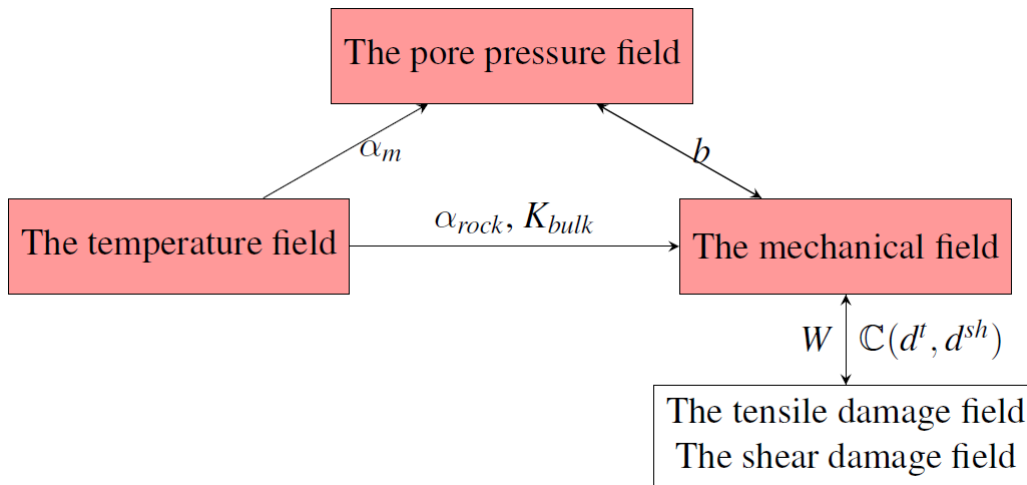
Figure IV .2: The coupling between THM and damage fields

The fields of damage also influence the THM fields and their couplings. The main parameters influenced are shown here:

- In the pore pressure field:

    - The permeability:

$$k = k_{initial} \exp(\gamma d^t) \tag{IV .49}$$

- For the thermo-mechanical coupling:

    - The bulk modulus:

$$K(d^t) = K_{initial}(1 - d^t) \tag{IV .50}$$

- For the hydro-mechanical coupling:

    - The coefficient pf Biot:

$$b(d^t) = b_{initial} + (1 - b_{initial})d^t \tag{IV .51}$$

    - The porosity:

$$\Phi(d^t) = \Phi_{initial} + (1 - \Phi_{initial})d^t \tag{IV .52}$$

    - The Biot module:

$$\frac{1}{M(d^t)} = \frac{(1 - b(d^t))(b(d^t) - \Phi(d^t))}{K_s} + \frac{\Phi(d^t)}{K_f} \tag{IV .53}$$

- For the thermo-hydraulic coupling:

    - Differential expansion:

$$\alpha_m(d^t) = (b(d^t) - \Phi(d^t))\alpha_s + \Phi_{ini}\alpha_f \tag{IV .54}$$

5   Iteratively coupled technique

As mentioned in previous section, for simplify the structure and the calculation of the coupling for adapting the rock-like material, we can at first calculate the temperature field for a new time step $n + 1$. The results of temperature $\Delta \bar{T}_{n+1}$ can be considered as a thermal load to participate the rest of coupling.

Now we focus on the HM coupling,Settari and Walters [1999] discuss the different coupling methods and categorized them as decoupled, explicitly coupled, iteratively coupled and

fully coupled. In our study, we choose the iteratively coupled method. Compare with other methods, first, it has stability and accuracy. It can produce the same results as a fully coupled technique if a sufficiently tight nonlinear convergence criteria is enforced. Secondly, it has modularity feature. It allows the coupled equations to be processed by separate program modules, taking full advantage of specialized features and disciplinary expertise built into independently developed single field models. In an iteratively coupled scheme, solutions for multiphase flow and poroelasticity equations are coupled through the nonlinear iterations in one time step.

Newton's method is used here to linearize the discrete system(IV .47) of HM fields. Residuals at the kth nonlinear iteration are computed as:

$$
\begin{cases}
R_u^{n+1,k} = & \Delta \bar{F}_e^{n+1} - R_{uu}\Delta \bar{U}^{n+1,k} - C_{up}\Delta \bar{P}^{n+1,k} - C_{uT}\Delta \bar{T}^{n+1} \\
R_p^{n+1,k} = & \Delta t_{n+1}(-R_{pp}\bar{P}^n + \Delta \bar{F}_\omega^{n+1}) - (\Delta t_{n+1}R_{pp} + M_{pp})\Delta \bar{P}^{n+1,k} \\
& - C_{pu}\Delta \bar{U}^{n+1,k} - C_{pT}\Delta \bar{T}^{n+1}
\end{cases}
\tag{IV .55}
$$

Applying Newton's linearization to the above residual equations yields the following algebraic system:

$$
\begin{bmatrix}
-\frac{\partial R_u}{\partial \Delta U} & -\frac{\partial R_u}{\partial \Delta P} \\
-\frac{\partial R_p}{\partial \Delta U} & -\frac{\partial R_p}{\partial \Delta P}
\end{bmatrix}
\begin{bmatrix}
\delta(\Delta \bar{U}) \\
\delta(\Delta \bar{P})
\end{bmatrix}^{n+1,k+1}
=
\begin{bmatrix}
R_u \\
R_p
\end{bmatrix}^{n+1,k}
\tag{IV .56}
$$

then, with the help of IV .55, the linearized system can be developed as:

$$
\begin{bmatrix}
R_{uu} & C_{up} \\
C_{pu} & \Delta t_{n+1}R_{pp} + M_{pp}
\end{bmatrix}
\begin{bmatrix}
\delta(\Delta \bar{U}) \\
\delta(\Delta \bar{P})
\end{bmatrix}^{n+1,k+1}
=
\begin{bmatrix}
R_u \\
R_p
\end{bmatrix}^{n+1,k}
\tag{IV .57}
$$

the two field equations in Eq. IV .57 are solved sequentially at each Newton iteration by

$$
(\Delta t_{n+1}R_{pp} + M_{pp})\delta(\Delta \bar{P})^{n+1,k+1} = R_p^{n+1,k} + C_{pu}\delta(\Delta \bar{U})^{n+1,k}
\tag{IV .58}
$$

and

$$
R_{uu}\delta(\Delta \bar{U})^{n+1,k+1} = R_u^{n+1,k} - C_{up}\delta(\Delta \bar{P})^{n+1,k+1}
\tag{IV .59}
$$

The iterations are performed as Eq. IV .57 shown, until a given tolerance for the residuals is satisfied. At the end of the each iteration, the result values are updated by:

$$
\begin{cases}
\Delta \bar{U}^{n+1,k+1} = \Delta \bar{U}^{n+1,k} + \delta(\Delta \bar{U})^{n+1,k+1} \\
\Delta \bar{P}^{n+1,k+1} = \Delta \bar{P}^{n+1,k} + \delta(\Delta \bar{P})^{n+1,k+1}
\end{cases}
\tag{IV .60}
$$

The iterative coupling presented can be described as a simple algorithm:

Algorithm 2: Simplified algorithm for time step $n + 1$

Input: $\bar{T}_n$, $\bar{P}_n$ and $\bar{U}_n$.

Output: $\bar{T}_{n+1}$, $\bar{P}_{n+1}$ and $\bar{U}_{n+1}$.

Start a new time step n+1;

Initialize $\Delta\bar{T}_{n+1} = 0$, $\Delta\bar{P}_{n+1} = 0$ and $\Delta\bar{U}_{n+1} = 0$;

Use Eq. IV .47 to calculate ΔT_{n+1}, ΔP_{n+1} and ΔU_{n+1};

for $s = 1...k$(iteration step) **do**

    Start a new nonlinear iteration k+1;

    Initialize $\Delta\bar{P}_{n+1}^k = \Delta\bar{P}_{n+1}$, $\Delta\bar{U}_{n+1}^k = \Delta\bar{U}_{n+1}$;

    Use Eq. IV .55 to compute residuals $R_u^{n+1,k}$ and $R_p^{n+1,k}$;

    Check for convergence by $R_u^{n+1,k} \leq Tol_u$ and $R_p^{n+1,k} \leq Tol_p$. If both tolerances are satisfied, terminate the current time step and go to the beginning of this algorithm for a new time level. Otherwise, continue with the following steps;

    Solve for $\partial(\Delta\bar{U})^{n+1,k+1}$ and $\partial(\Delta\bar{P})^{n+1,k+1}$ by using Eq. IV .58 and Eq. IV .59;

    Update $\Delta\bar{U}^{n+1,k+1}$ and $\Delta\bar{P}^{n+1,k+1}$ by using Eq. IV .60;

end for

Update $\bar{T}_{n+1}$, $\bar{P}_{n+1}$ and $\bar{U}_{n+1}$ by using Eq. IV .48.

---

6   Verification examples for code

In this section, we propose some examples to check the function of coupling THM by our Matlab code.

The result of the temperature field is first compared between the results simulated by Abaqus and Matlab. Then, we propose three small examples to compare the THM coupling results obtained by Matlab and the theory.

6.1   Verification for temperature field

The temperature is an independent field in our model of coupling. It is not influenced by the pore pressure and mechanical field. So it is the most simple field to simulate and verify.

We choose a structure as in Figure IV .3(a). We have an increased temperature ($\Delta T = 60^o C$) on the wall (Figure IV .3(b)). It presents a heating process in the underground tunnel.
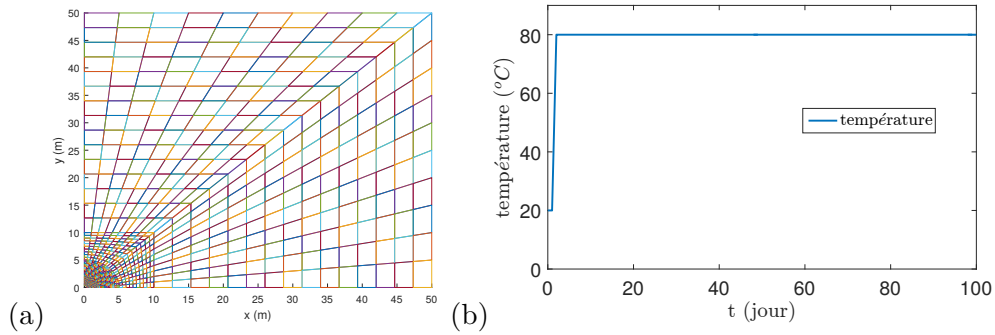
Figure IV .3: (a) Mesh of a 1/4 plate with a hole (b) Temperature at the wall according to the time.

The thermal parameters used in this test are cited here:

- Initial temperature : $T_{initial} = 20^o C$

- Heating temperature at the wall : $T_{wall} = 80^o C$

- Thermal conductivity : $\lambda = 1,65 W.m^{-1}.K^{-1}$

- Specific heat capacity : $C_p = 1000 J.kg^{-1}.K^{-1}$

The results of simulation by Abaqus and Matlab are shown in the Figure IV .4 and IV .5. As we can see that he results are exactly the same.
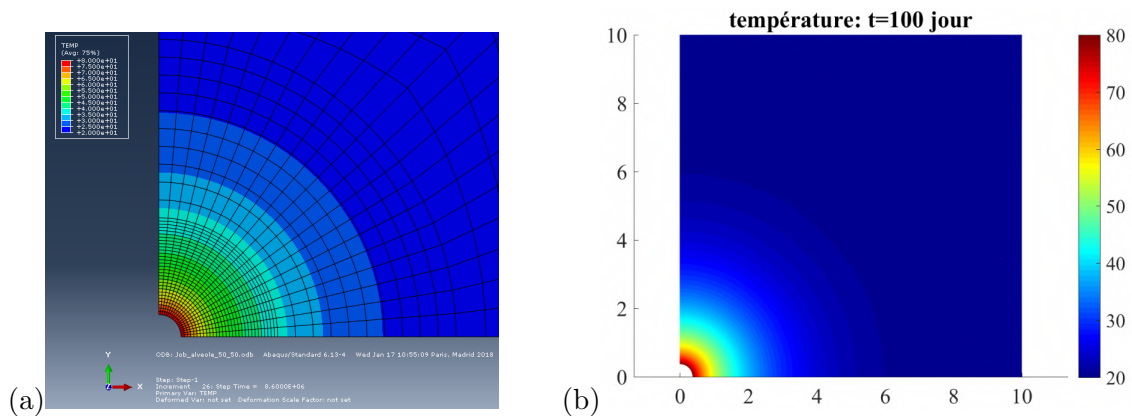
Figure IV .4: Distribution of the temperature at t=100 days, results simulated by (a)Abaqus; (b)Matlab.
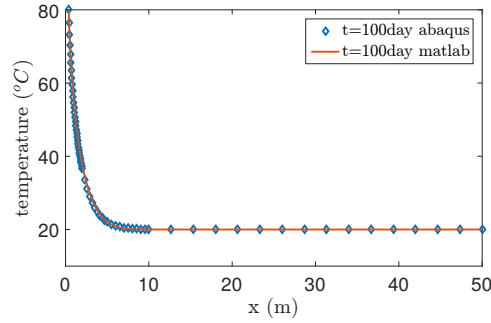
Figure IV .5: Variation of temperature according to the radius distance to the heating wall simulated by Abaqus and Matlab.

6.2   Verification for the TM coupling

We propose a very simple mesh: 4 quadratic elements with 9 nodes as in Figure IV .6.
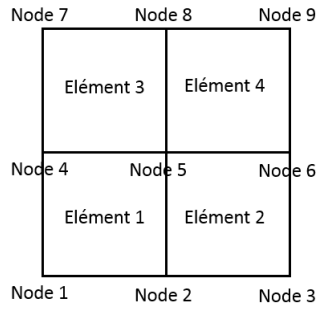
Figure IV .6: Mesh of 4 quadratic elements with 9 nodes.

To verify the function of TM coupling. We first fix the pore pressure($\Delta p = 0$), and we have the temperature increased on all 9 nodes: $\Delta T = 10^o C$.

The analytical result is obtained by:

$$\sigma_{analytical} = -3 * K_{drainé} * \alpha_{drainé} * \Delta T = -26208000 Pa \qquad \text{(IV .61)}$$

with $K_{drained} = 6.93e9 Pa$, and $\alpha_{drained}$=1.26e-4.

Comparing with the result simulated by Matlab code, we can see that the stress values σ_{xx} and σ_{yy} are equal to the analytical result.

Figure IV .7: Temperature-dependent calculated stress result by Matlab code.

6.3   Verification for the THM coupling

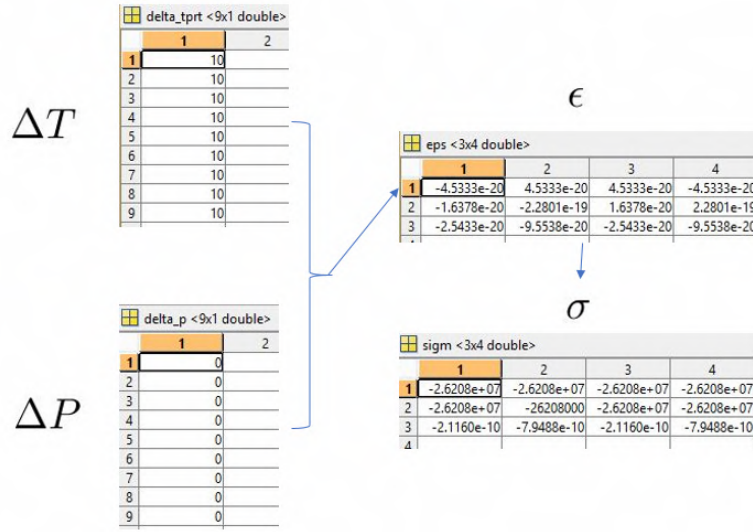We always use the same mesh of 4 quadratic elements with 9 nodes to check the THM coupling. In this example, he studies the influence of ΔT on the pore pressure field. And then, the variations of the TH fields leads to a change of mechanical field.

In this case, the pore pressure is not fixed. At first, we can calculate the increased pore pressure ΔP because of heating:

$$\Delta P_{analytical} = 3 * \alpha_m * M_{Biot} * \Delta T = 53570880 Pa \tag{IV .62}$$

with $\alpha_m = 2.576e - 4$, and $M_{Biot} = 6.93e9$.

Finally, we can calculate $\sigma_{analytical}$ dependent on ΔP and ΔT by:

$$\sigma_{analytical} = -b * \Delta P_{analytical} - 3 * \alpha_{drained} * K_{drained} * \Delta T = -5.7114e7 Pa \tag{IV .63}$$

with $\alpha_{drained} = 1.26e - 4$.

Comparing with the result calculated by Matlab code(Figure IV .8), we can see that results of the variation of pore pressure ΔP and the stress σ are equal to the analytical result.
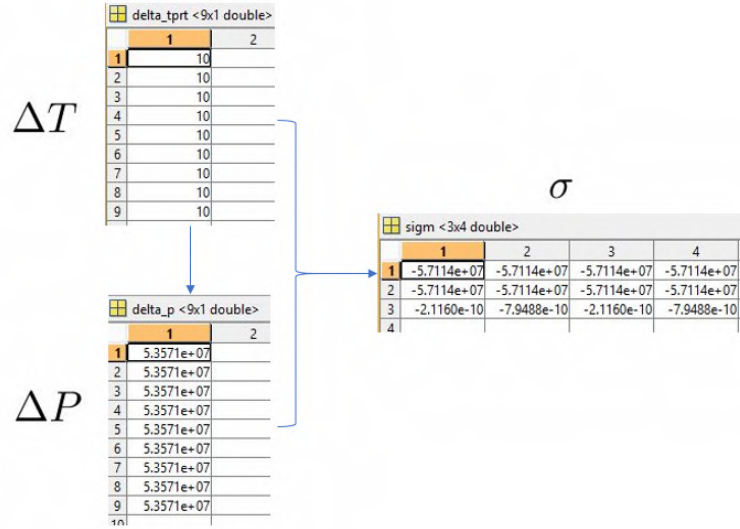
Figure IV .8: The input: variation of temperatureΔT; the output: variation of pore pressure ΔP and the stress calculated by Matlab code.

6.4 Verification for the HM coupling

A single element is used here to verify the HM coupling. Here, we compress this element as in Figure IV .9. This test shows us the influence of Δu to the pore pressure field.
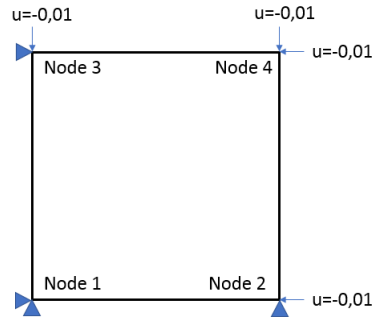
Figure IV .9: Mesh of a single quadratic element.

Under the compression load, a variation of pore pressure is obtained. The analytical value can be calculated by:

$$\Delta P_{analytical} = -M_{Biot} * b_{Biot} * (\epsilon_{xx} + \epsilon_{yy}) = 8e6Pa \qquad \text{(IV .64)}$$

By comparing the result calculated by Matlab code (Figure IV .10) with this value $\Delta p_{analytical}$. We can find that the code is working well on this HM coupling.
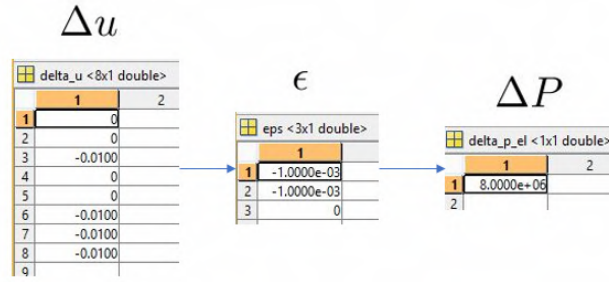
Figure IV .10: The input: the variation of deformation Δu and the strain ϵ; the output: the variation of pore pressure ΔP calculated by Matlab code.

7 Examples simulated by THM-d coupling

In this section, we will see 3 examples simulated by our model of THM-d coupling.

7.1 Example 1

In example 1. We will see the phase field method does not depend on the mesh. This is an important feature of the phase field method and should be noted in structural calculations, as well as the feature of our THM-d modeling.

The material is used: E = 4500MPa, $\nu = 0.3$, to make a single-edge tension test: (Figure IV .11).
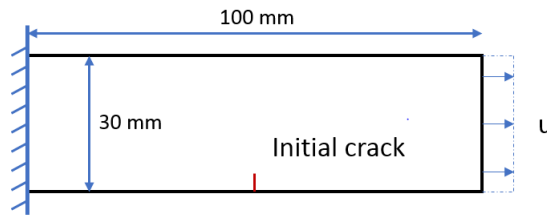
Figure IV .11: Single-edge tension test. Boundary conditions and geometry.

We define 2 different meshes: (Figure IV .12) and (Figure IV .13). The number of elements of the second mesh is 4 times higher than the first one. But they have the same width of smeared crack $l_d = 3 \times 10^{-3}m$, and $g_c^t = g_c^{sh} = 40N/m$.
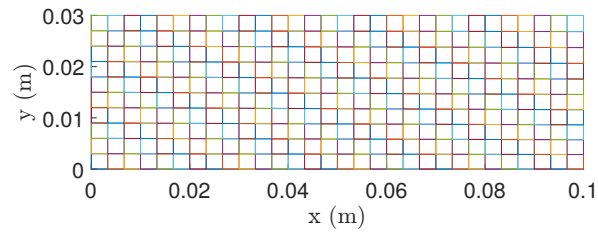
Figure IV .12: Mesh of 30×10 quadrilaterals elements(element size=$3\times10^{-3}m\times3\times10^{-3}m$)
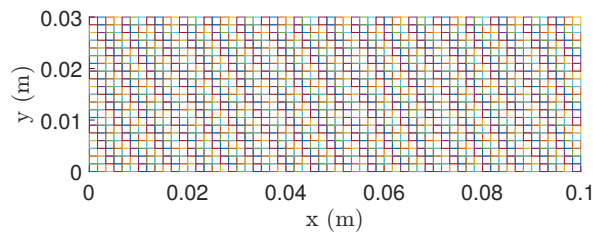
Figure IV .13: Mesh of 60×20 quadrilaterals elements(element size=$1,5\times10^{-3}m\times1,5\times10^{-3}m$)

In the Figure IV .15 we can see the results of distributions of tensile damage. The crack can be seen to propagate from the initial crack through the displacement load. The two crack paths are almost the same at the same step of the displacement load.
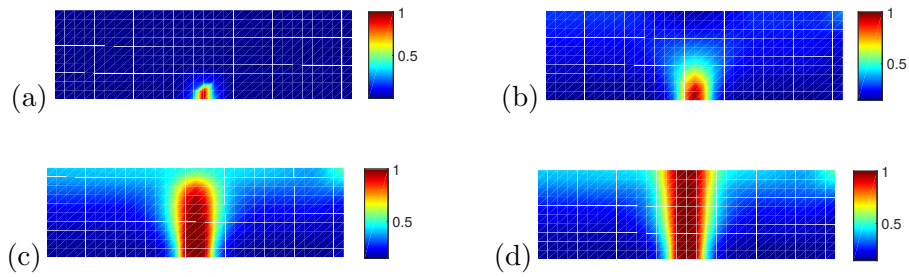
Figure IV .14: Chemin de fissure obtenu avec le maillage de 30×10 éléments quadrilatéraux pour: (a) $u = 0.01mm$; (b) $u = 0.1mm$; (c) $u = 0.14mm$; (d) $u = 0.16mm$
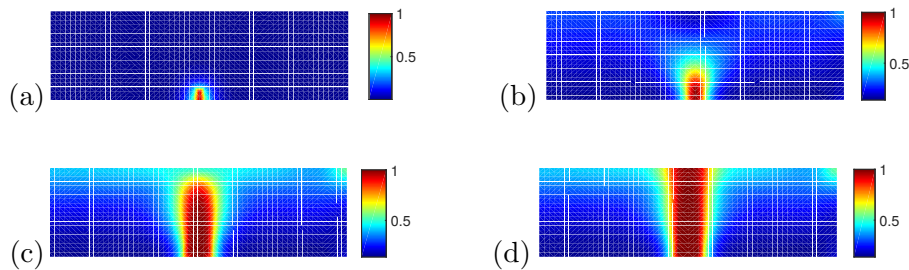
Figure IV .15: Crack path obtained with the mesh of 60×20 quadrilateral elements for: (a) $u = 0.01mm$; (b) $u = 0.1mm$; (c) $u = 0.14mm$; (d) $u = 0.16mm$

But if we change the width of the crack, the l_d, we can see their force-displacement curve. The results are different. The larger l_d means that the yellow line, leading to the crack, spreads most easily through the material because it requires the smallest displacement load.
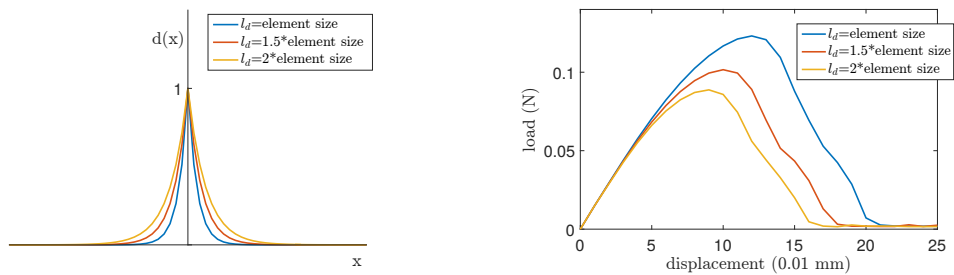

Figure IV .16: Diffuse crack modeling and force-displacement curve for single-edge tension testing with the 3 different l_d

7.2 Example 2

Test 2 shows the thermo-mechanical coupling. Here we have a decrease in the temperature of the material as a thermal load. The studied material has an initial crack.

The parameters used are shown here:

- Young's modulus & Poisson's coefficient: E = 4500MPa; $\nu = 0{,}3$

- Toughness parameter: $g_c^t = g_c^{sh} = 40$N / m

- Width of the diffuse crack: $l_d = 1.5 \times 10^{-3}$ m

- The expansion coefficient of material: $\alpha = 5 \times 10^{-4}$

- Thermal conductivity: $\lambda_{con} = 1.65 W/m.^oC$
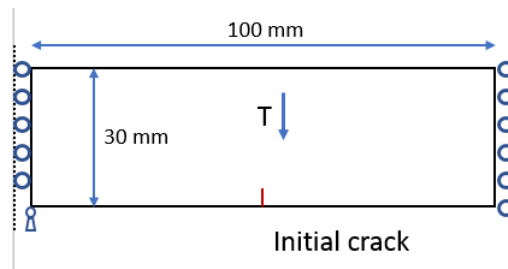
Figure IV .17: Test of decrease of the global temperature. Boundary conditions and geometry.

And then, we can see the propagation of the initial crack depends on the decrease of temperature as shown in Figure IV .18.
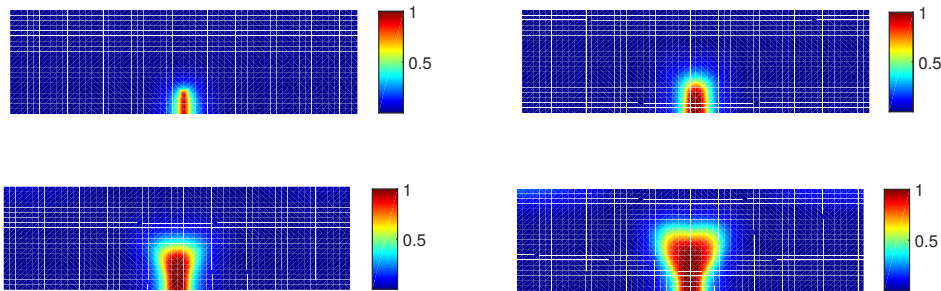
Figure IV .18: Crack path obtained with the mesh of 60×20 quadrilateral elements for: $\Delta T = 0^oC$; $\Delta T = -10^oC$; $\Delta T = -14^oC$; $\Delta T = -20^oC$

7.3   Example 3

In Example 3, it shows the function of the complete THM coupling. We have a heating point in the center of a plate as a thermal load. The boundary conditions and geometry are presented as in Figure IV .19.

The parameters used are mentioned here:

- Young's modulus & Poisson's coefficient: E = 4500MPa; $\nu = 0.3$;

- Toughness parameter: $g_c^t = g_c^{sh} = 40$N / m;

- Width of the diffuse crack: l_d = element's size = $0.04m$;

- The expansion coefficient of material: $\alpha = 3 \times 10^{-5}$;

- Thermal conductivity: $\lambda_{con} = 1.65 W/m.^oC$;

- Permeability: $k = 4.5 \times 10^{-20} m^2$;

- Biot coefficient: $b_{initiale} = 0.6$;

- Porosity: $\phi_{initiale} = 0.16$.
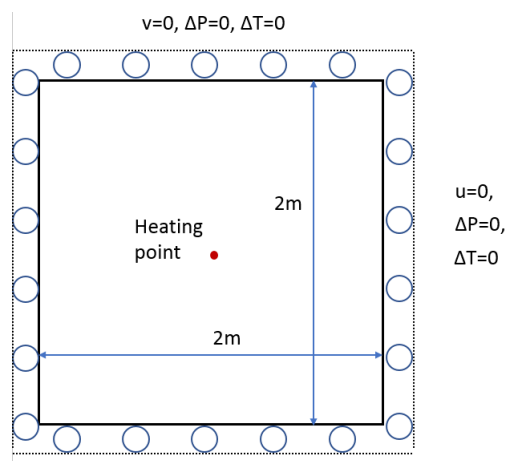
Figure IV .19: Central heating point test. Boundary conditions and geometry.

In the first 24 hours, the temperature of this heating point increases from 20 degrees to 80 degrees linearly.(Figure IV .20(a))
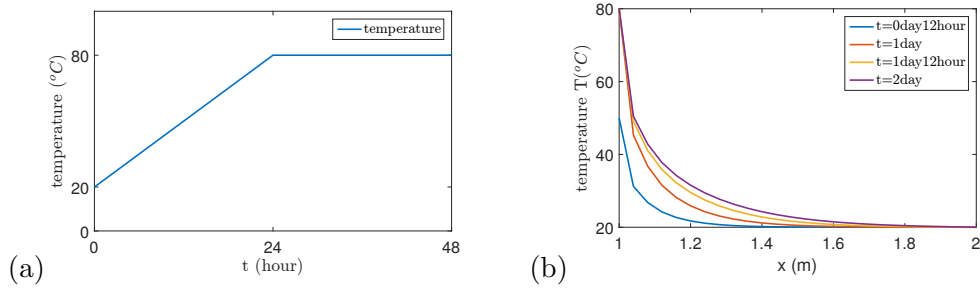
Figure IV .20: (a)Temperature applied to the heating point as a function of time; (b)Temperature variation section (from center point to edge)

We can see the increase of temperature from the center point to right edge in 48 hours as shown in Figure IV .20(b).

Figure IV .21 shows the temperature distribution at t = 48 hours, it can be seen that the high temperature zone propagates from the central point to the outer edge.
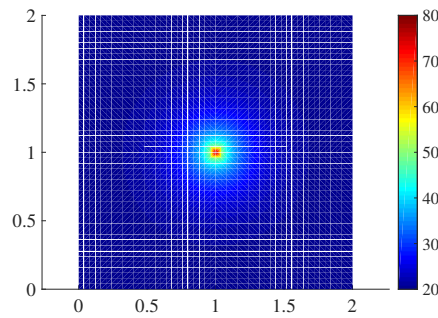
Figure IV .21: The distribution of temperature (^{o}C) at t = 48 hours

The heating leads to the increase of pore pressure, and the area of high pore pressure appears at the center point of the plate, and then this area extends during heating as shown in the Figure IV .22.
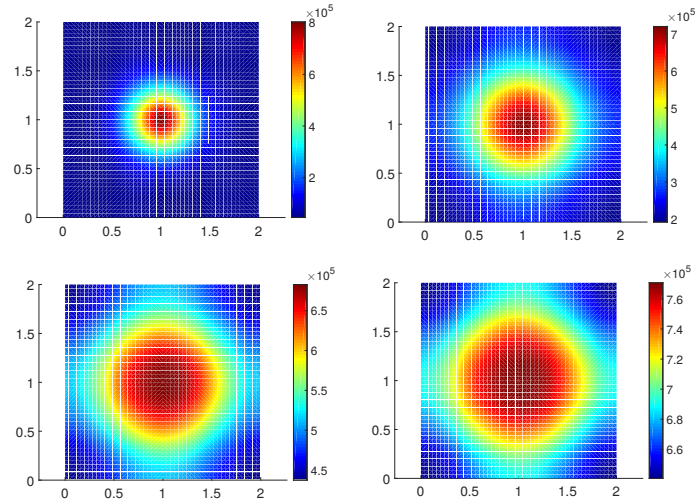
Figure IV .22: The distribution of pore pressure (Pa) for t =: 12 hours; 24 hours; 36 hours; 48 hours

Finally, in the distributions of the tensile damage field shown in the Figure IV .23. The tensile damage zone appears at the heating point and then extends, the value of d^t increases according to the variations of temperature and pore pressure.
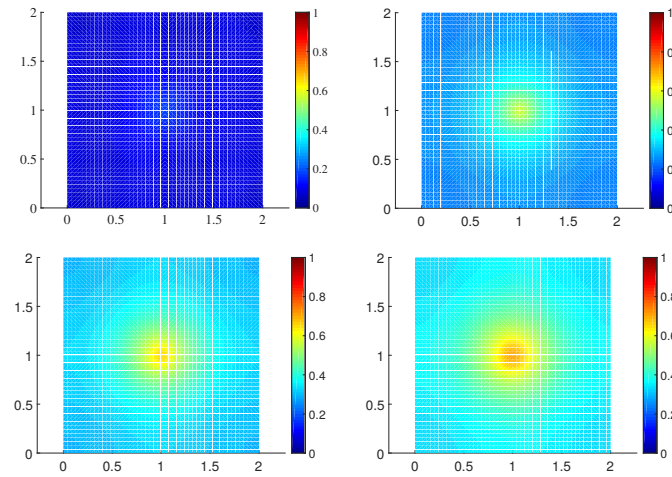
Figure IV .23: The distribution of tensile damage at t =: 12 hours; 24 hours; 36 hours; 48 hours

Here, if we change the isotropic permeability to anisotropic one:

- $k_h = 4.5 \times 10^{-20} m^2$;

- $k_v = k_h/5 = 0.9 \times 10^{-20} m^2$.

We can see the result of the temperature(Figure IV .24) does not change compared with Figure IV .21.
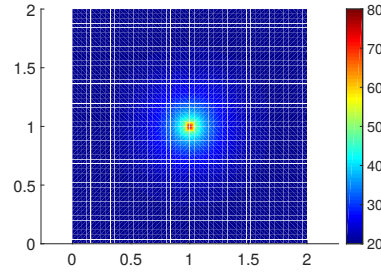
Figure IV .24: The distribution of temperature (^oC) at t = 48 hours

But for the result of the distribution of the pore pressure(Figure IV .25(a)), the horizontal pore pressure increases more rapidly. Finally, it leads to the same form of distribution of the area of tensile damage as shown in the Figure IV .25(b).
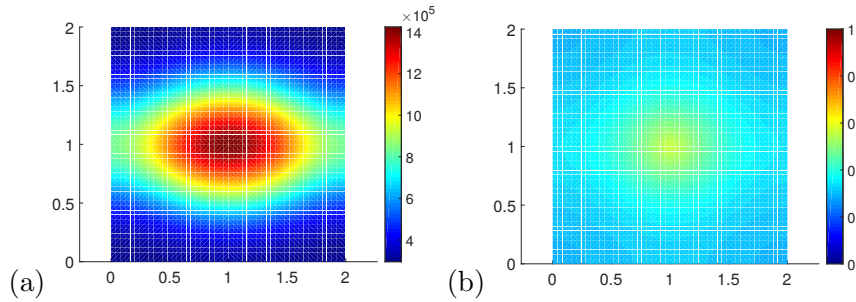
Figure IV .25: (a)The distribution of pore pressure (Pa); (b)The distribution of tensile damage field at t = 48 hours

8   Conclusion

This Chapter has presented the theoretical background of THM coupling. Based on this coupling, the THM fields and tensile, shear damage fields are successfully coupled. The damage fields are considered as the independent field which has its own partial differential equation to calculate the damage values. The code is verified by several simple tests. And the damage zone can be obtained by the charge of the temperature loading in the proposed examples.

In this context, in the following chapters, we will present the coupled THM modeling of two in situ experiments.

Chapter V

Examples of applications to the problem of radioactive waste disposal

Contents

1 Introduction

In general, the analytical resolution of a problem of continuum mechanics applied to civil engineering works is a task rarely possible. The equations of physics only make it possible to obtain exact solutions in a few particular cases which often have only a distant relation with the reality of the works. This is why analytical methods of approximate calculation

have been developed. At the same time, the constant development of computer resources is at the origin of the progress made in the implementation of numerical calculation methods.

By the way, a numerical calculation, and all that he understands remains an idealization of reality. If the preceding chapters have been established according to a modeler approach, the applications of this last chapter are oriented according to the point of view of the engineer. And for us, we use the modeling to link computer techniques and those of the techniques of the engineer builder.

In this chapter, we show two applications to the problem of radioactive waste disposal from French national radioactive waste management agency(ANDRA): tunnel excavation modeling GCS test and tunnel heating modeling ALC test. The contexts of the test and benchmarks of the simulation are described in detail at the beginning of every modeling. The experimental results and simulation results are compared in all aspects from the temperature, the pore pressure, the displacement and the most important study for us: the distributions of damage.

2   GCS test

2.1   General context

The construction of the Meuse/Haute-Marne URL has been launched in 2000 in Bure located about 300 km North-East of Paris by Andra to demonstrate the feasibility of a radioactive waste repository in a Callovo-Oxfordian claystone formation. An important experimental program is planned to characterize different properties of the host rock and to study its response to the different shaft and drift excavation. Numerous experiments and direct measurements have been performed in the laboratory drifts excavated at -445 m and then at -490 m (the main level).

The Callovo-Oxfordian claystone (COx) is considered as a potential geological formation to host an industrial radioactive waste repository in France, because of its favorable characteristics for radioactive waste containment, as it has a very low hydraulic conductivity, small molecular diffusion and significant retention capacity for radionuclides. A deep understanding of the thermo-hydro-mechanical (THM) response of the COx in different repository conditions is a key issue for the design of different structures and the safety calculations of the project.
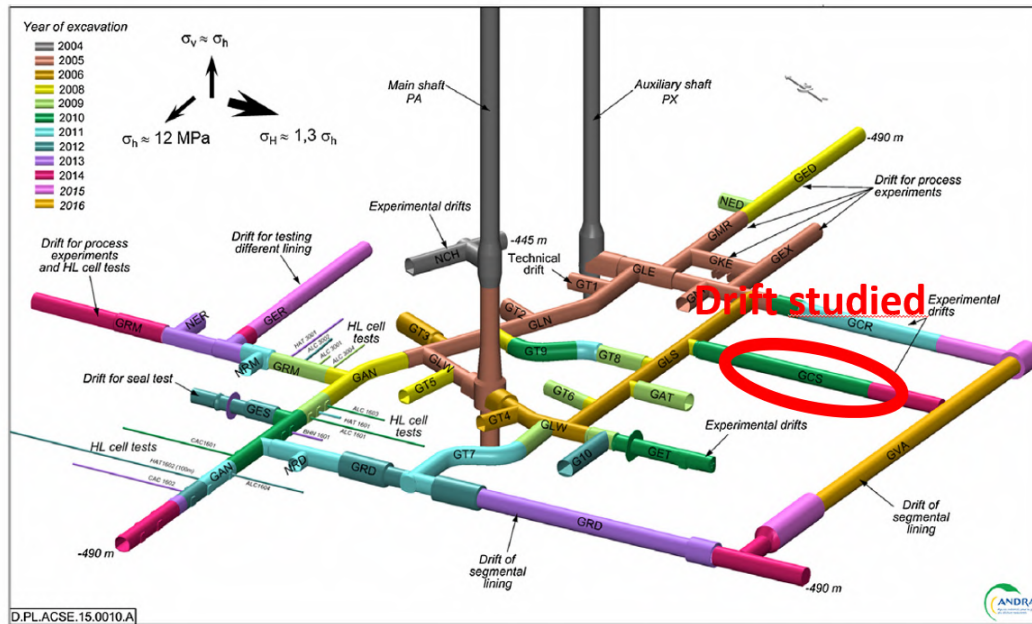
Figure V .1: General view of the GCS experiment. [Seyedi et al., 2017]

The GCS drift(Figure V .1) has been excavated in the direction of the major horizontal stress from the south drift (GLS) and 30 m away from the GAT drift in order to restrict hydro-mechanical interference between the two drifts (at short time). The GCS has a perfectly circular section with a 2.6 m radius. The digging was performed with a road header (Figure V .2), which allowed getting an average over excavation lower than 0.1 m, except at the floor where it could reach 0.4 m.
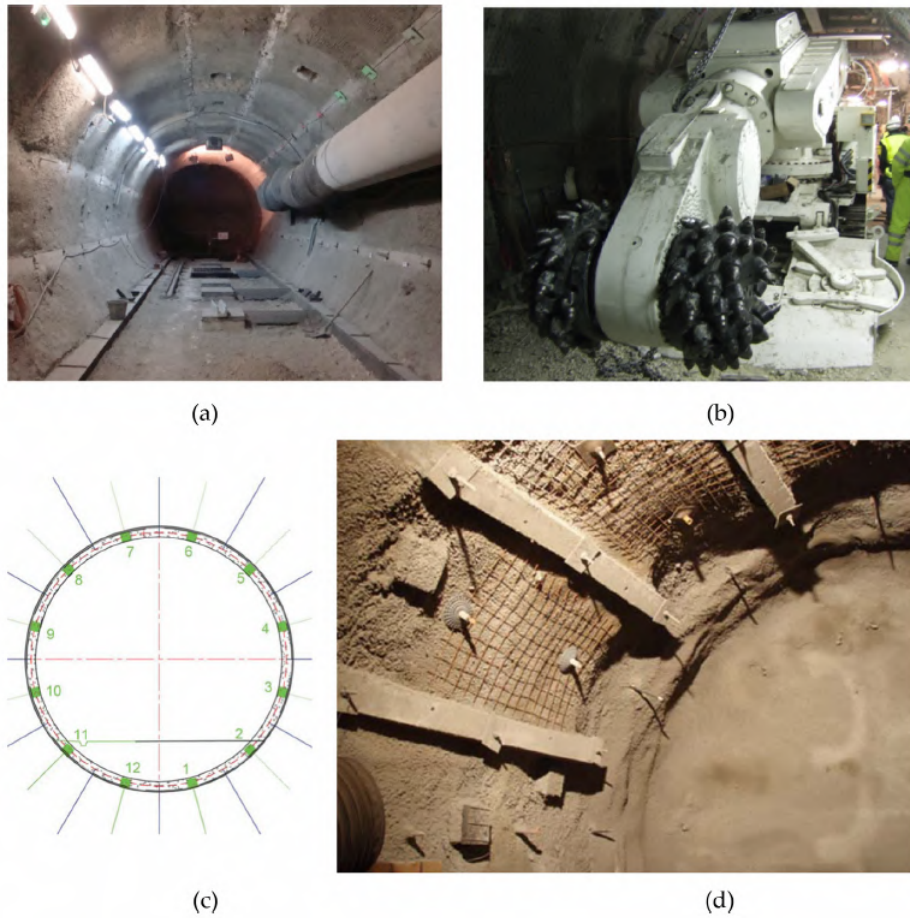
Figure V .2: (a) GCS drift (without slab); (b) Road-header; (c) GCS section; (d) yieldable concrete wedges. [Seyedi et al., 2017]

2.2   Action Transverse benchmark

A 2D plane strain configuration with the following characteristics is considered as a benchmark to simulate this tunnel excavation modeling:

- Circular section with a radius of 2.6 m;

- A homogeneous initial stress state is considered by neglecting gravity effects

- At the drift section: $\sigma_x = \sigma_h = $ -12.4 MPa, $\sigma_y = \sigma_v = $ -12.7 MPa;

- At the drift axes: $\sigma_z = \sigma_H = $ -16.12 MPa;

- The initial pore pressure is assumed to be equal 4.7 MPa everywhere in the model.

with these characteristics presented, the geometry and boundary condition of GCS gallery can be show as in the Figure V .3.
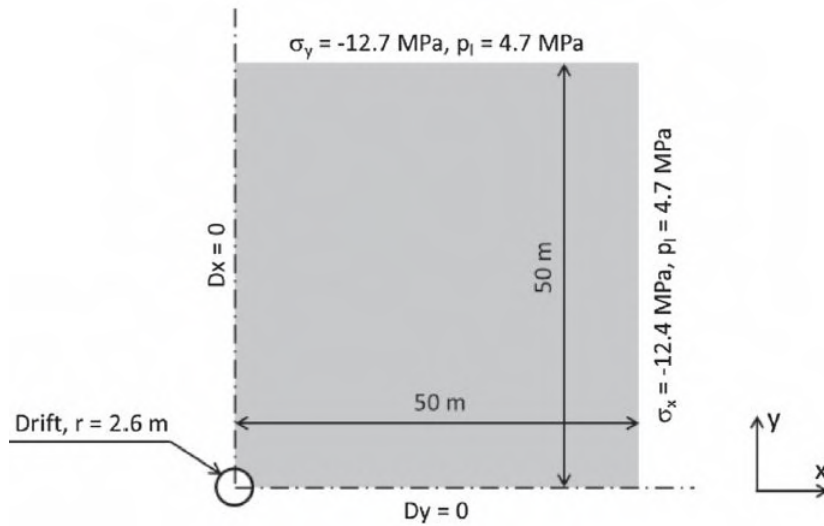
Figure V .3: Geometry and boundary conditions of GCS gallery

The COx claystone is considered as an anisotropic material, this anisotropy is reflected as:

- Elastic parameters: $E_\parallel = 5GPa$; $E_\perp = 3GPa$; $\nu_\parallel = 0.2$; $\nu_\perp = 0.35$.

- Initial permeability: $k_\parallel^0 = 6e - 20m^2$; $k_\perp^0 = 3e - 20m^2$.

with initial Biot coefficient $b_{initial} = 0.6$ and the initial porosity $\phi_{initiale} = 0.16$.

The excavation operation is modeled by the mechanical and hydraulic deconfinement curves presented in Figure V .4.
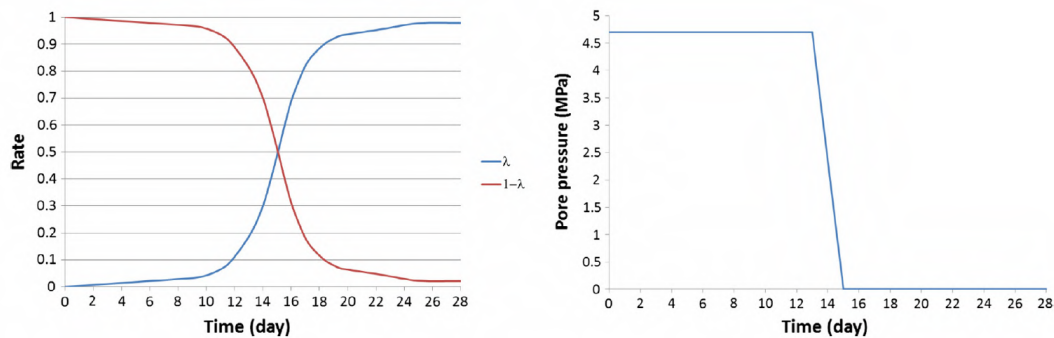
Figure V .4: Mechanical (left) and hydraulic (right) deconfinement curves.

2.3   Viscoelasticity model

For the time-dependent response of the GCS test, a viscoelasticity model used should be presented at first.

In order to simplify the problem, a 1-D model is used to presented here. We use 3 elements model (elastic element + Kelvin-Voigt model) to describe viscoelasticity as shown in Figure V .5.

The total strain is composed by elastic part (ϵ^e) and viscoelastic coupled part (ϵ^v) which are the right part and left part in Figure V .5:

$$\epsilon = \epsilon^e + \epsilon^v \tag{V .1}$$
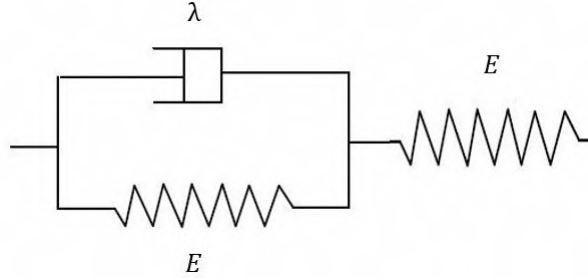
Figure V .5: The 3 elements viscoelasticity model

In the elastic part, we have:

$$\sigma = E\epsilon^e \tag{V .2}$$

And in Kelvin-Voigt model part, we have:

$$\sigma = E\epsilon^v + \lambda\frac{d\epsilon^v}{dt} \tag{V .3}$$

In this part, the increment of strain at time step n is presented as:

$$\triangle\epsilon_n^v = \dot{\epsilon}_{n-1}^v\triangle t \tag{V .4}$$

with the rate of strain:

$$\dot{\epsilon}_{n-1}^v = \frac{d\epsilon_{n-1}^v}{dt} = \frac{1}{\lambda}(\sigma_{n-1} - E\epsilon_{n-1}^v) \tag{V .5}$$

We define viscosity coefficient λ as a function:

$$\lambda(f(\bar{\sigma}), g(\epsilon_{eq}^v)) = \lambda_0 \cdot f(\bar{\sigma}) \cdot g(\epsilon_{eq}^v) \tag{V .6}$$

with

$$f(\bar{\sigma}) = \alpha \bar{\sigma}^n \tag{V .7}$$

and

$$g(\epsilon_{eq}^v) = exp(\frac{\epsilon_{eq}^v}{\beta}) \tag{V .8}$$

At last, we add the effect of damage fields. The model is considered as an viscoelasticity-damage problem.

In this model, the viscous strain contributes to create the damage. So we define the effective strain which is composed by elastic strain and viscous strain:

$$\epsilon^{eff} = \epsilon^e + \epsilon^v \tag{V .9}$$

And then, this effective strain would be used to calculate the crack driving energy as presented in the first Chapter:

$$F^\alpha = -\{\frac{\partial W_{eff}(\epsilon^{eff})}{\partial d^\alpha} + g_c^\alpha \delta\gamma^\alpha(d^\alpha)\} = 0 \tag{V .10}$$

On the other side, because the stiffness matrix is influenced by damage value $\mathbb{C}(d^c, d^t)$, we should rewrite the stress equation as:

$$\sigma = \mathbb{C}(d^c, d^t)\epsilon^e \tag{V .11}$$

So for the rate of strain, we have:

$$\dot{\epsilon}_{n-1}^v = \frac{d\epsilon_{n-1}}{dt} = \frac{1}{\lambda}(\sigma_{n-1} - \mathbb{C}(d^c, d^t)\epsilon_{n-1}^v) \tag{V .12}$$

As we can see in FEM discretization equation of viscoelastic model, we have:

$$K\triangle u = \triangle R + \triangle R^v \tag{V .13}$$

with:

$$K = \int_\Omega B^T \mathbb{C}(d^c, d^t)B d\Omega \tag{V .14}$$

$$\triangle R^v = \int_\Omega B^T \mathbb{C}(d^c, d^t)\triangle\epsilon_n^v d\Omega \tag{V .15}$$

The equivalent viscous load could be influenced by damage at every time step.

A simulated creep tests were also performed under triaxial loading conditions as presented in Chapter 2. In this case the loads of displacement were stopped once the desired deviatoric stress was reached. From then on, the stress state was kept constant for a specified period of time. Three tests were performed at a onfinement pressure of 12MPa and

with different ratios between applied and maximum deviatoric stresses(50%, 75%, 90%). Figure V .6 shows the results obtained in terms of time-dependent deformation.
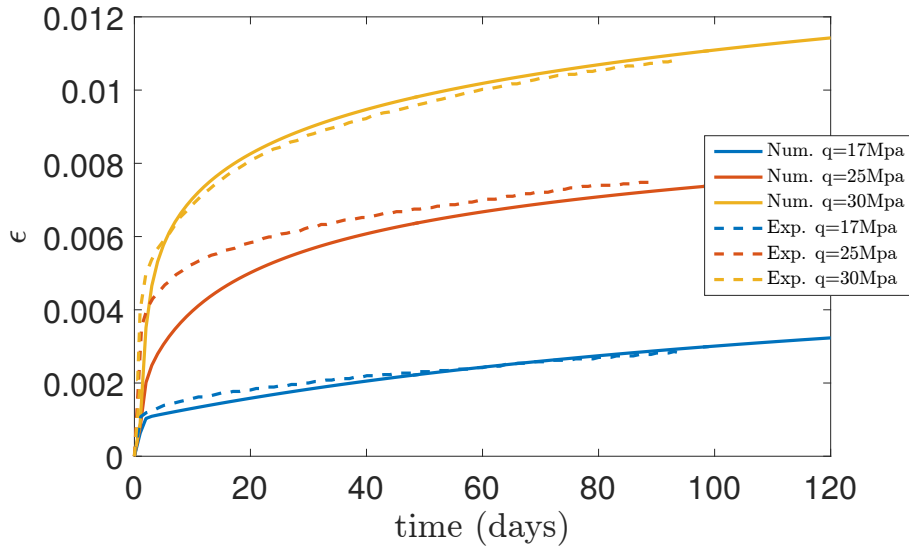
Figure V .6: Creep tests on COx claystone compared between numerical results and experimental results [Armand et al., 2017].

2.4   Modeling results

According to the excavation operation. The principal phenomenon is reflected at the variation of the pore pressure and displacement. The results from the numerical simulations are compared with field observations. Figure V .7 shows the location of the measurement points on the plane normal to the tunnel axis that have been used in the comparisons. They belong two devoted to the measurement of liquid pressure (OHZ1521, OHZ1522), and the other one to the measurement of rock displacements with an extensometer (OHZ1501). All of them were installed prior the excavation of the GCS drift. Also, a number of convergence sections installed along the drift during the excavation (OHZ170_24, OHZ170_36) are also considered.
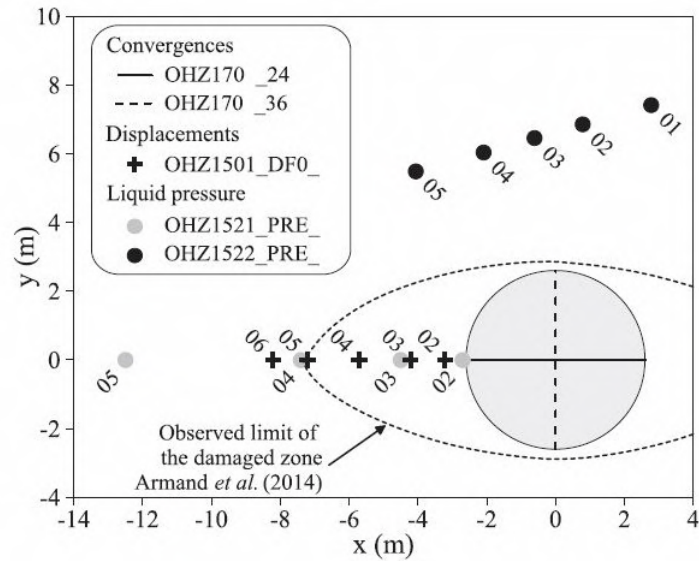
Figure V .7: Location of measurement points used for comparison with simulation results. [Mánica et al., 2017]

The Figure V .8 and V .9 presents the results of pore pressure between experiment and simulation at the sensors points. And Figure V .10 shows the distribution of the pore pressure at t=28 days which is the end of the excavation operation. There are 3 special areas should be explained.

The first area, it's the area of the sensor 04. The anisotropy of the elastic behavior of rock leads to this distribution of pore pressure. The initial pore pressure is equal to 4.7MPa, there's an overpressure zone appears at the horizontal direction of the gallery, and the pore pressure at the vertical direction of the gallery is reduced. The results of sensor 04 presents this overpressure zone very clearly, which is the red zone in the distribution figure(Figure V .10), and the orange line in Figure V .8. It increases during the excavation. The numerical results, the dotted orange line is well reproduced this increasing tendency. But our maximum pore pressure value does not reach to the maximum value of experiment at this point measured. We attribute the reason to the limit of our 2D model. Because before the excavation process arrives to our studied 2D plan, the pore pressure of this 2D plan has already been increased by the excavation, especially in the area near the wall of gallery. The evidence is that the initial value of pore pressure measured by sensor 04 is 6MPa, in other word, at the start of the excavation, t=0. The 3D model might bring the better result to this issue.

The second area is the area of sensor 02, which is the area near the wall of excavation. In this area, the rock is damaged because of the excavation and the overpressure zone. The

permeability is increased, it accelerates the seepage process of water in this damaged area. The third area is the area of sensor 05, which is the area far from the excavation surface. The pore pressure of this area does not change a lot.
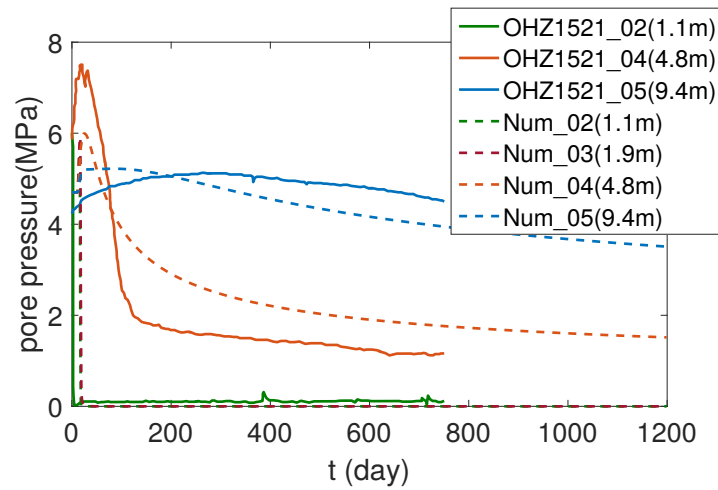
Figure V .8: Pore pressure evolution in measurement points of OHZ1521(horizontal direction) and computed values.
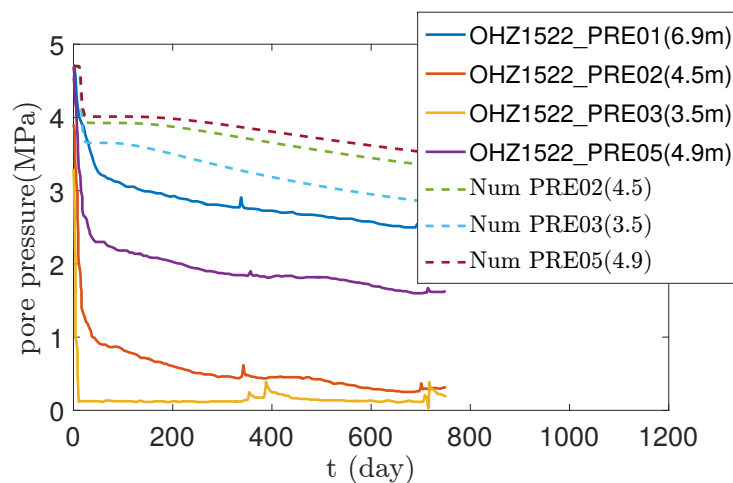
Figure V .9: Pore pressure evolution in measurement points of OHZ1522(vertical direction) and computed values.
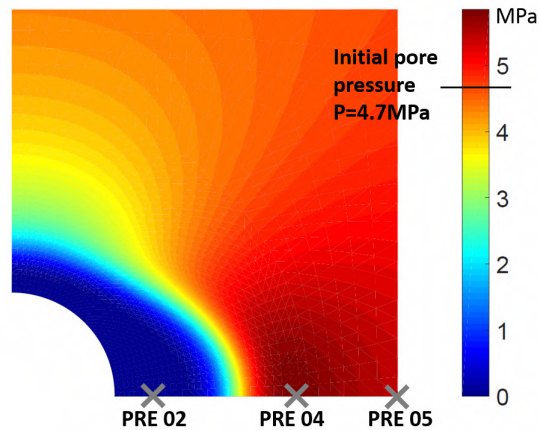
Figure V .10: Distribution of pore pressure at the end of the excavation(t=28days).

Figure V .11 shows the simulated distribution of damage at t=28 days which is the end of the excavation. And Figure V .12 is the conceptual model based on the results of experiment. We can see that the simulated and experimental forms of the damaged zone are very similar. The damaged zone appears at the horizontal direction of the gallery. And the tensile damage zone appears at the area near the gallery, the shear damage zone extends deeper. And only tensile damage zone leads to the increasing of the pore pressure.

(a)   (b)
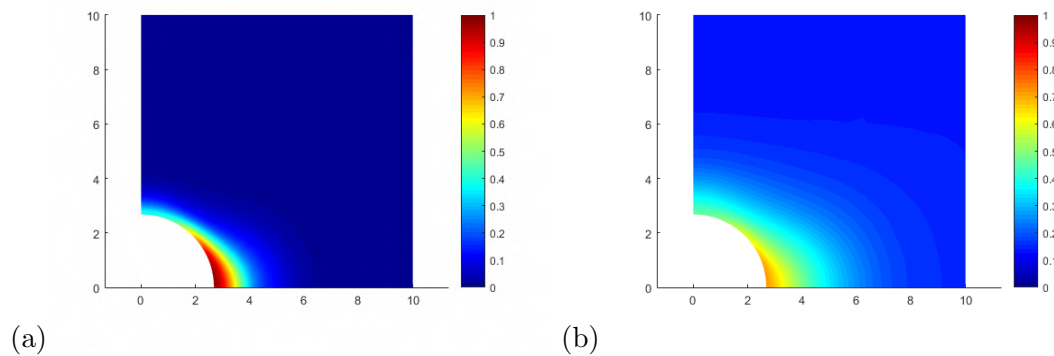
Figure V .11: The distribution of (a)tensile damage and (b)shear damage at t=28 days.
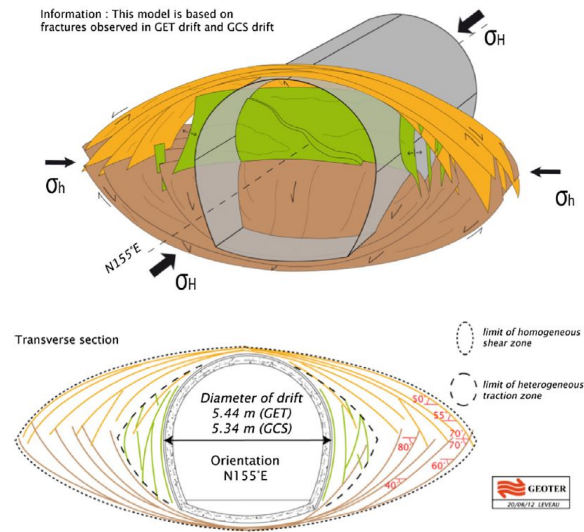
Figure V .12: Conceptual model of the induced fracture networks around drifts of GCS. Dark and light brown surfaces show shear fractures and green ones extension fractures. [Seyedi et al., 2017]

Figure V .13 shows the results of the convergences. During excavation, the diameter of the gallery will decrease because of the collapse. We call this decreasing of diameter convergence. The horizontal diameter converges more than the vertical one, even though the initial parallel Young's module is bigger than the perpendicular one. Because the damage area mainly appears at the horizontal direction. This is an interesting phenomenon, and we successfully reproduce this phenomenon by our hydro-mechanical damage coupling model.
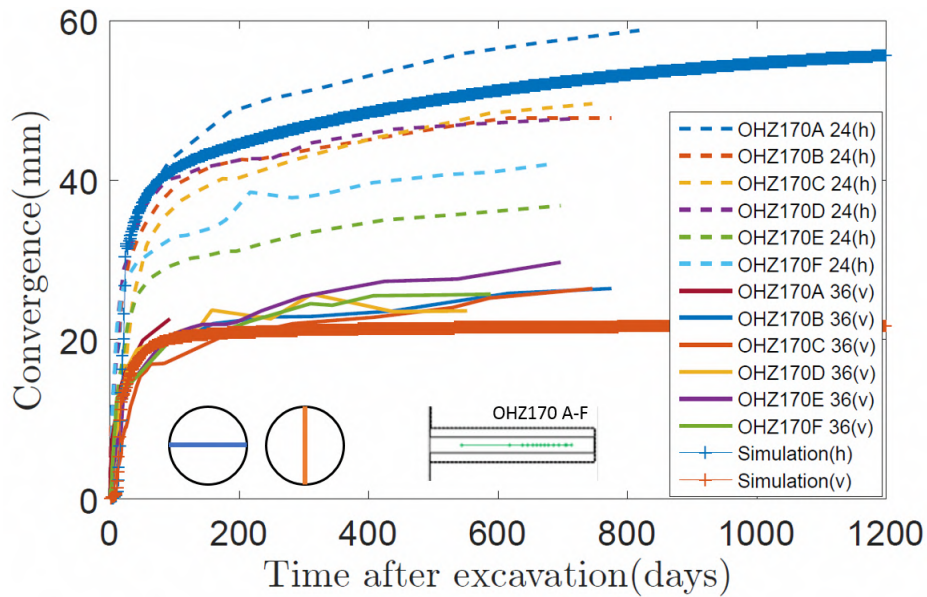
Figure V .13: Evolution of horizontal and vertical convergences. Observed and computed values.

3 ALC test

3.1 General context

The ALC experiment is an ongoing in situ heating test performed in the Meuse/Haute-Marne underground research laboratory. The experiment is a full scale representation of a single high-level waste cell in Callovo-Oxfordian claystone. The main objectives of the experiment are:

- verification of the construction feasibility of a high level waste cell representative of the 2009 reference concept;

- study of the behavior of the cell under thermal loading by simulating the heat produced by waste packages;

- determination of data about the casing behavior under thermal loading;

- understanding the THM behavior of the COx and of the interface between the rock mass and the casing.

The experimental concept has to be representative of what would be a High-level cell for medium exothermal waste packages in the 2009 reference concept (see Figure V .14). The ALC1604 micro tunnel was drilled from the GAN drift and is oriented parallel to σ_H.
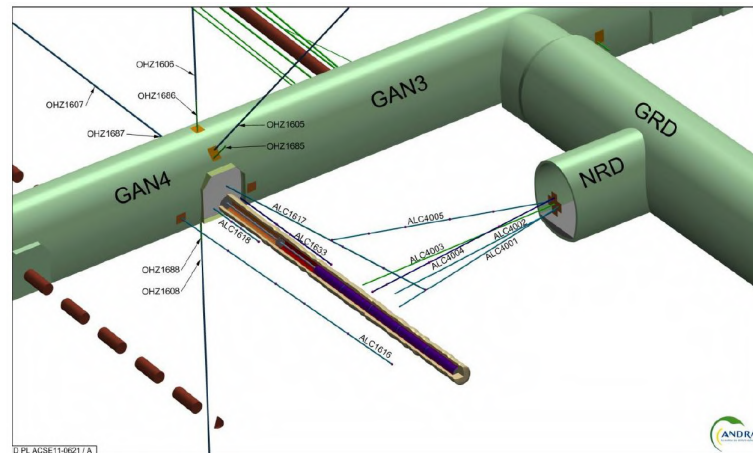
Figure V .14: General view of the ALC experiment.

It has a total length of 25m and the heated part is located in the body part between 10 and 25m deep and is made up of 5 heating elements. Each element is 3 meters long and has a diameter of 508 mm.

The peripheral instrumentation(Figure V .15) in the rockmass includes:

- 2 monopacker boreholes for liquid pressure and temperature measurement (ALC4001 and ALC4002 (the latter appeared to be defective));

- multipacker boreholes for liquid pressure and temperature measurement (ALC4005 and ALC1616 with 5 chambers, ALC1617 and ALC1618 with 3 chambers).

- 2 temperature measurement boreholes at 5 points (ALC4003 and ALC1633)
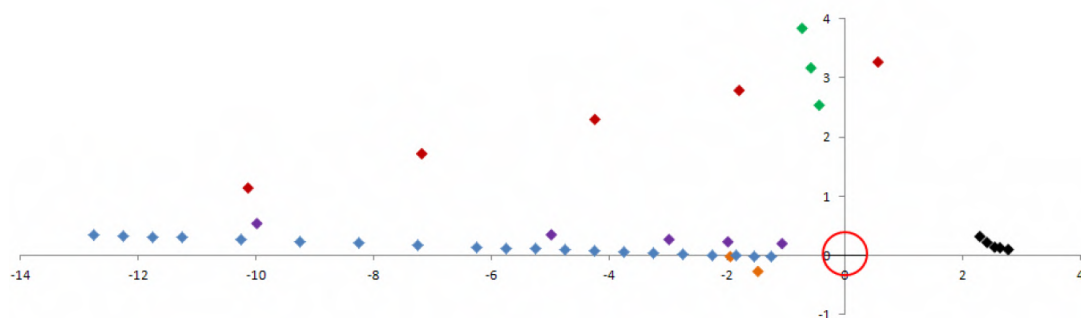
Figure V .15: Distance (in m) between the pore pressure, T and Mag X extensometer measuring chambers and the cell (red circle) – ALC4005 (red), ALC1616 (black), ALC1617 (green), ALC4001 and 4002 (orange), Mag X (blue) and temperature (purple).

The main heating phase started on 18 April 2013, at a constant nominal power of 220 W/m for the 15 m occupied by the heater elements, at a depth of between 10 and 25 m in the cell. This value has been designed to reach a temperature of 90 ^oC at the casing wall after 2 years.

3.2   Introduction of modeling

We simulate this test in a 2D plan like the Figure V .16(a) presented. This 2D plan can be seen as the 17.5m deep of the ALC1604 micro tunnel which is the middle plan of the heating part. The mesh containing 1300 elements and 1386 nodes in this simulation, shown in Figure V .16(b). 24 elements are used to mesh the 1/4 part of the ALC wall, which are the smallest element used in the mesh with the dimension of 0.0271×0.0147m. And we define our width of diffuse crack equals to 0.0147m in our phase field model.
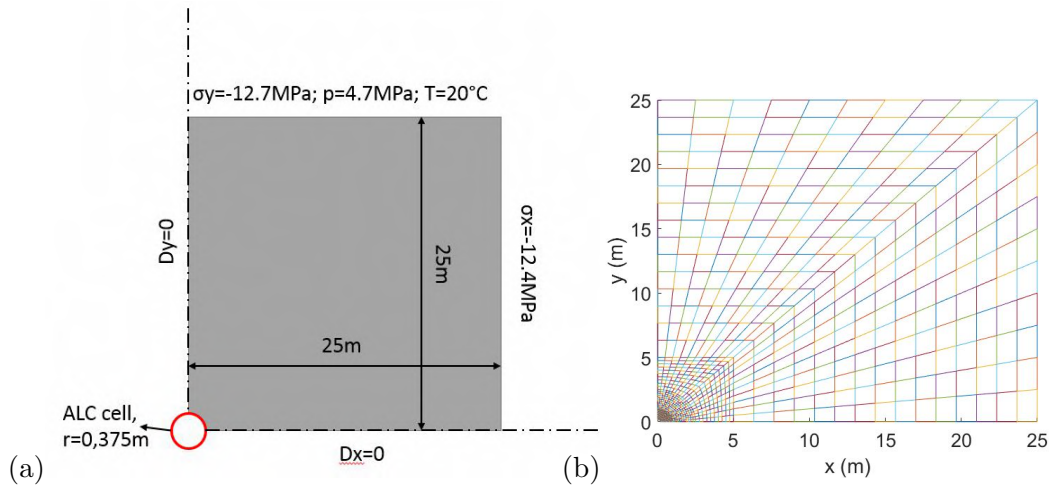
Figure V .16: (a)Modeling domain of the alveolus for 2D plan strain; (b)Mesh for plate with a hole (1/4).

The COx claystone is considered as an anisotropic material with the different elastic behavior, permeability and thermal conductivity in the parallel and perpendicular directions.In the Table V .1, it shows the material parameters in the initial state, which means the claystone is not damaged at all. And they can be influenced by the damage value d^t and d^{sh} during the test, the relation function are shown in the previous chapters.

Elastic parameters	Young's modulus	$E_{\parallel}$=5GPa
		$E_{\perp}$=3GPa
	Poisson's ratio	$\nu_{\parallel}$=0.2
		$\nu_{\perp}$=0.35
Hydraulic parameters	Permeability	$\kappa_{\parallel}$=2 × 10$^{-20}m^2$
		$\kappa_{\perp}$=1 × 10$^{-20}m^2$
	Biot coefficient	b=0.6
	Porosity	Φ=0.16
Thermal parameters	Thermal conductivity	$\lambda_{\parallel}$=2$Wm^{-1}:K^{-1}$
		$\lambda_{\perp}$=1.33$Wm^{-1}:K^{-1}$

Table V .1: The THM material parameter of COx claytone used in this simulation.

The excavation of ALC takes place in the first day during 24 hours. We have mechanical and hydraulic deconfinement like shown in the Figure V .17.

The heating begins at the 176th day after excavation. The equivalent heating power is 220/3 W/m for our 2D model.

The time step used in this example:

- 0-1 day (excavation): 1 hour

- 1-176 days: 1 day

- 176-186 days (heating starts at 176day): 1 hour

- 186-2500 days : 1 day
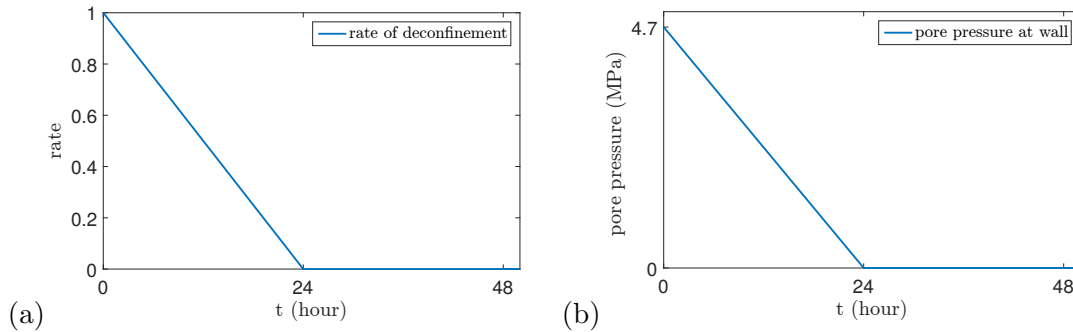
Figure V .17: Variation of the (a) deconfinement coefficient and (b) pore pressure at the excavation surface as a function of time.

3.3   Results of simulation

At first, we choose the sensors set of ALC4003 to compare the results of temperature(Figure V .18). Temperature increase due to heating, is almost well reproduced, the numerical result is higher than the experience result after 1500 days.
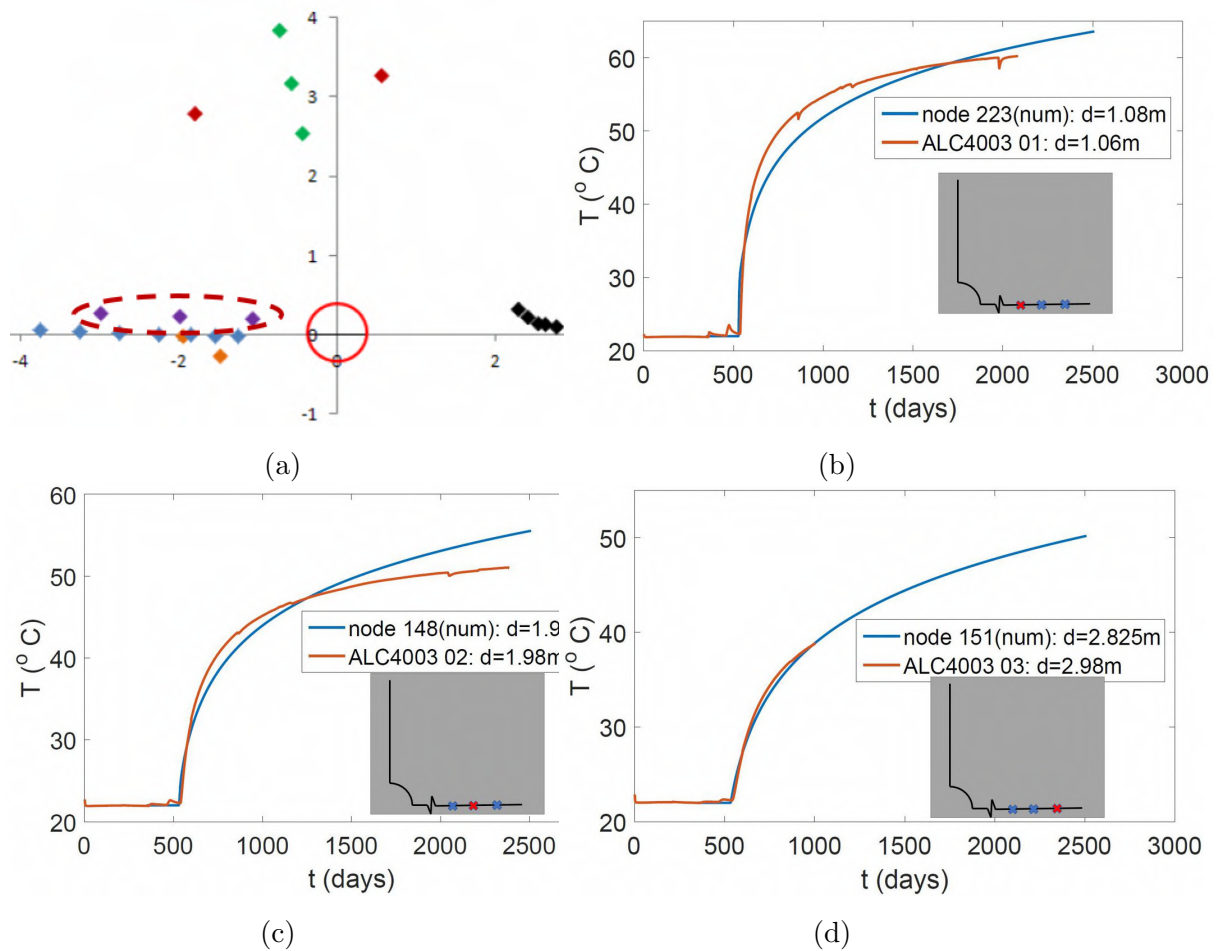
Figure V .18: (a) The position of sensors ALC4003 01-03; Temperature evolution in measurement points of borehole ALC4003, (a) sensor 01: d=1.06m; (b) sensor 02: d=1.98m; (c) sensor 03: d=2.98m.

The Figure V .19, V .20 shows the results of pore pressure simulated compare with the experimental data measured by sensor of ALC1616 02 and ALC1617 02. These two sensors are placed at the horizontal direction and vertical direction of the ALC.

As we can see in the two figures, there are two main processes are presented. The excavation process begins at the line A and the heating begins at the line B.
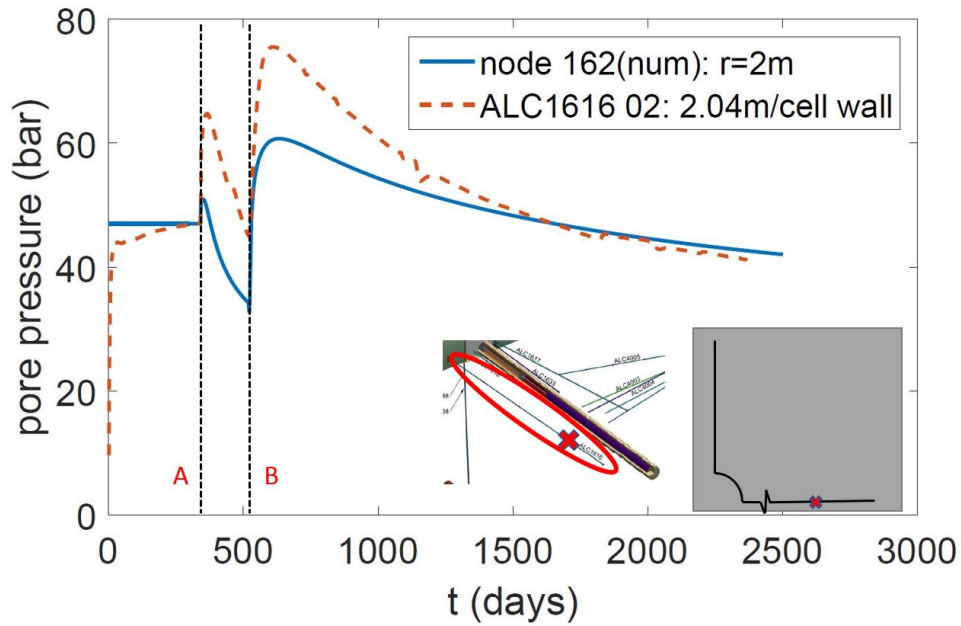
Figure V .19: Pore pressure evolution in ALC1616 (horizontal)
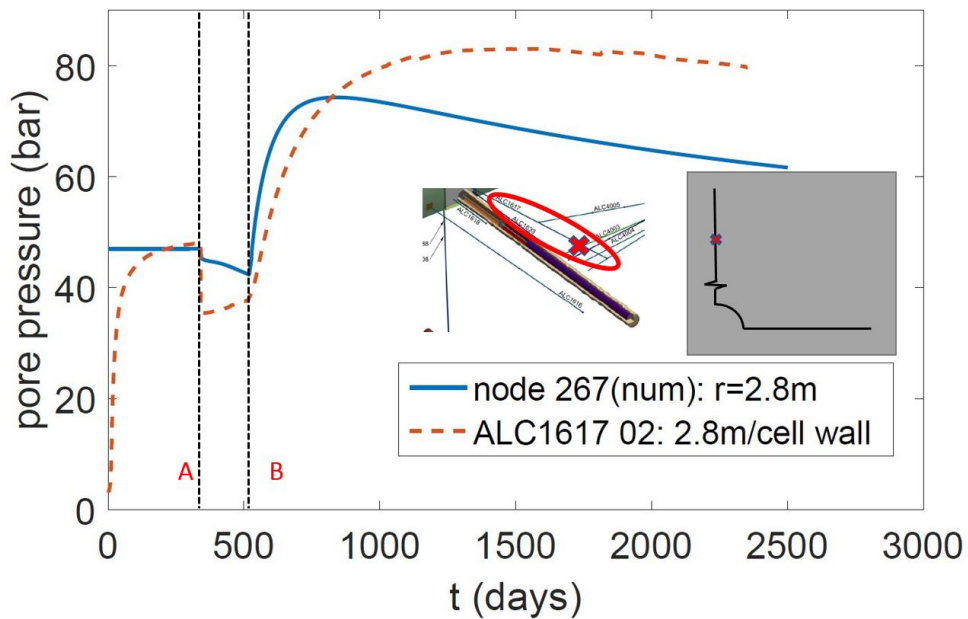
Figure V .20: Pore pressure evolution in ALC1617 (vertical)

At first, during the excavation, the anisotropy of the elastic behavior of COx claystone leads to the distribution of pore pressure shown in Figure V .21. There is an overpressure zone appears at the horizontal direction of the alveole, and the pore pressure at the

vertical direction of the alveole is reduced. The results of ALC1616 02 sensor presents this overpressure zone very clearly. The value of pore pressure at this position of the sensor is increased during the excavation. The numerical results, which presented as the orange dotted line is well reproduced this increasing tendency. But our maximum pore pressure value does not reach the maximum value of the experiment at this point measured. And for the ALC1617 02 sensor, it has the same problem: the pore pressure value simulated does not reach the minimum value of the experiment. We attribute the reason to the limit of our 2D model. Because before the excavation process arrives at our studied 2D plan, the pore pressure of this 2D plan has already been increased by the excavation, especially in the area near the wall of alveole. The excavation process can compress this 2D plane in the direction of axis z. The 3D model might bring better results to this issue.
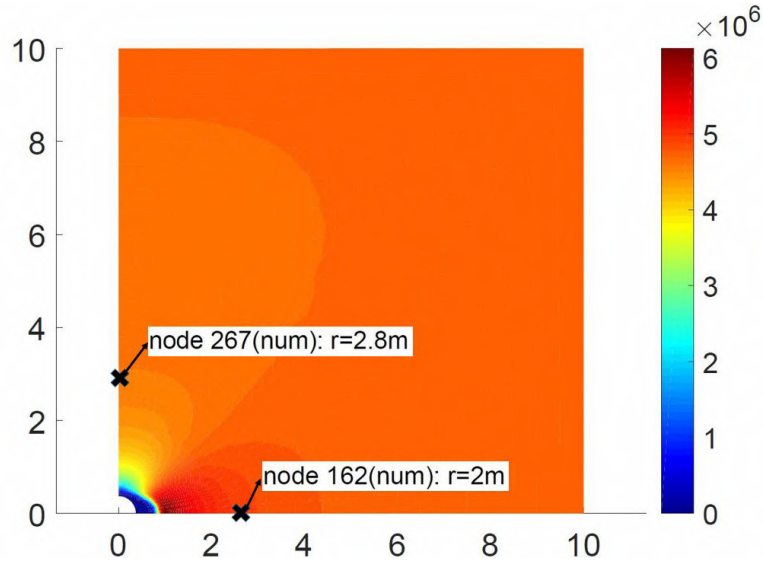
Figure V .21: The distribution of pore pressure(Pa) at t=1 day(after excavation).

In our work, the distribution of damage can be obtain during the test, like shown in the Figure V .22. The photo of distribution of crack around ALC3005 which is shown in Figure V .23 is used here to compare, this alveole has the same direction to our alveole simulated, so it is under the same initial stress, the drift is parallel to σ_H. We can see that the simulated and experimental forms of the damaged zone are very similar. The damaged zone appears at the horizontal direction of the gallery and alveole. The tensile damage zone appears at the area near the excavation surface, the shear damage zone extends deeper.
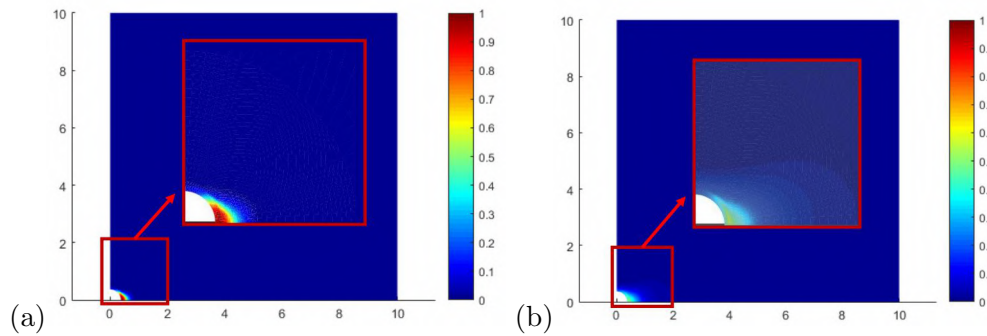
Figure V .22: The distribution of (a)tensile damage and (b)shear damage at t=1 day.
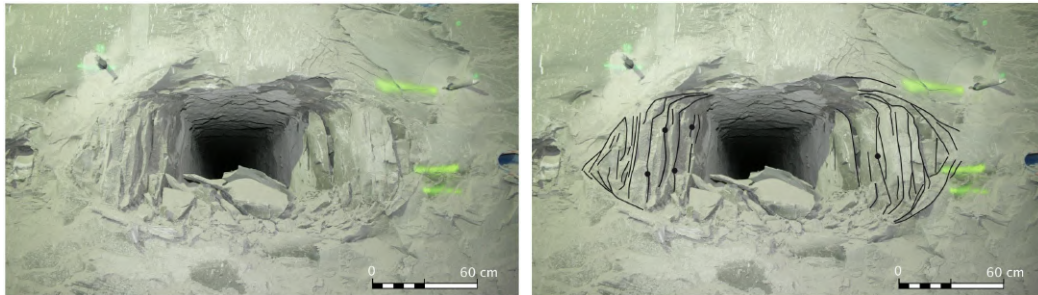
Figure V .23: Photo of structures around ALC3005.

For the heating process, it begins at the line B in the Figure V .19, V .20. It shows the complete function of the THM coupling model. The temperature increases the pore pressure, and the increased pore pressure can influence the mechanical behavior include the damage process. This increasing tendency of pore pressure because of heating is reproduced very well. If we have the same initial pore pressure at the beginning of the heating, the results will become better for the pore pressure.
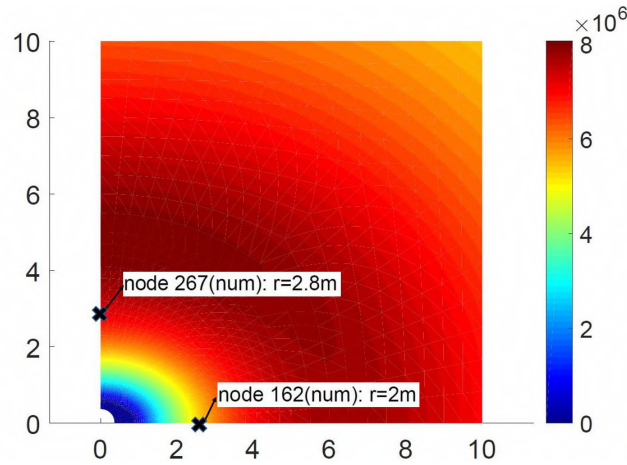
Figure V .24: The distribution of pore pressure(Pa) at t=1190 days

The overpressure zone in this period become a ring shape as shown in the Figure V .24. And it changed the old damaged zone to a new one as in the Figure V .25 shown. The tensile damaged zone extends and the shear damaged zone does not change a lot.
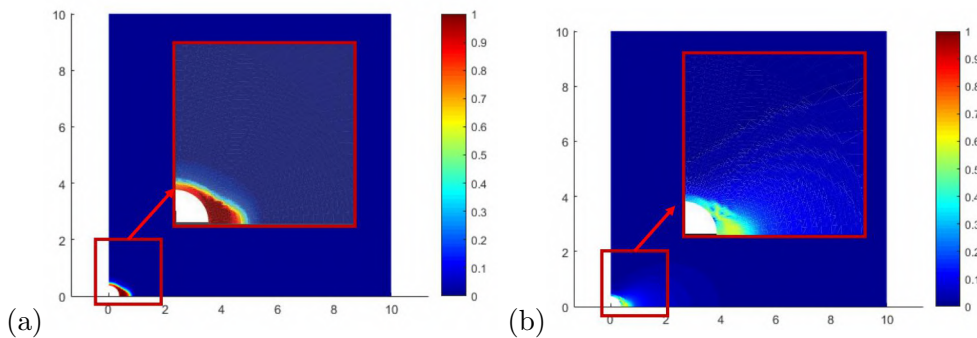
Figure V .25: The distribution of (a)tensile damage and (b)shear damage at t=1190 days

4   Conclusion

In this Chapter, the GCS test and ALC test of ANDRA are introduced and simulated. According to the double phase-field model to calculate and describe the damage, we don't need to define the excavation damaged zone(EDZ) during the underground excavation operation. The independent damage fields are coupled with THM fields, and then they are able to participate in the calculation of coupling at every time step. The effects of the damage zone are reflected in the model of couping, and both of the tensile damage zone and shear damage zone are observable during the excavation operation. Furthermore, the

newly created damage zone because of the heating of the radioactive waste package is also be simulated by our model in the ALC test. With this model which is allowed to describe the appearance of new damage, our results of simulation are more logic and more convincing compare with the other normal FEM model of THM coupling.

Chapter VI

Conclusions and perspectives

1 Conclusions

In the general framework of research projects related to geological disposal of radioactive waste, shale gas production and acid gas sequestration, it is necessary to investigate damage and cracking in COx clayey rocks under coupled thermo-hydro-mechanical loads (THM). Numerical modeling with the finite element method is the principal work that presented in this thesis. For this purpose,

- A double crack phase-field model is proposed for modeling damage and cracking process of cohesive brittle materials. Both tensile and shear cracks are taken into account. Two types of the crack paths can be observed directly during the failure process. The two types of fracture behavior can be controlled by the adjustment of the degradation function and density resistance energy g_c^t and g_c^{sh}. Thanks to the elastic stiffness decomposition, the crack fields can be coupled with both isotropic and anisotropic elastic materials. This model successfully reproduces the triaxial compression test with brittle rock-like materials such as sandstone and Jinping marble. The crack path can be reproduced under the elasticity-damage condition.

- Plastic deformation plays an important role in clayey rocks by controlling the pre-peak deformation and affecting the shear band evolution in the post-peak regime. For this purpose, the double crack phase-field method is extended to adapt to the elasto-plastic damage behavior. Both tensile and shear cracks as well as plastic deformation are taken into account. The adding plastic deformation improves the simulation results of quasi-ductile rock-like materials very well in triaxial compression conditions.

- The THM fields and tensile, shear crack fields are successfully coupled. The crack fields are considered as the independent fields which are governed by their own boundary values problems.

- With the support of ANDRA, the GCS excavation test and ALC heating test have been investigated by using by our model. The tensile and shear crack fields are coupled with the THM fields. The effects of the damage zone on THM fields are taken into account through the evolutions of mechanical properties and permeability. The numerical predictions are in good agreement with in situ observations in terms of THM responses and damage evolutions.

2   Perspectives

In spite of previous studies and the results obtained in this study on modeling of damage and cracking under THM conditions, a number of perspectives are still open and need to be investigated. Some aspects are mentioned below:

- Some improvements of evolution laws for crack fields could be envisaged in order to describe more complex cracking modes (such as mixed mode I and mode II).

- The double phase-field method can be extended to partially saturated conditions in order to study damage and cracking process with the variation of saturation degree.

- The extension to three dimensional configuration is also an important issue in order to capture some geometrical effects on damage and cracking processes.

Bibliography

Ambati, M., Gerasimov, T., and De Lorenzis, L. (2015). A review on phase-field models of brittle fracture and a new fast hybrid formulation. *Computational Mechanics*, 55(2):383–405.

Ambrosio, L. and Tortorelli, V. M. (1990). Approximation of functional depending on jumps by elliptic functional via t-convergence. *Communications on Pure and Applied Mathematics*, 43(8):999–1036.

Amor, H., Marigo, J.-J., and Maurini, C. (2009). Regularized formulation of the variational brittle fracture with unilateral contact: Numerical experiments. *Journal of the Mechanics and Physics of Solids*, 57(8):1209–1229.

Armand, G., Conil, N., Talandier, J., and Seyedi, D. M. (2017). Fundamental aspects of the hydromechanical behaviour of callovo-oxfordian claystone: from experimental studies to model calibration and validation. *Computers and Geotechnics*, 85:277–286.

Armand, G., Noiret, A., Zghondi, J., and Seyedi, D. (2013). Short-and long-term behaviors of drifts in the callovo-oxfordian claystone at the meuse/haute-marne underground research laboratory. *Journal of Rock Mechanics and Geotechnical Engineering*, 5(3):221–230.

Barenblatt, G. I. (1962). The mathematical theory of equilibrium cracks in brittle fracture. In *Advances in applied mechanics*, volume 7, pages 55–129. Elsevier.

Biot, M. A. (1941). General theory of three-dimensional consolidation. *Journal of applied physics*, 12(2):155–164.

Biot, M. A. (1956). General solutions of the equations of elasticity and consolidation for a porous material. *J. appl. Mech*, 23(1):91–96.

Biot, M. A. (1973). Nonlinear and semilinear rheology of porous solids. *Journal of Geophysical Research*, 78(23):4924–4937.

Borden, M. J., Hughes, T. J., Landis, C. M., Anvari, A., and Lee, I. J. (2016). A phase-field formulation for fracture in ductile materials: Finite deformation balance law derivation, plastic degradation, and stress triaxiality effects. *Computer Methods in Applied Mechanics and Engineering*, 312:130–166.

Borden, M. J., Verhoosel, C. V., Scott, M. A., Hughes, T. J., and Landis, C. M. (2012). A phase-field description of dynamic brittle fracture. *Computer Methods in Applied Mechanics and Engineering*, 217:77–95.

Bourdin, B., Francfort, G. A., and Marigo, J.-J. (2000). Numerical experiments in revisited brittle fracture. *Journal of the Mechanics and Physics of Solids*, 48(4):797–826.

Bourdin, B., Francfort, G. A., and Marigo, J.-J. (2008). The variational approach to fracture. *Journal of elasticity*, 91(1-3):5–148.

Choo, J. and Sun, W. (2018). Coupled phase-field and plasticity modeling of geological materials: From brittle fracture to ductile flow. *Computer Methods in Applied Mechanics and Engineering*, 330:1–32.

Fang, J., Wu, C., Li, J., Liu, Q., Wu, C., Sun, G., and Qing, L. (2019). Phase field fracture in elasto-plastic solids: variational formulation for multi-surface plasticity and effects of plastic yield surfaces and hardening. *International Journal of Mechanical Sciences.*

Francfort, G. A. and Marigo, J.-J. (1998). Revisiting brittle fracture as an energy minimization problem. *Journal of the Mechanics and Physics of Solids*, 46(8):1319–1342.

Griffith, A. and Gilman, J. J. (1968). The phenomena of rupture and flow in solids. *Transactions of the ASM*, 61:855–906.

Hoxha, D. and Auvray, C. (2004). Résultats des essais sur échantillons pour le développement des modèles rhéologiques hm et thm des argilites. *Rapport Andra n D. RP. 0ENG. 98.013/A.*

Irwin, G. R. (1958). Fracture. In *Elasticity and Plasticity/Elastizität und Plastizität*, pages 551–590. Springer.

Liu, Z. and Shao, J. (2017). Strength behavior, creep failure and permeability change of a tight marble under triaxial compression. *Rock Mechanics and Rock Engineering*, 50(3):529–541.

Mánica, M., Gens, A., Vaunat, J., and Ruiz, D. F. (2017). A time-dependent anisotropic model for argillaceous rocks. application to an underground excavation in callovo-oxfordian claystone. *Computers and Geotechnics*, 85:341–350.

Miehe, C., Hofacker, M., Schänzel, L.-M., and Aldakheel, F. (2015). Phase field modeling of fracture in multi-physics problems. part ii. coupled brittle-to-ductile failure criteria

and crack propagation in thermo-elastic–plastic solids. *Computer Methods in Applied Mechanics and Engineering*, 294:486–522.

Miehe, C., Hofacker, M., and Welschinger, F. (2010a). A phase field model for rate-independent crack propagation: Robust algorithmic implementation based on operator splits. *Computer Methods in Applied Mechanics and Engineering*, 199(45-48):2765–2778.

Miehe, C., Welschinger, F., and Hofacker, M. (2010b). Thermodynamically consistent phase-field models of fracture: variational principles and multi-field fe implementations. *International Journal for Numerical Methods in Engineering*, 83(10):1273–1311.

Moes, N., Dolbow, J., and Belytschko, T. (1999). A finite element method for crack growth without remeshing. *Internat. J. Numer. Methods Engrg.*, 46:131–150.

Mumford, D. and Shah, J. (1989). Optimal approximations by piecewise smooth functions and associated variational problems. *Communications on pure and applied mathematics*, 42(5):577–685.

Oliver, J. (1996). Modelling strong discontinuities in solid mechanics via strain softening constitutive equations, part 1: fundamentales. *Internat. J. Numer. Methods Engrg.*, 39:3575–3600.

Settari, A. and Walters, D. A. (1999). Advances in coupled geomechanical and reservoir modeling with applications to reservoir compaction. In *SPE symposium on reservoir simulation: houston TX, 14-17 February 1999*, pages 345–357.

Seyedi, D. M., Armand, G., and Noiret, A. (2017). "transverse action"–a model benchmark exercise for numerical analysis of the callovo-oxfordian claystone hydromechanical response to excavation operations. *Computers and Geotechnics*, 85:287–305.

Shao, J., Henry, J., Skoczylaz, F., and Shahrour, I. (1993). Study of massive water injection by thermoporomechanical coupling model. *Computers and Geotechnics*, 15(2):105–121.

Zeng, Q., Yao, J., and JF, S. (2018). Numerical study of hydraulic fracture propagation accounting for rock anisotropy. *Journal of Petroleum Science and Engineering*, 160:422–432.

Zeng, Q., Yao, J., and JF, S. (2019). Study of hydraulic fracturing in an anisotropic poroelastic medium via a hybrid edfm-xfem approach. *Computers and Geotechnics*, 105:51–68.

Zhao, L., Shao, J., and Zhu, Q. (2018a). Analysis of localized cracking in quasi-brittle materials with a micromechanics based friction damage approach. *Journal of the Mechanics and Physics of Solids*, 119:163–187.

Zhao, L., Zhu, Q., and Shao, J. (2018b). A micromechanics-based plastic damage model for quasi brittle materials under a large range of compressive stress. *International Journal of Plasticity*, 100:156–176.

Zhu, Q., Zhao, L., and Shao, J. (2016). Analytical and numerical analysis of frictional damage in quasi brittle materials. *Journal of the Mechanics and Physics of Solids*, 92:137–163.